UNIVERSITY OF OKLAHOMA

GRADUATE COLLEGE

CHARACTERIZATION OF CEMENT-STABILIZED CLAY USING EXPERIMENTAL AND ANALYTICAL TECHNIQUES

A DISSERTATION

SUBMITTED TO THE GRADUATE FACULTY

in partial fulfillment of the requirements for the

Degree of

DOCTOR OF PHILOSOPHY

By

WASSIM EMILE TABET
Norman, Oklahoma
2015

CHARACTERIZATION OF CEMENT-STABILIZED CLAY
USING EXPERIMENTAL AND ANALYTICAL TECHNIQUES

A DISSERTATION APPROVED FOR THE
SCHOOL OF CIVIL ENGINEERING AND ENVIRONMENTAL SCIENCE

BY

Dr. Amy B. Cerato, Chair

Dr. Kanthasamy K. Muraleetharan

Dr. Gerald A. Miller

Dr. Kianoosh Hatami

Dr. Royce W. Floyd

Dr. Andrew S. Elwood Madden

To my beautiful and most precious Hiba Baroud
And to my wonderful family:
My father Emile, my mother Antoinette, and my brother Rabih

Acknowledgements

First and foremost, I would like to give thanks to God, the Virgin Mary, my guardian angel, and all the saints for showering me with graces and blessings that gave me strength and perseverance to complete this work.

I am grateful for my parents, Emile and Antoinette, and my brother Rabih, for keeping me in their prayers, always encouraging me in all my endeavors, and supporting me in every aspect of my life. I love you so much.

I want to thank my advisor, Dr. Amy Cerato, for her motivation, understanding, and support since the day I started as an exchange student.

I would like to express my sincere gratitude to my committee members, Dr. Muralee, Dr. Miller, Dr. Hatami, Dr. Floyd, and Dr. Madden for their teaching, encouragement, and valuable reviews that helped improve the quality of this dissertation, and to Dr. Naji Khoury for putting me on track to achieve this milestone.

To my colleagues and friends, you are too many to name you all but you know who you are! I cannot thank you enough for providing me with all sort of support ranging from technical to comic relief. Your friendship will always be cherished.

To all the faculty and staff of the School of Civil Engineering and Environmental Science for their help and kindness, especially to Mr. Mike Schmitz for his craftsmanship and Mrs. Susan Williams for her sincere affection.

And finally, to the love of my life, Hiba Baroud, for being the reason I stayed. Without your love, patience, and support, this work would not have been possible. You are my rock. I am blessed to have you in my life. I love you.

Table of Contents

List of Tables

List of Figures

Abstract

Problematic soils such as soft, compressible, collapsible, or expansive soils are widespread throughout the world and are often becoming unavoidable due to the continuous expansion of societies. Soil improvement techniques are commonly used to enhance soil properties, increase strength and stiffness, control deformation, and reduce permeability. While soil stabilization has been implemented for many decades and the methods of application have been vastly refined, mainly empirically, an in-depth knowledge of the underlying mechanisms remains lacking.

This research study is dedicated to advancing microstructure characterization of stabilized soil and understanding the fundamental mechanisms and microstructure evolution of cement-stabilized clay in order to better understand the macroscopic behavior of the soil. A pure kaolinite was the chosen soil for this study and Portland cement was the selected stabilizer. Kaolinite samples and cement-stabilized samples were compacted at their optimum conditions and unconfined compression tests were performed to record the macroscopic behavior. An extensive set of laboratory tests including X-Ray Diffraction (XRD), Scanning Electron Microscopy (SEM), Energy Dispersive X-Ray Spectrometry (EDS), X-Ray Fluorescence (XRF), thermogravimetry (TG), and Mercury Intrusion Porosimetry (MIP), has been used to reveal the mineralogy, structure, mineral distribution, elemental composition, and pore size distribution and their corresponding changes with time due to chemical stabilization. The findings confirmed that the addition of cement resulted in the flocculation of the originally dispersed fabric accompanied by a shift from a bimodal to a unimodal pore size distribution. Cementitious products were increasingly abundant with time, mostly formed in void spaces and resulted in the partitioning of large pores into smaller pores. Calcium silicate hydrate (CSH) phases were the major hydration products responsible for strength gain and were spread continuously throughout the samples binding the clay particles together. On the other hand, the remaining hydration products were found as isolated crystals. Quantitative characterization of microstructural features was also performed. The amounts of CSH and calcium hydroxide were measured through TG tests and monitored with time and their correlation with strength gain was established. The addition of cement caused the kaolinite to dissolve and contribute to the formation of cementitious products via pozzolanic reactions. The size of the clay particles was noticeably shrinking as observed in SEM images. Quantitative XRD using whole-pattern fitting and the Reference Intensity Ratio confirmed that the amount of kaolinite was decreasing logarithmically with curing time and that a strong linear correlation was observed between the amount of kaolinite and the unconfined compressive strength.

This research study provides a comprehensive characterization of cement-stabilized clay based on experimental and analytical techniques used in several disciplines such as engineering, geology, materials science, and geomechanics. The advances in the understanding of soft clay and its stabilized counterpart at the micro-scale will form the framework for constructing future constitutive and physical models to better predict the macroscopic behavior of soils. This research also lays the groundwork for future efforts that will continue to expand the knowledge of the intricate reactions and subsequent changes that occur in stabilized soils.

Chapter 1: Introduction

1.1 General

Many locations in the United States and around the world contain problematic soils such as soft, compressible, collapsible, or expansive soils. As society expands, encountering such soils becomes inevitable, and engineers must either improve the soil or install deep foundations to competent soil or rock. Very often, soil improvement techniques are more reliable, efficient, cost-effective, and environmentally friendly than deep foundations. Mechanical improvement or stabilization such as compaction is a possible option; but engineers often find that chemically stabilizing the soil and altering its physicochemical properties is necessary for better improvement. The main objectives of soil improvement techniques are typically to increase strength, control deformation, and reduce permeability. The research herein focuses on understanding the fundamental microscopic properties and microstructure evolution of cement-stabilized soft clay in order to better understand how that soil will behave at the macro-scale. The advances in the understanding of a soft clay, both improved and unimproved, at the micro-scale will form the framework for constructing future constitutive and physical models to predict the macroscopic behavior of soft clays.

The research goal is to advance microstructure characterization of clayey soil and its stabilized counterpart for better understanding of macroscopic behavior. One of the difficulties of understanding the properties of soft clays on the micro-scale is that the soil particle size is extremely small and difficult to isolate. Moreover, the large number of chemical reactions that take place during the stabilization process makes things even more complicated. Therefore, in order to facilitate the analyses of various laboratory tests, a pure kaolinite was selected for this study. Some of the advantages of using pure kaolinite are (i) the limit of mineralogical makeup which would produce simpler X-ray diffraction (XRD) spectra in comparison to a natural soil, (ii) the larger particle size which would make more visible the interaction of individual clay particles and the effects of stabilization at the micro-scale when imaged using scanning electron microscopy (SEM), and (iii) the well-defined structure and hydration behavior. This goal of advancing the microstructural characterization for macroscopic behavior prediction is achieved through imaging techniques (SEM), and quantifying mineralogical and structural microscopic properties in the evolution of macroscopic behavior to better understand the fundamental behavior of clays.

1.2 Objective and Scope of Work

The research goal is to advance microstructure characterization of cement-stabilized soils for better understanding of macroscopic behavior. The objectives of the research are to (i) investigate the effect of chemical stabilization on micro-scale properties and the corresponding change in macroscopic behavior, (ii) assess the role of the microscopic properties (e.g., mineralogical, structural) in the evolution of macroscopic behavior to better understand the fundamental behavior of clays, and (iii) derive various relationships, preferably quantitatively, of these properties with the macroscopic behavior.

To meet the objectives of this study, the scope of this research encompasses:

1. Performing laboratory experiments to disclose the common geotechnical and physicochemical characteristics of a manufactured soil, along with its stabilized counterpart.

2. Conducting XRD, SEM, EDS, XRF, TG, and MIP to reveal the mineralogy, structure, mineral distribution, elemental composition, and pore size distribution and the changes of these features attributed to chemical stabilization.
3. Quantifying the macroscopic behavior of the selected soil samples in terms of unconfined compression strength.
4. Investigating the effect of chemical stabilization on the micro-scale properties and the corresponding change of macroscopic behavior.

1.3 Dissertation Outline

This dissertation is organized into five chapters. Chapter 2 provides background information about soil stabilization and various experimental tests that have been used in previous published studies to characterize different aspects of the soil. Chapter 3 provides detailed description of the soil, samples preparation, and the methods used for each test in this study. Chapter 4 presents the results and analyses of soil structure, composition, mineralogy, and strength, and their evolution with time due to stabilization. Finally, the summary, conclusions, and recommendations for future work are proposed in Chapter 5.

Chapter 2: Literature Review

2.1 Experimental Tests

2.1.1 Assessing Structure and Texture

Since its introduction to the market in 1965, Scanning Electron Microscopy (SEM) has been widely used in material-characterization laboratories and has proven useful in its application to mineralogy (England, 1991). Given its much shorter wavelength compared to that of visible light, the electron beam can interact with a specimen surface to provide high-resolution images. The great depth of field makes this instrument appropriate to directly observe rough surfaces and its ability to achieve high magnifications and resolutions is optimal to study the microstructure of soil samples and evaluate the geometric arrangement of clay particles. The electron source is a cathode in the form of tungsten filament (or lanthanum hexaboride or field emission) that is heated and then the electrons are drawn from it by an accelerating voltage. This electron gun and the column of the instrument where the primary electron beam passes function under a high vacuum so that the electrons do not interact with air molecules. Electromagnetic lenses located in the column focus and direct the electron beam to scan across the surface of the specimen. The signals emitted from the interaction of the electron beam with the surface of the specimen are collected by various detectors, amplified, and fed to electronically adjust the brightness on a cathode ray tube (CRT) along with other types of monitors used to display an image of the specimen. Since the SEM works under high vacuum, the sample being scanned should be completely dry and coated with a conductive material such as gold or iridium.

The Environmental Scanning Electron Microscope (ESEM) is an advanced SEM that allows the imaging of samples that are in their intact state, without the need to dry or coat them. This is possible because the ESEM is equipped with (i) differential pumping system where the high vacuum in the column is separated from the pressure in the specimen chamber, (ii) gaseous detection device that prevents sample charging, and (iii) cooling stage that allows for the control of sample temperature.

Mercury Intrusion Porosimetry (MIP) is a capillary penetration technique used to quantitatively determine the porous nature of materials such as total pore volume, pore diameter, and pore size distribution (PSD). Through the use of a porosimeter, a non-wetting liquid (usually mercury) is intruded into the pores of a sample by incrementally applying pressure while monitoring the mercury filled specimen pore volume upon each increment. The pore size is calculated based on Washburn's equation (Washburn, 1921) which assumes that the liquid is flowing in cylindrical tubes: $r = -2 T_s \cos\theta / P$; where r is the radius of the pore, T_s is the surface tension of the liquid, θ is the contact angle of the liquid-air interface to the solid, and P is the applied pressure.

Specific Surface Area (SSA) is defined as the surface area per unit mass of soil and is usually reported as m^2/g. SSA is considered an important factor that controls many physical and chemical properties of fine-grained soils and thus has a significant influence on their behavior (Peterson et. al, 1996, Cerato and Lutenegger, 2002). It is divided into external SSA and internal SSA, which combined, constitute the total SSA. The external SSA consists of the surface area on the outside of the clay particles, excluding the areas in the interlayer surfaces, whereas the internal SSA is made of the areas in the interlayer surfaces. A common method to obtain total SSA is from the

Ethylene Glycol Monoethyl Ether (EGME) method proposed by Cerato and Lutenegger (2002). External SSA is usually determined by gas adsorption method (BET method) which was proposed by Brunauer et al. (1938).

2.1.2 Mineralogical Assessment

The X-ray Diffraction (XRD) technique is one of the most important and widely used methods for mineralogical assessment of materials. X-radiation is the part of the electromagnetic radiation spectrum that lies between the ultraviolet and gamma ray radiations (Last, 2001). Since X-rays have similar wavelengths (1 – 100Å) as the spacing of atomic planes in crystalline materials (d-spacing), the diffraction phenomenon is made possible. Diffraction, at a given angle, occurs when all scattered waves from an incident beam interfere constructively. This is best described by Bragg's law: $n \lambda = 2 d \sin\theta$; where n is an integer, λ is the wavelength of the incident X-ray, d is the spacing between two adjacent planes of atoms, and θ is the angle between the incident wave and the atomic plane. The number of diffracted X-rays is counted at each angle to collect a diffraction pattern. The diffraction pattern of crystalline material is a unique property of that material and is compared to databases to identify the material.

2.1.3 Elemental and Compositional Analyses

Energy-Dispersive X-ray Spectroscopy (EDS) is usually integrated in an SEM instrument and used for the elemental analysis or chemical characterization of a point or a region of a sample. A high-energy beam of electrons slams into the studied area exciting an electron in an inner shell. If the energy is high enough, the electron being excited gets ejected from the inner orbital leaving a hole behind. An electron from a higher-energy orbital then migrates to fill this hole while releasing energy equal to the difference between the high- and low-energy shells in the form of an X-ray. The energy of these X-rays is characteristic of the atomic structure of the element which allows the elemental composition of the studied region.

X-ray Fluorescence (XRF) is also widely used for elemental and chemical analyses. High-energy X-rays are shot from an x-ray tube onto a sample. The x-rays knock individual electrons out of their orbit around an atom. Electrons in the outer orbits then jump down to fill the vacancies while emitting x-ray fluorescence radiation in amounts specific to the element they are a part of. The XRF radiation is then identified by an XRF detector. The intensity of the radiation is proportional to the concentration of the element in the sample.

Thermogravimetric analysis (TG) is a method of thermal analysis in which changes of physical and chemical properties are measured as a function of increasing temperature. The apparatus for TG consists of a sample holder (alumina crucible), precision balance, and a furnace connected to a temperature controller. During the test, the weight of the sample is continuously recorded as it is heated at a constant rate to high temperatures. Various components are decomposed at different temperatures and the weight percentage of each resulting weight loss can be measured. The TG instrument can also be coupled with a mass spectrometer (MS) for evolved gas analysis.

2.2 Applications of Experimental Tests in Geotechnical Engineering

Numerous studies have used one or more of the techniques mentioned in the previous section to characterize soils in several engineering applications. The development of SEM has significantly contributed to the development of microfabric studies of soils by allowing researchers to actually observe the microstructure of soils at high magnifications and resolutions (Gillot 1969, Collins and McGown 1983, Delage and Lefebre 1984, Delage et al. 1996, Mitchell and Soga 2005). Many studies examined the microstructure of soils compacted at different states on the compaction curve and correlated its relationship with various engineering properties such as strength, compressibility, water permeability, and effective conductivity (Barden and Sides 1970, Ahmed et al. 1974, Delage et al. 1996, Tabet and Cerato 2015). Al-Rawas and McGown (1999) employed SEM in their investigation on the microstructure of the expansive Omani soils. They used the characterization scheme developed by Collins and McGown (1983) to describe the soil microfabric and track its changes due to swelling to better understand expansive soil behavior. Another study by Al-Rawas (1999) combined both SEM and XRD techniques in order to extensively investigate the factors controlling the expansive nature of the soils and rocks of northern Oman. He found that montmorillonite with predominantly Na^+ cations is the most common clay mineral in the region, due to the geological history of Northern Oman, and is the main reason for the high swelling potential of the samples tested. However, given that these swelling clays occur as intermittent bands, it would be difficult to make any reliable field prediction of heave. Tabet and Cerato (2015) used SEM to evaluate the influence of the microstructure on the effective conductivity in compacted clay samples with variable plasticity index (PI) values and found that the effective conductivity was significantly higher in the horizontal direction compared to that in the vertical direction. They attributed this observation to the highly preferred orientation of clay particles and their decreased tortuosity in the horizontal direction and the increased tortuosity in the vertical direction. Lin and Cerato (2014) used conventional SEM and environmental scanning electron microscopy (ESEM) to disclose the microstructure of two natural expansive clays at their initial compacted state and monitored the structural changes during two wetting-drying cycles using the ESEM. In general, the micrographs obtained from both imaging techniques were comparable. The structural changes, however, were difficult to detect at the micro-scale even though the volumetric changes were significant at the macro-scale.

Attempts have been made to develop quantitative relationships between SEM micrographs and soil characteristics such as porosity, average particle size, water activity, permeability, and aggregate orientation (Smart and Leng 1993, Frost and Wright 1993, Tovey and Hounslow 1995, Shi et al. 1995, Frost and McNeil 1998, Shi et al. 1998, Martinez-Nistal et al. 1999, Katti and Shanmugasundaram 2001, Montes-H et al. 2003a&b, Liu et al. 2005); mostly through image digitization, binarization and isolation of target objects. For example, Wang et al. (2012) used the ESEM to collect microstructure images of soft soil before and after consolidation, and image processing software (PECAS software) to process the images. First, image preprocessing, which included adjusting exposure, brightness, contrast, and gray coefficient, was necessary to get reasonable microscopic structure parameters. Next, binary threshold segmentation was implemented to change gray images into black and white images. Finally, the equivalent size and size distribution were computed and analyzed. The results showed that, through consolidation, the big cells decreased and small cells increased with a reduction in equivalent size. Similarly, the pore area significantly decreased; the big pores were largely reduced and the small pores increased slightly, with an increase of pore number. The pore distribution was fairly uniform, with the majority of the pores smaller than 1 μm, and the equivalent pore size was reduced. A study by Cetin et al. (2007) quantitatively investigated the structure changes during compaction of a cohesive soil as a function of various molding moisture contents. A natural clay soil was mixed with muscovite mica sand of 0.125 to 1 mm size derived from a muscovite schist rock. The purpose of using these platy muscovite mica particles was to increase the number of measurable elongated particle constituents in the soil. Three sections were trimmed from each sample, dried, vacuum-impregnated with epoxy resin, and then cut into thin sections. Afterwards, they were scanned into appropriate computer programs and the azimuths of axes of the oriented particles were measured according to Brewer (1976). The measurements were evaluated in two ways: 1) their averages with respect to the horizontal were calculated, 2) percentages of the measurements falling in the ranges of 0-10^{o}, 10-20^{o}, and so on, from the horizontal were determined. The orientation patterns were graphically presented by plotting the data on rose diagrams. The results agreed with previous studies; the soil fabric was randomly oriented dry of optimum and became increasingly oriented towards optimum; however, contrary to the generally accepted view, the results revealed that the overall degree of preferred orientation decreased as the moisture content continued to increase wet of optimum. Two other studies by Cetin (2004) and Cetin and Söylemez (2004) used similar techniques to examine soil-particle and pore orientations during consolidation and drained and undrained shear of a cohesive soil. Montes-H et al. (2003a&b) successfully used ESEM coupled with the digital image analysis (DIA) program Visilog to measure the volume change of a bentonite during shrink and swell cycles along the wetting and drying curves. The program quantified the percent increase of the surface as a function of time at different relative humidities and estimated the influence of interlayer cation in water sorption and swelling-shrinkage of the bentonite. In general, however, quantification methods based on SEM micrographs of the microstructure require significant simplifications and are considered primitive and highly subjective (Lin 2012).

Mercury Intrusion Porosimetry (MIP) is a common technique used to quantitatively describe the microstructure of interconnected pores by measuring the pore volume intruded corresponding to the required pressure for intrusion, and thus the pore size distribution (PSD) can be deduced. The resulting graph from an MIP test typically includes the log differential intrusion vs. entrance pore size (Romero and Simms 2008). Graphs from MIP tests showed that a dual-porosity structure (i.e., inter-aggregate pores and intra-aggregate pores) forms in compacted soil samples and is characterized by two standing PSD peaks at around 0.02~0.3 μm and 7~10 μm (Romero and Simms 2008, Romero et al. 1999, Simms and Yanful 2002, Li and Zhang 2009, Koliji et al. 2010). The first peak describes the intra-aggregate micropores which are determined by interactions between clay platelets, whereas the second peak describes the inter-aggregate macropores which are controlled by aggregate/cluster shapes, alignment, orientation and contact style. An example of the pore size distribution of a compacted soil is presented in Figure 2.1.

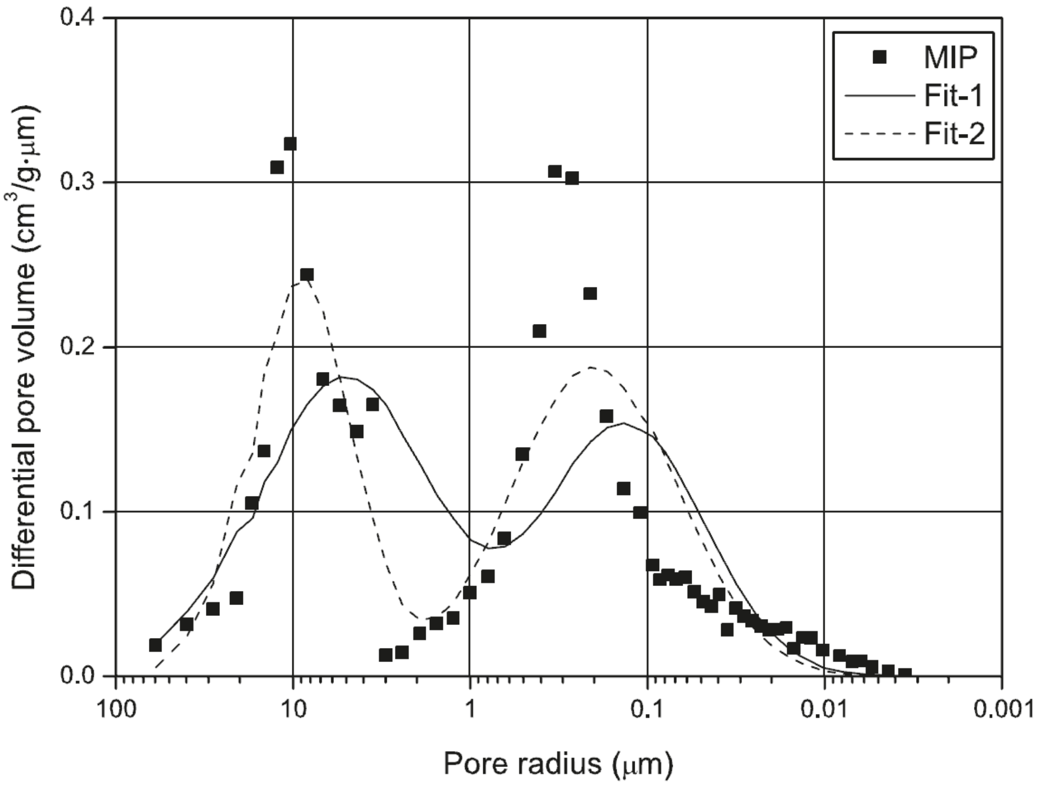

Figure 2.1: Pore-Size Distribution of a Compacted Soil (from Li and Zhang, 2009)

The PSD is considered an important fabric parameter, especially in fine-grained soils, and has been correlated with various macroscopic properties such as strength, stiffness, volume change (consolidation), hydraulic conductivity, soil-water characteristic curve (Ahmed et al. 1974, Garcia-Bengochea et al. 1979, Delage and Lefebvre 1984, Griffiths and Joshi 1989, Romero et al. 1999, Simms and Yanful 2002). Ahmed et al. used MIP to examine the influence of the method of compaction (Standard Proctor, keading, and static), compactive effort, molding water content, and drying method (oven vs. freeze-drying) on the PSD. They showed that different compaction methods resulted in PSD curves with similar characteristics, but the molding water content had a significant effect on the PSD. They selected three arbitrary diameter ranges, coarse (600-50 μm), medium (50-0.5 μm), and fine (0.5-0.016 μm) to compare the PSDs of samples that have similar porosities but compacted at different water contents. They found that samples compacted dry of optimum had a very small amount of coarse pores, a large amount of medium pores, and a smaller amount of fine pores. While the amount of coarse pores was similar in samples compacted wet of optimum, the amount of medium pores was about half and that of fine pores was about double the amount obtained for samples compacted dry of optimum. Moreover, the total porosity of samples compacted wet of optimum and oven-dried was considerably smaller than similar samples dried using the freeze-drying method. Koliji et al. (2010) studied the combined effects of suction variation and mechanical loading on the structure of an aggregated soil and its evolution using a combination of MIP, ESEM, and neutron computed tomography (CT). Li and Zhang (2009) investigated the variations of the microporosity structure of a lean clay with sand during compaction, saturation, and drying processes. The results show that the associated volume of the inter-aggregate pores is closely associated with the void ratio of the compacted sample. In addition, soil compaction causes significant reduction in inter-aggregate pores while slightly affecting the intra-aggregate pores. On the other hand, the change of the intra-aggregate pores is dominant during saturation and drying.

SEM was also used to investigate changes in soil structure due to chemical stabilization (Choquette et al. 1987, Lin et al. 2007, Horpibulsuk et al. 2010). When combined with MIP, valuable qualitative and quantitative information can be garnered about the arrangement and size of particles and pores and their distribution in a soil sample. For instance, Choquette et al. (1987) studied the mineralogical and microtextural changes associated with lime stabilization of marine clays from eastern

Canada. They found that reaction products of Calcium-Aluminum-Silicate-Hydrate (CASH) and Calcium-Silicate-Hydrate (CSH) types are formed, affecting the pore size distribution, and the gain in strength is related to the progressive formation of these new phases. It should be noted that CSH, CAH, and CASH have variable compositions and are usually written with hyphens (e.g. C-S-H) to indicate a non-stochiometric compound. Horpibulsuk et al. (2010) and Horpibulsuk (2012) extensively studied the strength and microstructure development of cement stabilized clays using SEM, MIP, and thermogravimetric analysis (TG). Based on the compaction tests, the maximum dry unit weight of the stabilized samples was higher than that of the unstabilized samples whereas their optimum water content was practically identical. For the same compaction energy and curing time, the strength of the stabilized samples increased with water content up to 1.2 times the optimum moisture content (OMC) and started decreasing beyond that point. The maximum strength of the unstabilized clay is at OMC and maximum dry unit weight because it mainly depends on the densification. Similar trends were observed with class-C fly ash (CFA) blended cement stabilized clay at different replacement ratio (Horpibulsuk et al., 2009). They also studied the strength development over a wide range of cement content at a water content of 1.2OMC and found that the strength increase can be classified in three zones as illustrated in Figure 2.2.

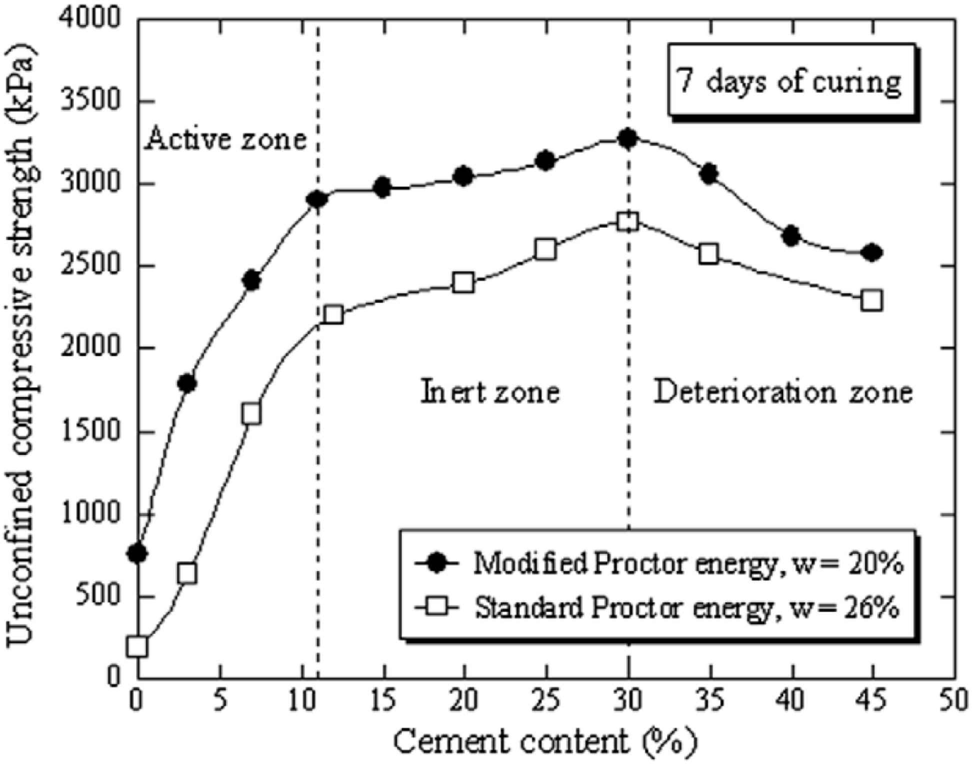

Figure 2.2: Strength Development vs. Cement Content (from Horpibulsuk et al. 2010)

The first is the active zone in which strength increases with an increase in cement content due to the increased cement to grain contact which results in an equal amount of bonding. The second is the inert zone in which both pore size distribution and cementitious products change insignificantly with increasing cement resulting in only a slight improvement. The third is the deterioration zone in which strength decreases when the cement content increases beyond a certain amount resulting in a reduction in water content, which decreases the degree of hydration, and thus, cementitious products. From SEM and MIP results, they found that after four hours of curing, a cement gel covers the soil clusters and fills the pores. During the early stage of curing (fewer than 7 days), the volume of pores smaller than 0.1 micron significantly decreases due to the cementitious products filling them while the volume of pores larger than 0.1 micron slightly increases due to the coarse unhydrated cement particles that cause large soil-cement clusters and large pores. After 7 days of curing, the volume of pores larger than 0.1 micron tends to decrease while the volume of pores smaller than 0.1 micron tends to increase. This was attributed to the cementitious products that fill the large pores and divide them into smaller pores leading to a reduction in total pore volume. Consequently, the cementitious products provide a significant increase in strength by filling the pore space and enhancing the inter-cluster bonding strength. They also found that the role of fly ash in blended cement stabilized clay did not exactly act as a pozzolanic material; the fly ash surfaces were smooth indicating that pozzolanic reactions were minimal, contrary to concrete technology where the products of the pozzolanic reactions result in etching on fly ash surfaces. The role of fly ash in blended cement stabilized clay is rather as a dispersive material that divides the cement-clay clusters with large pores into smaller clusters with smaller pores. This increases the reactive surfaces, which in turn increases the degree of hydration.

Thermogravimetric analysis has been widely used to characterize minerals, particularly hydrous phases such as clays and zeolites, as well as determine hydration products in cement paste (Midgley 1979, Stucki and Bish 1990, Taylor 1990, Horpibulsuk et al. 2010). Cheng et al. (2010) used thermogravimetric analysis-mass spectrometry (TG-MS) to characterize eight different kaolinites. They concluded that the dehydroxylation temperature of kaolinite is around 450 ^{o}C but could vary due to the degree of disorder of the kaolinite structure and the type and amount of impurities such as calcite and sulfide. MS data of CO_2^+ showed peaks at around 225 and 350 ^{o}C indicating the presence of organic impurities, whereas the peak at 710 ^{o}C was attributed to the decomposition of calcite. Wang et al. (2004a) implemented several analytical techniques including XRD, SEM, TG, and x-ray absorption near edge structure (XANES) to study the mineralogy of soil susceptible to sulfate attack after stabilization by Type I Portland cement. They quantified the amount of gypsum present based on the mass loss between the temperatures 98 and 116 ^oC, the amount of kaolinite from mass loss between 400 and 500 ^oC, and attributed the reduction in mass between 620 and 730 ^oC to the decomposition of carbonate. Several studies using TG were performed on Portland cement pastes to determine the hydration products including CSH, CAH, CASH, $Ca(OH)_2$, and ettringite (Midgley 1979, El-Jazairi and Illston 1977 and 1980, Wang et al. 2004b, Horpibulsuk et al. 2010). One outcome from these studies was that four distinct regions related to different reactions were identified from the TG/DTG curves, where DTG is the derivative of the TG curve. These regions were defined as follows (with slight variations among different references):

a) From room temperature to 105 ^oC. The mass loss is attributed to the evaporation of adsorbed moisture.
b) From 105 to 440 ^oC. The mass loss in this region is related to the dehydration reactions which include the CSH phases.
c) From 440 to 580 ^oC. The mass loss is attributed to the dehydroxylation of calcium hydroxide.
d) From 580 to 1000 ^oC. This region consists largely of decarbonation of calcium carbonate.

An example of the TG/DTG curves for Portland cement paste showing these temperature bins and the corresponding compounds is illustrated in Figure 2.3.

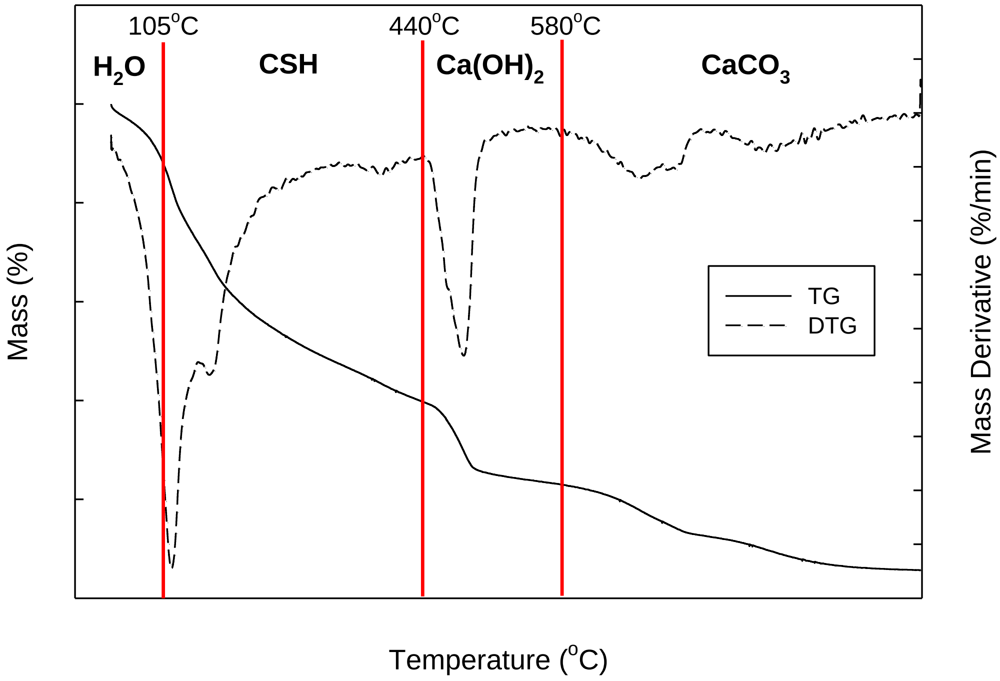

Figure 2.3: Example of TG/DTG Curves for Portland Cement Paste

In their study on the strength development in cement-stabilized silty clay, Horpibulsuk et al. (2010) described the change in cementitious products in terms of the change in $Ca(OH)_2$ alone. They determined the amount of $Ca(OH)_2$ based on the weight loss between 450 and 580 °C since, at this temperature range, $Ca(OH)_2$ is decomposed into CaO and H_2O. The $Ca(OH)_2$ content was then approximated by multiplying the weight loss due to the evaporation of water by 4.11. Attributing the amount of $Ca(OH)_2$ in stabilized soils, as opposed to cement paste, to the weight loss between 450 and 580 °C can be inaccurate due to the fact that the dehydroxylation of kaolinite occurs at a similar range.

2.3 Soil Stabilization

2.3.1 Cement Chemist Notation

Cement Chemist Notation (CCN) is an old but convenient notation developed by cement chemists to simplify the writing of the chemical formulas of oxides in cement. These are abbreviated in single letters as follows: C = CaO, S = SiO_2, A = Al_2O_3, F = Fe_2O_3, T = TiO_2, M = MgO, K = K_2O, N = Na_2O, $\bar{C}$ = CO_2, $\bar{S}$ = SO_3, P = P_2O_5, and H = H_2O. These abbreviations are used throughout this section to explain the hydration of Portland cement which helps understanding the soil stabilization process.

2.3.2 Hydration of Portland Cement

Portland Portland cement is a heterogeneous material comprised of several fine-grained minerals. The four major minerals in Portland cement are C_3S (tricalcium silicate), C_2S (dicalcium silicate), C_3A (tricalcium aluminate), and C_4AF (tetracalcium alumino ferrite). All the compounds in Portland cement are anhydrous, but in the presence of water they react to form hydrated compounds (Lea and Hewlett 1998). The hydration of cement occurs through a dissolution-precipitation process. This hydration process strengthens the soil matrix it is mixed in. Numerous and complex reactions occur during the hydration of Portland cement but the major ones are as follows:

$$2C_3S + 6H = C_3S_2H_3\ (calcium\ silicate\ hydrate) + 3CH\ (calcium\ hydroxide)$$

$$2C_2S + 4H = C_3S_2H_3\ (calcium\ silicate\ hydrate) + CH\ (calcium\ hydroxide)$$

In the absence of gypsum, the tricalcium aluminate reacts with water causing rapid setting of cement as follows:

$$2C_3A + 27H = C_4AH_{19} + C_2AH_8 = 2C_3AH_6 + 15H$$

Gypsum is added to the cement in order to control setting by considerably retarding the hydration of C_3A through the formation of ettringite on the surface of C_3A.

$$C_3A + 3C\bar{S}H_2\ (gypsum) + 26H = C_6A\bar{S}_3H_{32}\ (ettringite)$$

Once all the gypsum is consumed and insufficient sulfate ions are present in the solution, ettringite becomes unstable and converts to monosulfate with further hydration of C_3A, or into solid solution between $C_4A\bar{S}H_{12}$ and C_4AH_{13}. Any remaining C_3A will hydrate to produce C_4AH_{19} which typically converts to C_3AH_6 with time (Soroka 1980, Lea and Hewlett 1998, Bensted and Barnes 2002).

$$2C_3A + C_6A\bar{S}_3H_{32} + 4H = 3C_4A\bar{S}H_{12}\ (monosulfoaluminate\ or\ monosulfate)$$

$$C_3A + CH + 12H = C_4AH_{13}$$

In the absence of gypsum, the calcium aluminoferrite reacts as follows:

$$3C_4AF + 60H = 2C_4(A,F)H_{19} + 2C_2(A,F)H_8 + 4(F,A)H_3$$

$$= 4C_3(A,F)H_6 + 2(F,A)H_3 + 24H$$

In the presence of gypsum and calcium hydroxide, the ferrite phase reacts in a similar way as C_3A, but more slowly, as follows:

$$C_4AF + 3C\bar{S}H_2 + 21H = C_6(A,F)\bar{S}_3H_{32} + (F,A)H_3$$

$$C_4AF + C_6(A,F)\bar{S}_3H_{32} + 7H = 3C_4A\bar{S}H_{12} + (F,A)H_3$$

2.3.3Pozzolanic Reactions in Stabilized Soil

An additional soil strengthening mechanism in the presence of water and calcium is pozzolanic reactions. A pozzolan is a siliceous or siliceous-aluminous material with no cementitious properties when by itself, but with the presence of water and calcium (calcium hydroxide) reacts to form cementitious products. In stabilized soils, silica and alumina dissolve from clay particles as well as the stabilizer or pozzolanic agent (e.g. cement or fly ash) and react with the calcium that is mainly derived from the stabilizer such as cement or lime to form calcium silicate hydrate and calcium aluminate hydrate. In the case of kaolinite, $Al_2Si_2O_5(OH)_4$, also written as AS_2H_2 when using the cement chemist notation, the reactions of dissolution and the formation of CSH and CAH are as follows:

$$AS_2H_2 + 3H = A + S_2H_4 + H$$

$$5CH + S_6H_{12} = C_5S_6H_5 + 12H$$

$$4CH + A + 20H = C_4AH_{13} + 11H$$

These reactions show that the cementitious products formed in stabilized soils are very similar to those formed in Portland cement (Diamond and Kinter 1965, Khoury et al. 2006, Chrysochoou 2014), with the main difference being the rate at which these reactions occur (Kruger 1990). As a result of this discussion, complex reactions are expected to occur in chemically stabilized soil; silica, alumina and calcium may be derived from several sources, thus resulting in a multitude of dissolution/precipitation reactions that are occurring at the same time and competing for similar constituents.

2.4 Research Contribution

While soil stabilization has been performed for a very long time and the guidelines and methods of application have been vastly refined, mainly empirically, over the years, an in-depth knowledge of the underlying mechanisms remains lacking. The literature presented previously in this chapter highlighted the advancements accomplished regarding understanding the behavior of stabilized soils to date. The research presented herein is aimed at adding to the fundamental knowledge of the underlying mechanisms that take place during soil stabilization by showing the changes that occur at the micro-scale and how they affect the soil behavior at the macro-scale. The unique approach taken in this study consists of presenting a comprehensive investigation that carefully controlled a combination of several experimental tests and thorough analysis to identify the various changes taking place at the micro-scale responsible for the evolution of macro-scale soil behavior. It is worth noting, however, that the correlations obtained in this study are specific to the soil and stabilizer selected and are not necessarily applicable to other soils and/or stabilizers, but are rather meant to show the sequence of the reactions taking place during soil stabilization and how they all tie together. In addition to advancing the understanding of stabilized soil behavior, the outcome of this study will provide a database that would help improve current constitutive models and their prediction accuracy of stabilized soil behavior.

Chapter 3: Methodology

3.1 Materials

Several preferences were sought in the soil selected for this study. First, the soil had to be a manufactured clay of single mineralogy to minimize the variables related to having several minerals. Second, the clay had to be processed without the addition of dispersive agents during the manufacturing phase to eliminate “quick” behavior after the addition of water. Finally, the soil had to be crystalline with relatively large clay particle in order to facilitate XRD and SEM quantification. The soil chosen for this study was a kaolinite named SA-1 that has been processed by air flotation, and obtained from Active Minerals International, LLC (Gordon, GA).

The first step was to estimate the crystallinity of the kaolinite. Hinckley (1963) proposed an empirical measure of crystal defect density in kaolin group minerals which he termed the “crystallinity index” but is also now known as “Hinckley Index” or HI. HI is a dimensionless number that can be easily calculated from an XRD pattern of a randomly oriented sample, and typically varies between approximately 0.2 and 1.5 (Plançon et al. 1988); the higher the index, the lower the defect density, and the greater the crystallinity. The HI of SA-1 was found to be 1.14 and thus the crystallinity was considered suitable for this study. Relevant physical and chemical properties of SA-1 as obtained from the manufacturer are listed in Table 3.1, and more detailed information is provided in Appendix A.

Table 3.1: Chemical Composition and Physical Characteristics of SA-1 (obtained from manufacturer)

Chemical Analysis	Percentage	Physical Properties	Value
SiO_2	45.60	Specific Gravity	2.6
Al_2O_3	38.40	Raw Color	Cream/Gray
Fe_2O_3	0.40	Particle Size, μm	Percent finer, %
TiO_2	1.50	20	95
CaO	0.06	10	90
MgO	0.05	5	77
K_2O	0.18	2	57
Na_2O	0.03	1	43
LOI	13.8	0.5	30

The stabilizer chosen for this study was Portland cement Type I/II which was obtained from Ash Grove Cement Company (Chanute, KS) through Dolese Bros. Co. (Norman, OK). The first reason for choosing Portland cement is that it is the most commonly used stabilizer in the world mainly due to its abundance, efficiency, and relative inexpensiveness. The second reason is that this study stemmed from a previous project entitled *“NEESR-SG: Understanding and Improving the Seismic Behavior of Pile Foundations in Soft Clays”* in which 10% by weight of Portland cement was used to improve the soil surrounding the piles. The NEESR-SG project highlighted the need for better understanding of the effects of cement on the clay at the micro-scale level in order to eventually incorporate these effects in constitutive models to improve their prediction accuracy in stabilized soils. The chemical composition of the cement, as provided from the manufacturer, is presented in Table 3.2 and the complete data sheet is provided in Appendix B.

Table 3.2: Chemical Composition of Portland Cement Type I/II

Chemical Analysis	Percentage
SiO_2	20.78
Al_2O_3	4.35
Fe_2O_3	3.25
CaO	64.46
MgO	1.93
SO_3	2.89
Na_2O	0.18
K_2O	0.42
CO_2	1.58
LOI	2.20
Potential Compounds	
C_3S	57
C_2S	17
C_3A	6
C_4AF	10

3.2 Common Physical and Engineering Properties

Once a suitable soil was selected, it was subjected to common laboratory tests designed to provide important properties and allow classification of the soil according to the United Soil Classification System (USCS). The laboratory testing program included Atterberg Limits (ASTM D 4318) and unconfined compressive strength (UCS) (ASTM D 2166). The linear shrinkage and shrinkage limit were obtained following the British Standards BS 1377 (1990). The total SSA was measured using the EGME method proposed by Cerato and Lutenegger (2002) and the external SSA was determined by gas adsorption method (BET method) which was proposed by Brunauer et al. (1938).

The liquid and plastic limits are 64% and 25%, respectively. Based on the USCS, the soil is classified as inorganic clay of high plasticity (CH). In order to save material and time, the Harvard Miniature compaction apparatus was used to create the moisture-density curve. This compaction process was designed and calibrated by Khoury and Khoury (2005) to closely match the compaction characteristics of a standard Proctor test. The soil was compacted in a Harvard Miniature mold using a 415.9 g (0.915 lb) hammer and a 30.48 cm (12 in) drop in five equal layers with six blows per layer. The optimum moisture content (OMC) and the maximum dry unit weight (γ_{dmax}) of the soil were found to be 25.06% and 15.04 kN/m^3, respectively, and 26.76% and 14.68 kN/m^3 for its cement-stabilized counterpart. All the properties obtained from the various laboratory tests are summarized in Table 3.3.

Table 3.3: Physical and Engineering Properties of SA-1

Property	Value
Liquid Limit, %	64
Plastic Limit, %	25
Plasticity Index, %	39
Specific Gravity*	2.6
Clay Size Fraction*, %	57
Linear Shrinkage, %	10
Shrinkage Limit, %	25
USCS Classification	CH
Total Specific Surface Area, m^2/g	38
Maximum Dry Unit Weight, kN/m^3	15.04
Optimum Moisture Content, %	25.06
Maximum Dry Unit Weight – Stabilized Soil, kN/m^3	14.68
Optimum Moisture Content – Stabilized Soil, %	26.76

*Values from manufacturer

The stabilized samples were prepared by thoroughly mixing 10% by dry weight of Portland cement (type I/II) powder with the soil before adding the required amount of water to bring the mixture to the desired water content. All samples were compacted in five equal layers using volume-based compaction to optimal conditions (OMC and γdmax). The compacted sample measures 7.11 cm (2.8 in) in height and 3.56 cm (1.4 in) in diameter. Every effort was made to achieve nominally identical samples by weighing the sample after compaction and calculating its density as well as monitoring the moisture content. The samples were then wrapped with plastic wrap and stored in 100% humidity room to cure for various times. Two days were also allowed for the compacted raw soil to achieve homogeneous moisture distribution before running the unconfined compression tests, whereas the stabilized samples were tested after 1, 7, 14, 28, and 90 days of curing. A total of four samples were prepared for each curing; three of which were sheared to obtain to the UCS and were subsequently subjected to the remaining tests, and the last sample was only used for SEM and MIP testing without being sheared. The strain rate used during shear was 1%/min. XRF analysis was used to determine the actual amount of CaO in the tested soil. The raw soil, stabilized soil, and Portland cement were sent to an external lab (ALS Minerals in Reno, NV, USA) for whole rock analysis. Using the method developed in Cerato and Miller (2013), the stabilizer content of the stabilized samples was determined to be 8.5%, which is slightly lower than the actual added cement content of 10%.

3.3 Thermogravimetric Analysis Test

At the end of the unconfined compression test, a small quantity of soil was recovered from each sample and mixed with other samples cured for the same time, and then dried in a 60 ^{o}C oven for about two hours before being thoroughly pulverized. Approximately 43 mg of the dried samples were loaded in alumina crucibles and into the TG machine which was programmed so that it provided a constant heating rate of 10 K/min until 1000 ^{o}C. In this study, the thermogravimetry analyzer, NETZSCH STA 499 F1 Jupiter was connected to the online MS NETZSCH QMS 403C. The gas phase products, mainly water vapor and carbon dioxide, were monitored by the online MS. The gas flow rate was 50 mL/min of Argon (ultra-high purity from Airgas). The TG tests were conducted in duplicate for each curing time using different sub-samples to ensure repeatability of the results.

3.4 Investigation of Mineralogy

For mineralogical analysis, a piece of soil was recovered from the interior of each UCS sample, dried in a 60 ^{o}C oven, and then pulverized to powder with the mortar and pestle. A mass of exactly 1.000 g of the powder was thoroughly mixed with exactly 0.250 g of internal standard, highly crystalline corundum (Al_2O_3), until the powder became homogeneous. The internal standard was used to aid in the quantification process and determine the amorphous content of the sample (De La Torre et al. 2001, Chrysochoou 2014). The mixture was then randomly mounted in the sample holder well. A duplicate from each sample was prepared; thus, for each curing time, a total of six samples were prepared and analyzed. The XRD tests were performed using the Rigaku Ultima IV powder X-ray diffractometer with CuKα radiation set to 40 kV and 40 mA, a diffracted beam graphite monochromater, and Bragg-Brentano parafocusing geometry. The data was collected between two-theta values of 2^{o} to 70^{o} with a step size of 0.02^{o} and a scan time of 2 second per step, with the sample spinning continuously. Qualitative and quantitative analysis of all XRD patterns was performed using Jade software (MDI Jade 10) with reference to the patterns of the International Center of Diffraction Data (ICDD) and the American Mineralogist Crystal Structure Database. The Rietveld method (Rietveld 1969) was used for quantitative analysis of XRD. This method consists of fitting the observed diffraction pattern with a synthetic pattern produced by a mathematical model based on the physics of diffraction. The Rietveld method is also known as a whole-pattern fitting method because the synthesized pattern is the sum of patterns calculated for each phase in the sample (Snyder and Bish 1989). The difference between the observed pattern and the synthesized pattern is then minimized through the optimization of a number of refinable parameters. The Rietveld method cannot capture non-crystalline phases, the internal standard was used to calculate the amorphous content as $A = \frac{R_s - W_s}{R_s(1 - W_s)} \times 100\%$, where R_s is the amount of the internal standard calculated by the Rietveld method and W_s is the weighed amount that was added to the sample. All phases can then be normalized using the amorphous content to obtain true weight percentages. Quantitative analysis was also performed in general accordance with the Reference Intensity Ratio (RIR) method. The RIR is another widely used method for quantitative analysis of XRD patterns. It is based upon scaling all diffraction data to the diffraction of the standard reference. In this study, this method was primarily applied to monitor the ratio of the integrated intensity of the main peak of kaolinite to that of corundum. Moore and Reynolds (1997) and Hillier (2000) recommend the use of integrated intensity instead of peak height especially when dealing with clay minerals because peak height could vary with crystallinity and defects while integrated intensity is constant.

3.5 Investigation of Microstructure

3.5.1 Scanning Electron Microscopy

Since the microscope operates under high vacuum, the wet specimens must be dried first. Samples can be dehydrated using air-drying, oven-drying, freeze-drying, or critical-point-drying techniques. The flash-freezing/freeze-drying technique was adopted in this study because it is considered as the most effective and appropriate method for microstructural preservation of soils (Delage and Pellerin 1984, Kang et al.

2003, Ferber et al. 2009, Li and Zhang 2009). The flash-freezing technique is based on the assumption that during rapid freezing of a wet soil at the temperature of a cryogenic liquid such as liquid nitrogen, the water in the soil is vitrified in an amorphous solid state. This transition does not cause expansion of the ice which could potentially damage the structure (Penumadu and Dean 2000). The frozen specimens are then placed in a freezing unit with a vacuum chamber and dried by sublimation at a low temperature. Freeze-drying avoids disrupting the structure due to surface tension effects that typically take place during air-drying.

For microstructure analysis using scanning electron microscopy (SEM), small cubic specimens, measuring approximately 5 mm x 5 mm x 5 mm, were cut from UCS samples using a sharp razor blade then frozen at -196 ^{o}C by immersion in liquid nitrogen. The frozen samples were freeze-fractured by hitting a chilled blade placed in the middle of the side of the cube with a small hammer. The resulting pieces were kept in liquid nitrogen before being transferred to the freeze-drier to dry by sublimation for five days. The major advantage of using the freeze-fracturing technique lies in the fact that ice fixes the particle together during the fracturing process and prevents them from moving. Moreover, the fracture plane is determined by the ice itself rather than a weakness zone of the material and crosses all the structures in the soil (Delage et al. 1982). The freeze-drier used in this study is the Labonco FreeZone 6 and vacuum and freezing temperature were 0.25 mBar and -56 ^{o}C, respectively. The dehydrated specimens were secured on aluminum stubs by an adhesive carbon conductive tape. A silver paste was applied, when necessary, on the side of the cubic specimens for ground stripping, and then the specimens were sputter-coated with iridium to avoid charge build-up. Iridium has less texture than gold-palladium coating and improved adhesion.

When the focused electron beam hits the sample, it interacts with the atoms at or near the surface resulting in three main signals: secondary (SE) and backscattered (BSE) electrons which are used for imaging and characteristic X-rays which are used for chemical analysis. The Zeiss NEON 40 EsB High Resolution Field Emission SEM was used in this study in secondary electron detection mode. Secondary electrons are generated by the inelastic scattering of the high voltage electron beam that knocks the electrons out from the atoms. By definition, the energy of secondary electrons is less than 50 eV, and mostly less 10 eV (Goldstein et al. 1992). While secondary electrons are generated throughout the interaction volume, only those produced near the surface have enough energy to leave the sample. This results in high resolution images of surface topography and morphology. The magnification range of the Zeiss NEON 40 EsB High Resolution FE-SEM is X 20 to X 900 000 with a resolution of 1.1 nm which is suitable for the examination of clay particles, their geometric arrangements, and any cementitious products formed as a result of stabilization. Magnifications in the range of 160X, 640X, 2,500X and 15,000X, are representative of one general fabric level, two intermediate fabric levels and one clay arrangement fabric level, respectively, following the microfabric assessment methodology proposed by Al-Rawas and McGown (1999).

Energy-Dispersive X-ray Spectroscopy (EDS) is integrated in the Zeiss NEON SEM and allowed the collection of EDS spectra during SEM observations. The settings included electron beam energy at 5-10 kV, takeoff angle at 35° and elapsed live time for 50-100 second. EDS spectra were used for qualitative elemental analysis; at low magnifications, they reveal the general elemental makeup of the sample, and at high magnifications, EDS can be performed at specific regions to aid identify the feature that is being investigated.

3.5.2 Mercury Intrusion Porosimetry

For the microstructure analysis using MIP, cubic samples were cut from UCS samples and freeze-dried in a similar way as the SEM samples. The dried samples were wrapped in plastic wrap and stored in sealed tubes containing a desiccator before being shipped to the University of Texas at Arlington to be tested. AutoPore IV 9510 mercury intrusion porosimeter from Micromeritics Instrument Corporation (Norcross, GA), capable of providing maximum mercury pressure of 414 MPa and able to measure pore diameter from about 0.003 to 400 μm, was used to quantitatively measure the porosity and pore size distribution of the samples and monitor the microstructural changes for cement-stabilized clays with curing time and in comparison to the untreated samples. Diamond (1970) measured the contact angle of mercury on clays and found it to be 147^o for kaolinite and illite, and 139^o for montmorillonite. More recently, Penumadu and Dean (2000) measured the contact angle of mercury and kaolin clay using the sessile drop technique and found higher values; 162^o for advancing angle and 158^o for receding angle. In this study, the contact angle of 147^o was selected because it is the value that is considered to be more commonly used and accepted (Romero and Simms 2008, ASTM D4404-10). The surface tension of mercury is 485 dynes/cm and its density is 13.5335 g/mL. The MIP test was conducted in two stages, low-pressure and high-pressure stage. First, the dried sample was placed in the penetrometer which was inserted in the low-pressure port and evacuated to a pressure of 6.7 Pa or 50μm Hg (99.993% vacuum).

Then, the penetrometer was filled with mercury by applying a mercury filling pressure of 3.58 kPa (0.52 psia). Finally, the filled penetrometer was placed in the pressure vessel of the porosimeter and the pressure was incrementally increased while recording the absolute pressure and the volume of intruded mercury until the maximum pressure of 414 MPa was reached.

Chapter 4: Results and Discussion

4.1 Unconfined Compression Test

A set of four samples were prepared for the raw soil and for each curing time. A total of twenty four samples were compacted at their respective optimum moisture content and maximum dry unit weight before being stored in a 100% humidity room for moisture homogenization/homogeneity and curing. At a specific curing time, three out of the four samples were tested for unconfined compressive strength (UCS) according to ASTM D 2166 while the last sample was left intact for comparison purposes in subsequent tests. The UCS of the raw and stabilized samples as a function of time is shown in Figure 4.1. The data points represent the average of the three unconfined compressive strength tests while the bars show the range between the minimum and maximum value for strength.

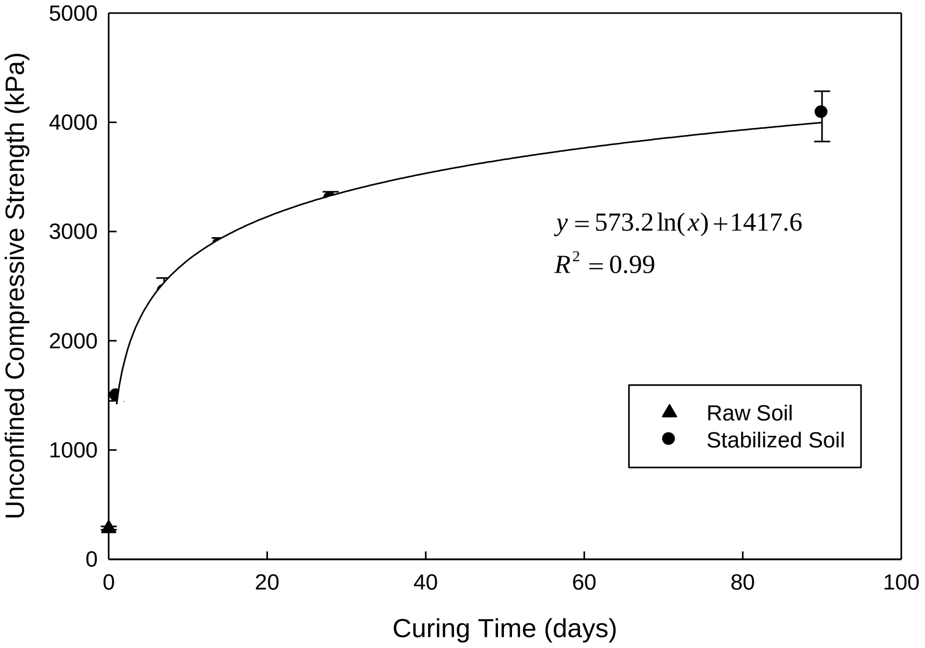

Figure 4.1: Unconfined Compression Strength vs. Time for Stabilized Samples

The repeatability among the samples cured for the same time is very good given the small range bars and reflects nominally identical samples. The strength appears to rapidly increase in early stages of curing and starts leveling off at later stages. This behavior is well-known in the literature and has been reported in several previous studies (e.g. Circeo et al. 1962, Chrysochoou 2014) that concluded that the strength of chemically stabilized soils can be properly captured with a logarithmic trend over time. As seen in Figure 4.1, the logarithmic relationship between unconfined compressive strength and time is excellent, with an R^2 value of 0.99. In order to include the data points for the raw soil in the fitting curve and capture the behavior of all the samples together, a curing time of 0.1 days is used for the raw soil in such a way to keep the fitting nearly unchanged. The modified plot is shown in Figure 4.2.

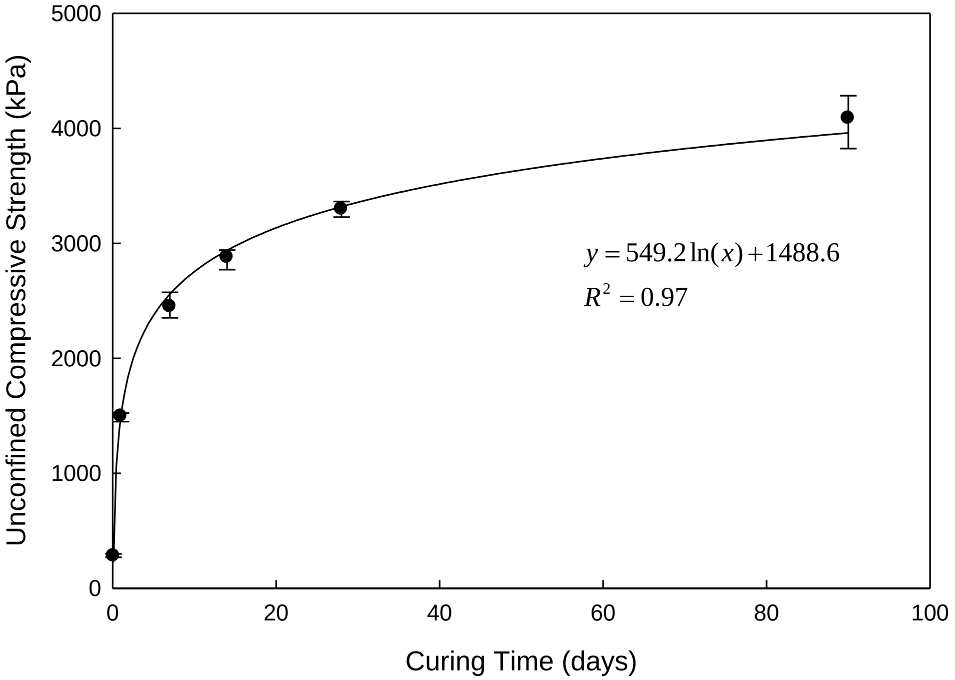

Figure 4.2: Unconfined Compression Strength vs. Time for all Samples

4.2 Thermogravimetric Analysis Test

After each sample was tested in unconfined compression, a small amount of soil was recovered from each sample and mixed with the other samples from the same curing time together to obtain a representative homogeneous powder, which was then dried before being thoroughly pulverized. All the TG tests were performed at a constant heating rate of 10 K/min until 1000 ^{o}C, while the TG analyzer was connected to the online MS for simultaneous evolved gas analysis. Two TG tests were performed for each curing time to assess repeatability. A representative example of the reproducibility of this test is shown in Figure 4.3, and all other figures are presented in Appendix C. The reproducibility of all the TG tests was excellent.

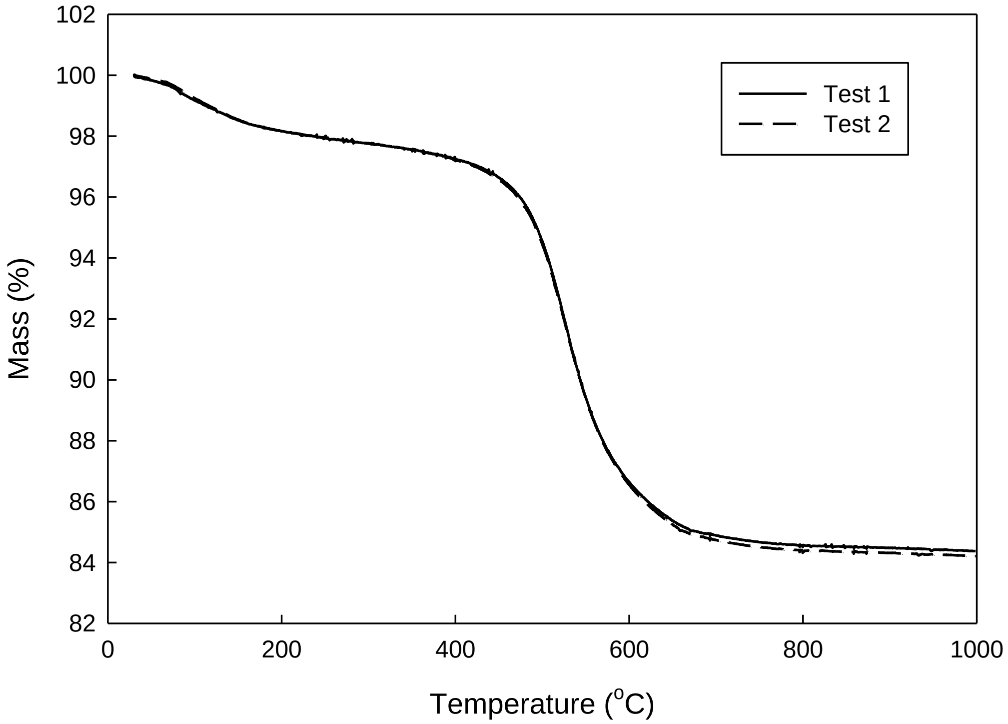

Figure 4.3: TG Repeatability Tests for 7-day Cured Samples

The TG curve alone only shows the mass loss during heating, and small variations in the curve may easily go unnoticed. The DTG curve, which is the derivative of the TG curve, is thus computed to highlight these changes and help detect and differentiate the various reactions. The TG and DTG curves of the raw kaolinite are shown in Figure 4.4.

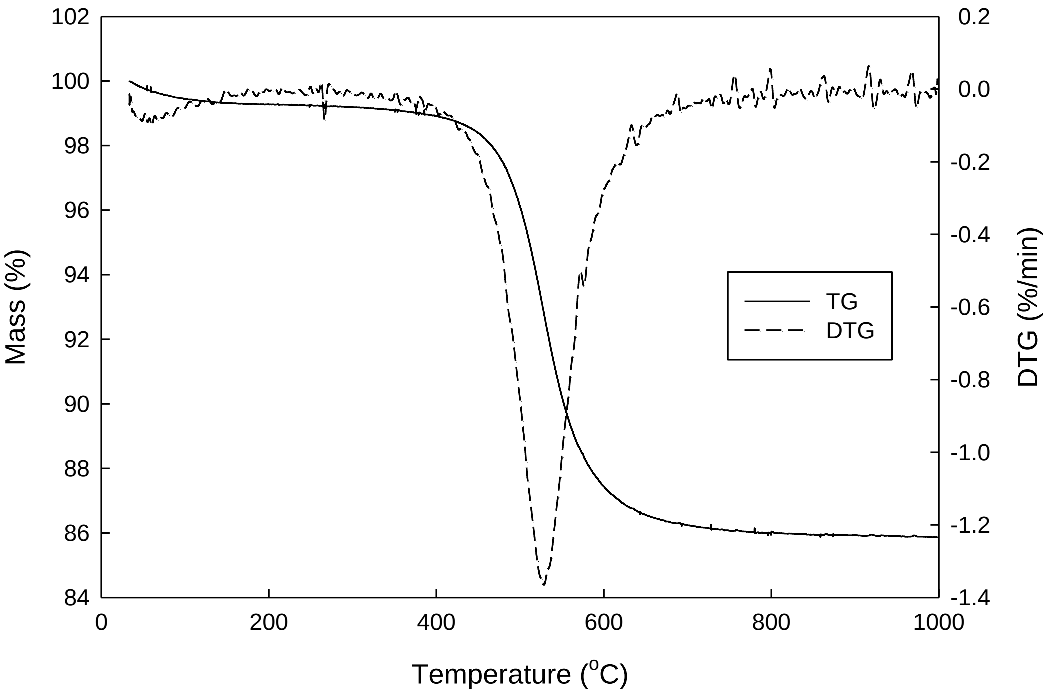

Figure 4.4: TG and DTG Curves of Raw Kaolinite

Two distinct mass losses can be spotted from these curves. The first one is a small peak on the DTG curve that signifies desorption of water below 100 ^oC. Unlike other clay minerals, kaolinite does not have any water or cations in its interlayer, and so the water adsorbed on the external surfaces of the clay particles is removed at this temperature. The second peak is very large and occurs at around 527 ^oC where the rate of the reaction is at its fastest. At this temperature, structural water is removed by dehydroxylation which is considered the major thermal reaction in kaolinite that results in mass loss and the transformation to meta-kaolinite. This reaction is well-known and can be best described as follows (Heide and Földvari 2006):

$$Al_2Si_2O_5(OH)_4 \rightarrow Al_2Si_2O_7 + 2H_2O$$

The theoretical value for mass loss according to this formula is 13.95% but values between 11.2 and 14.5% have been reported in the literature (Hindar et al. 1980, Heide and Földvari 2006, Cheng et al. 2010) and these discrepancies were often attributed to mineral admixtures. In this study the mass loss due to the dehydroxylation of kaolinite, in the 440 to 580 ^{o}C range, is found to be 12.1% which is reasonably close to the theoretical value. Variations in the dehydroxylation temperature and the amount of mass loss depend on several factors such as the degree of disorder of the kaolinite, the particle size, the amount and kind of impurities, the heating rate, the TG instrument, among others (Cheng et al. 2010, Ptacek et al. 2010).

As previously mentioned, the evolution of gas species is analyzed through the use of the coupled TG-MS system. The evolved gas analysis occurs on the basis of degassing profiles at the same temperature range as the TG from ion currents for different mass/charge (*m/z*) ratios, in particular the molecule ions of water (H_2O^+, *m/z* 18) together with fragment ions (OH^+, *m/z* 17, and O^+, *m/z* 16), and carbon dioxide (CO_2^+, *m/z* 44). The mass-spectra curves of these gases for the raw kaolinite are shown as ion current versus temperature in Figure 4.5.

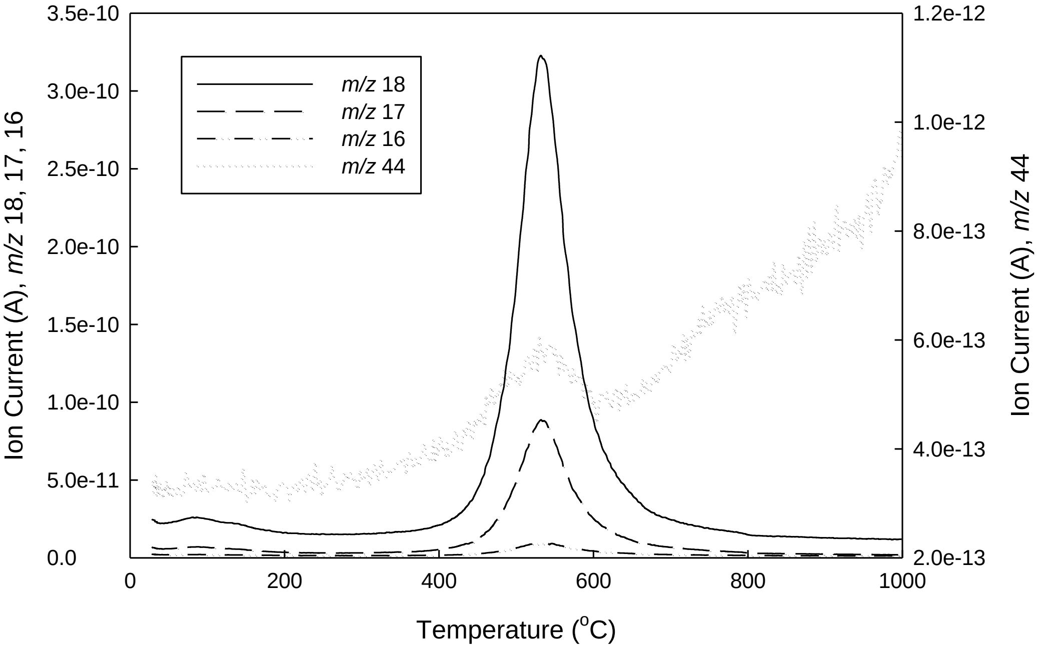

Figure 4.5: MS Spectra for the Raw Kaolinite

Water release is monitored by following the MS curves of the molecule ion water H_2O^+ (*m/z* 18) and the fragment ions OH^+ (*m/z* 17) and O^+ (*m/z* 16). The strong similarity in the trends among these three curves is an indication of the characteristic fragmentation mechanism of water molecule during the ionization process (Heide and Földvari 2006). A small peak below 100 °C and a large peak at around 530 °C are found in all the three curves indicating that water is indeed the gas that is being released from the sample at these temperatures. This conclusion is consistent with the mass loss observed in the TG/DTG curves at similar temperatures which was explained by water desorption at low temperatures and dehydroxylation of kaolinite at the high temperature. The evolution of carbon dioxide is monitored by following the MS curve of the molecule ion CO_2^+ (*m/z* 44). The curve shows a very small peak at the same temperature as the major water peak (about 530 ^{o}C). The presence of carbonates and their decomposition at this temperature are unlikely in the raw kaolinite sample. A possible explanation for the small CO_2 peak is as an artifact related to the water peak. Sometimes when there is a very large peak in the MS curve, such as the water peak in this case, it affects all the other peaks in a similar manner. In other words, when an ionized gas is in the MS in high concentration, some of its ions may get to the detector when the MS is measuring the other masses. The rising background in the ion current curve of *m/z* 44 is likely to be caused by some CO_2 desorption from the walls of the oven as they heat up. The TG and DTG curves of the stabilized kaolinite cured for 1, 7, 14, 28, and 90 days are shown in Figure 4.6 – Figure 4.10, respectively, followed by their corresponding mass-spectra curves of the molecule ions H_2O^+ and CO_2^+ and the fragment ions OH^+ and O^+ illustrated in Figure 4.11 – Figure 4.15.

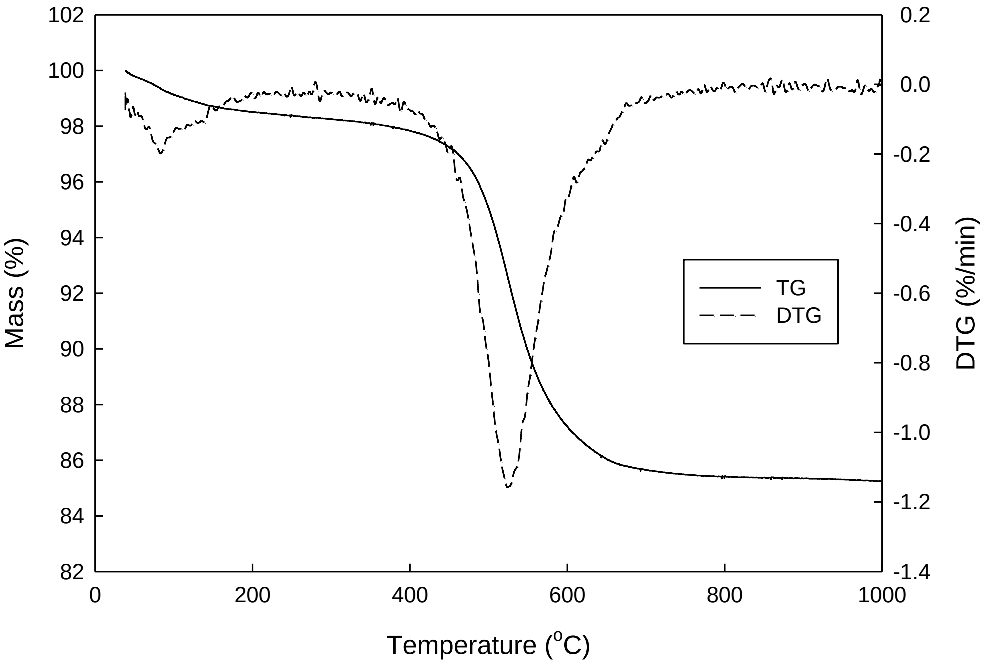

Figure 4.6: TG and DTG Curves of 1-day Cured Stabilized Kaolinite

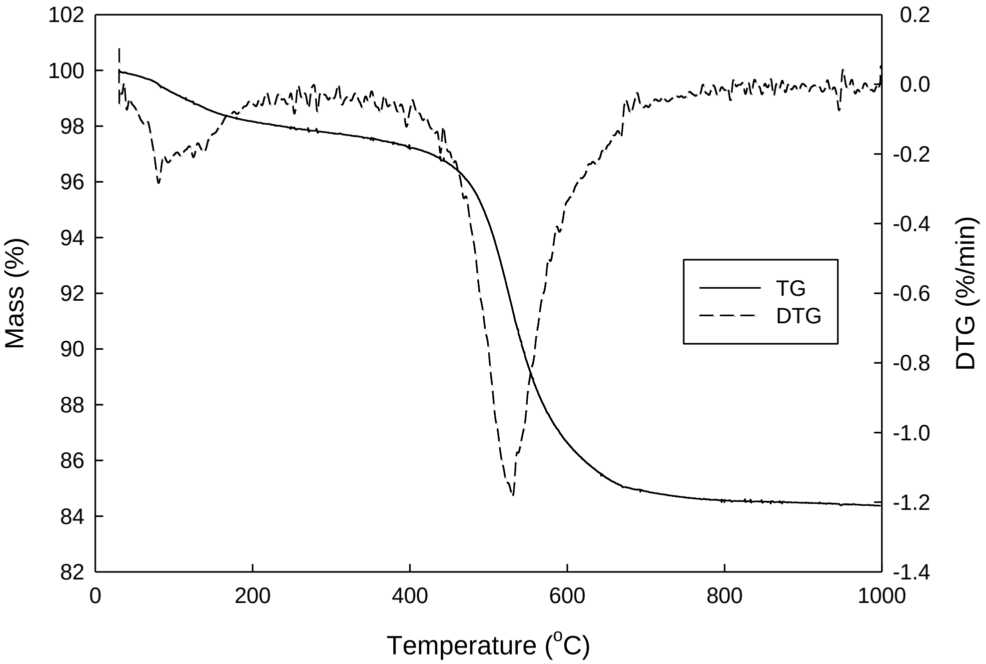

Figure 4.7: TG and DTG Curves of 7-day Cured Stabilized Kaolinite

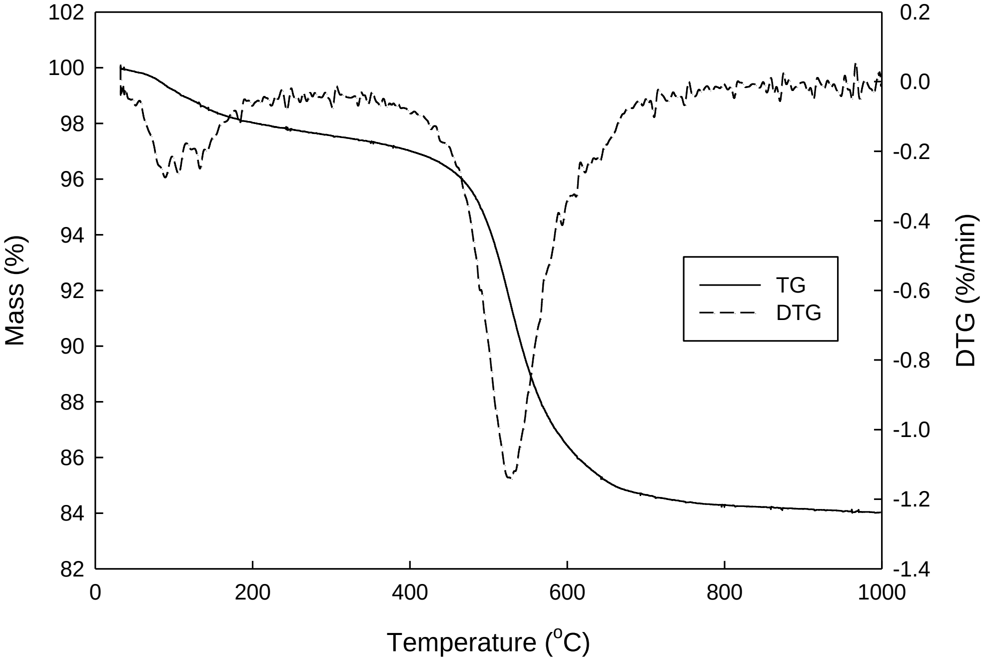

Figure 4.8: TG and DTG Curves of 14-day Cured Stabilized Kaolinite

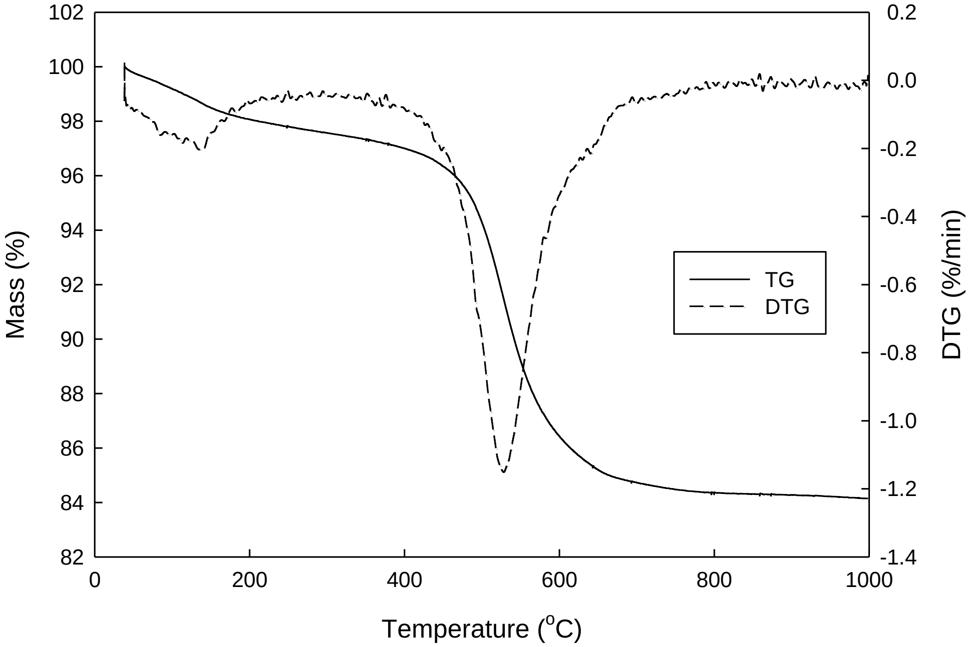

Figure 4.9: TG and DTG Curves of 28-day Cured Stabilized Kaolinite

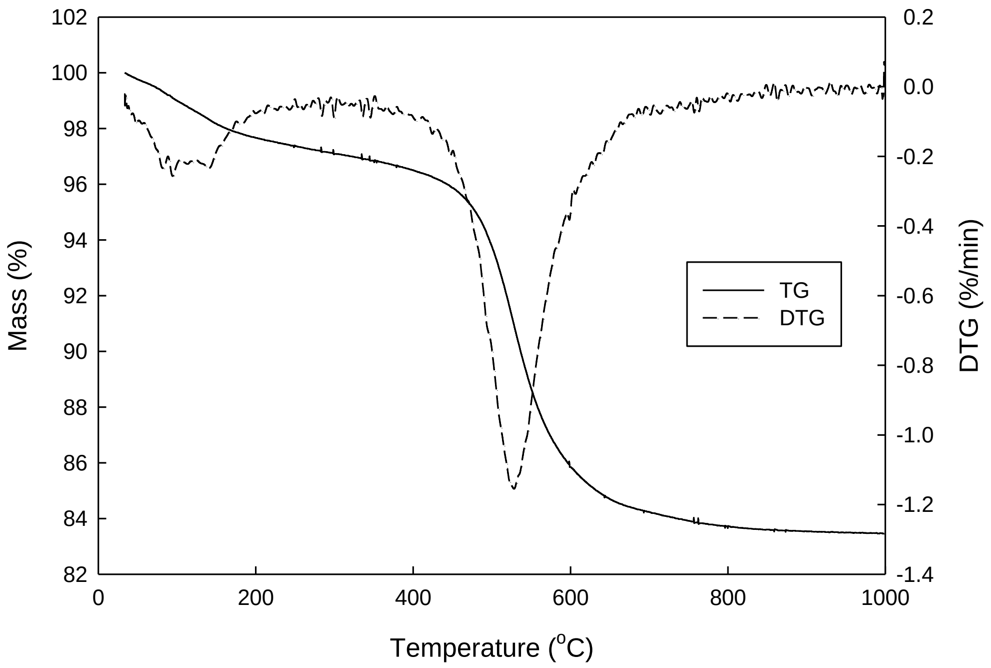

Figure 4.10: TG and DTG Curves of 90-day Cured Stabilized Kaolinite

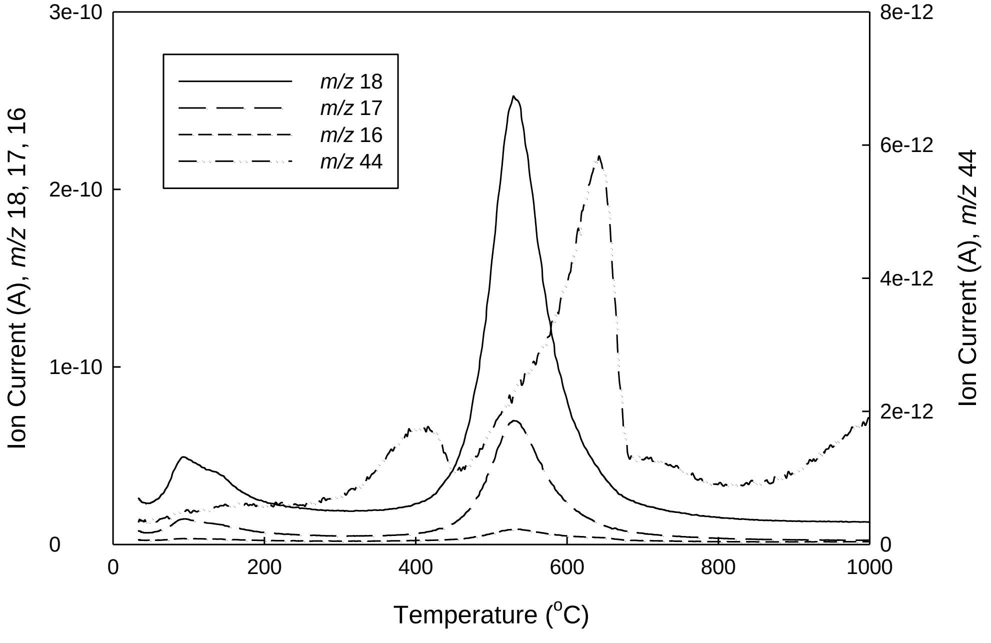

Figure 4.11: MS Spectra for 1-day Cured Stabilized Kaolinite

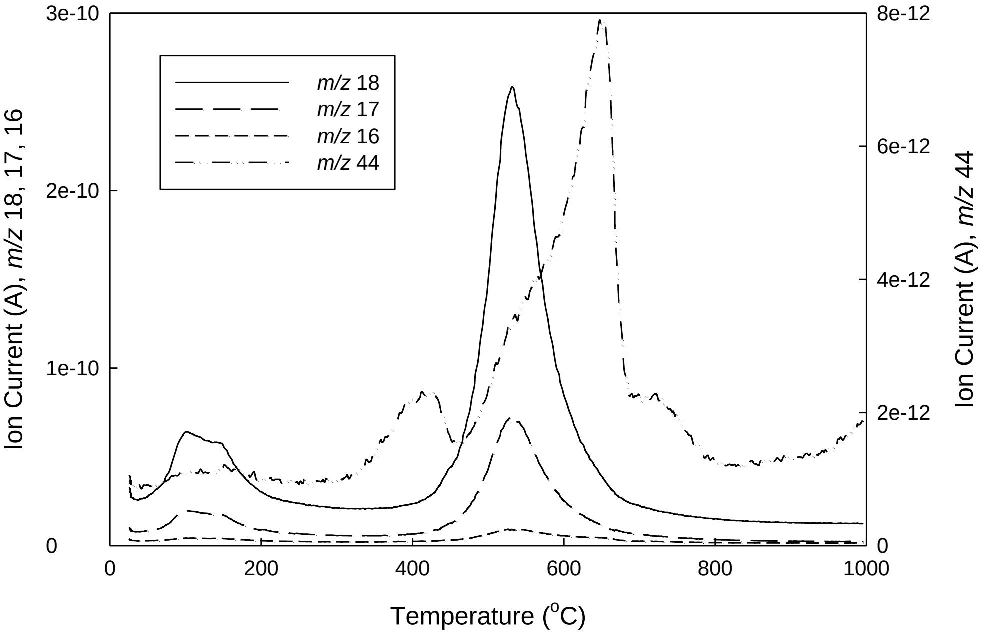

Figure 4.12: MS Spectra for 7-day Cured Stabilized Kaolinite

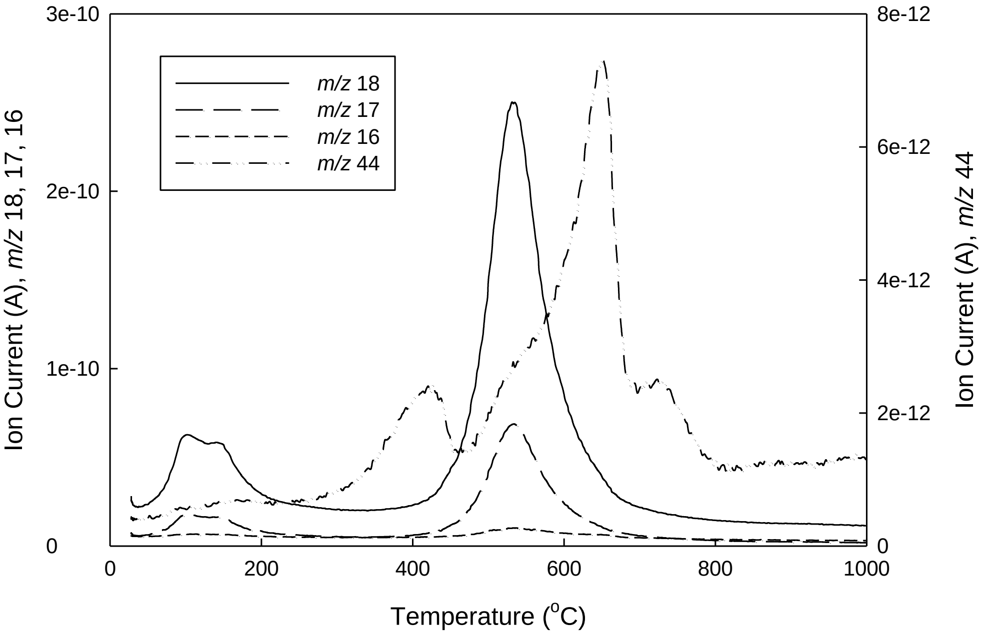

Figure 4.13: MS Spectra for 14-day Cured Stabilized Kaolinite

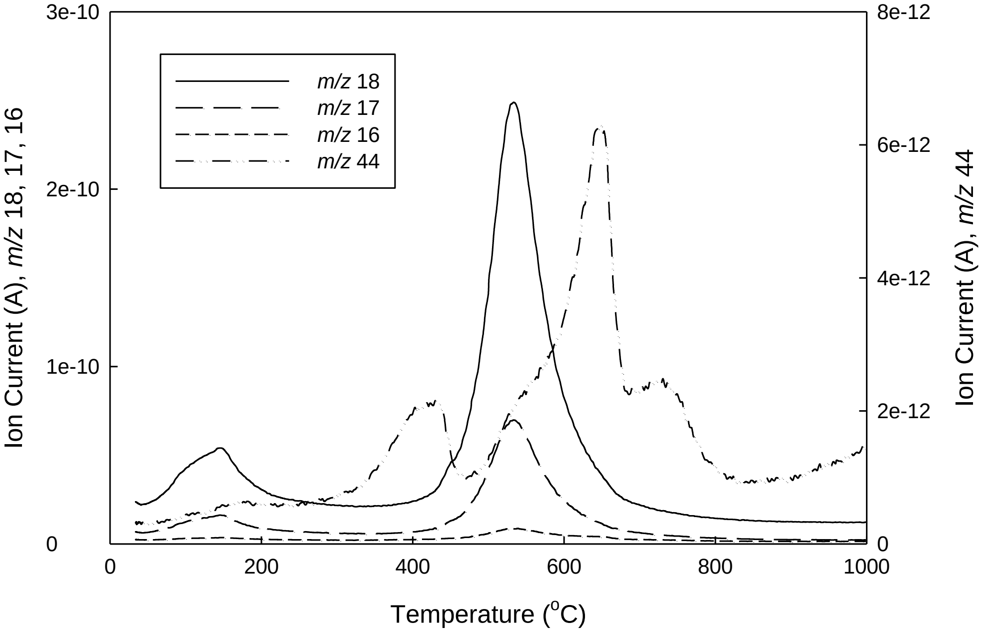

Figure 4.14: MS Spectra for 28-day Cured Stabilized Kaolinite

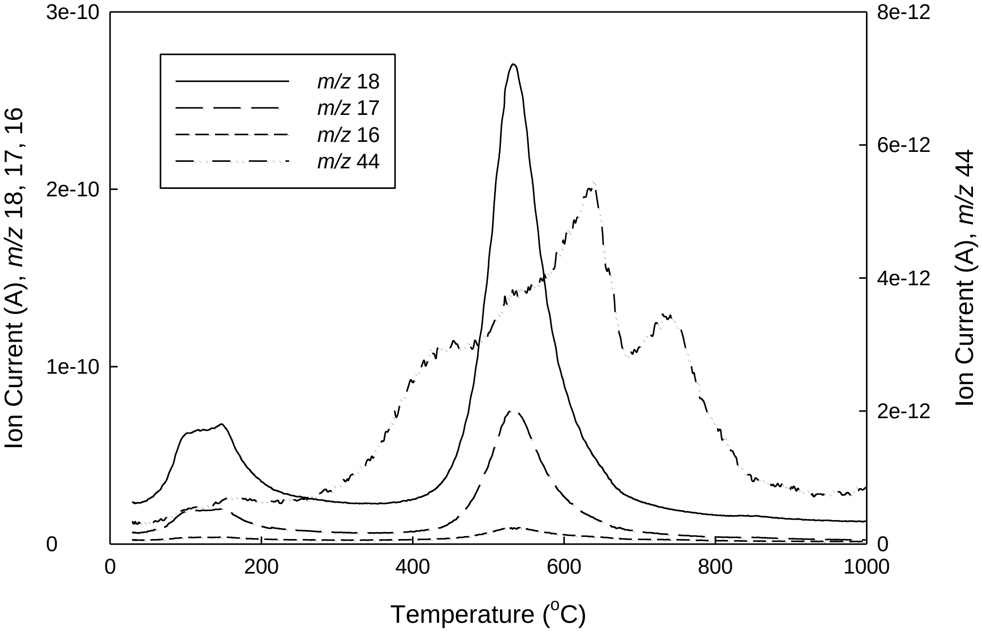

Figure 4.15: MS Spectra for 90-day Cured Stabilized Kaolinite

At first look, the TG/DTG curves of the stabilized soil cured for different times follow similar trends; not very different from the raw kaolinite. The first small peak observed in the raw soil at temperatures below 100 ^oC (Figure 4.4) appears to become larger and wider in the stabilized soil and with increasing curing time (Figure 4.6 – Figure 4.10). In addition, it seems to be composed of several peaks and extends well above 100 ^oC, which indicates that several constituents or phases are present in the soil and being decomposed at this temperature range. El-Jazairi and Illston (1977) indicated that mainly CSH phases, among others, dehydrate at temperatures ranging between 105 and 440 ^oC. More recent studies (Zhou and Glasser 2001, Alarcon-Ruiz et al. 2005) showed that gypsum and ettringite decompose between 110 and 170 ^oC. The location of the major peak at around 527 ^oC does not shift after the soil is stabilized (Figure 4.6 – Figure 4.10), most likely because the quantity of the cement that is added is relatively small (10% by weight) compared to the kaolinite.

Another observation from the curves of the stabilized soil is the presence of a more noticeable shoulder at the right side (higher temperature) of the major peak past 600 ^oC. Calcium carbonate is generally considered to decompose at around 900 ^oC, but in silicate minerals at around 600 to 700 ^oC (Mojumdar 2001, Cheng et al. 2010).

The analysis of the mass-spectra from the molecule ions of water (H_2O^+, *m/z* 18) and carbon dioxide (CO_2^+, *m/z* 44) confirms these observations. A broad water peak starting below 100 ^oC, but extending well above it, and composed of several other small peaks, indicates the desorption of evaporable water and the dehydration from different phases (Figure 4.11 – Figure 4.15). It is followed by a well-defined peak at about 528 ^oC that would typically refer to the decomposition reaction of one compound; however, both calcium hydroxide which originates from cement hydration and kaolinite dehydroxylate at this temperature range. It is interesting to see that the water peak from the dehydroxylation of kaolinite remained practically unchanged despite the addition of cement which reflects the significant overlapping of these two reactions. The MS curve from carbon dioxide (*m/z* 44) reveals mainly three peaks. The first, around 415 ^{o}C, is a small and unexpected peak. However, it is unlikely to be an artifact from the instrument or an accidental contamination because it is consistently present in all the samples. Cheng et al. (2010) encountered carbon dioxide peaks in pure kaolinite samples at this low temperature which were attributed to the decomposition of organic impurities. The raw kaolinite used in this study did not produce such a peak (Figure 4.5) and thus does not seem to contain similar organic impurities. A possible explanation could be carbon dioxide desorption from some basic sites in the clay, caused by the addition of cement, that had adsorbed CO_2 which is an acid gas. The second peak is relatively large and occurs around 646 ^{o}C followed by a small peak at around 723 ^{o}C. Both these peaks are assigned to the decarbonation of calcite ($CaCO_3$) following this reaction:

$$CaCO_3 \leftrightarrow CaO + CO_2$$

Based on cement literature (ASTM C1365, Chen et al. 2006), carbon dioxide diffuses into the solid and dissolves in the pore solution to form carbonate ions (CO_3^{2-}), which in turn react with the calcium ions (Ca^{2+}) supplied by the free lime, portlandite, and/or calcium silicate hydrates to produce calcium carbonate. As noticed in the MS curve of the raw kaolinite, small humps also occur in the CO_2 curve of the stabilized samples at the same temperature as the water peaks (Figure 4.11 – Figure 4.15), most likely as an artifact related to the high concentration of water molecules. In particular, a shoulder is created to the left of the main carbon dioxide peak where it coincides with the major water peak.

For quantitative assessment, the mass loss at each temperature interval was measured from each TG curve and the average was calculated based on duplicate tests. The results are presented in Table 4.1 and Figure 4.16.

Table 4.1: Percentage Mass Loss at Specific Temperature Intervals

	Mass Loss (%)			
Curing Time (days)	32-105 ^oC	105-440 ^oC	440-580 ^oC	580-1000 ^oC
Unstabilized	0.57	1.03	12.11	2.61
1	1.07	1.92	11.01	3.31
7	1.02	2.83	11.08	3.71
14	1.08	3.05	11.14	3.76
28	0.72	3.12	11.08	3.41
90	1.25	3.44	11.24	3.85

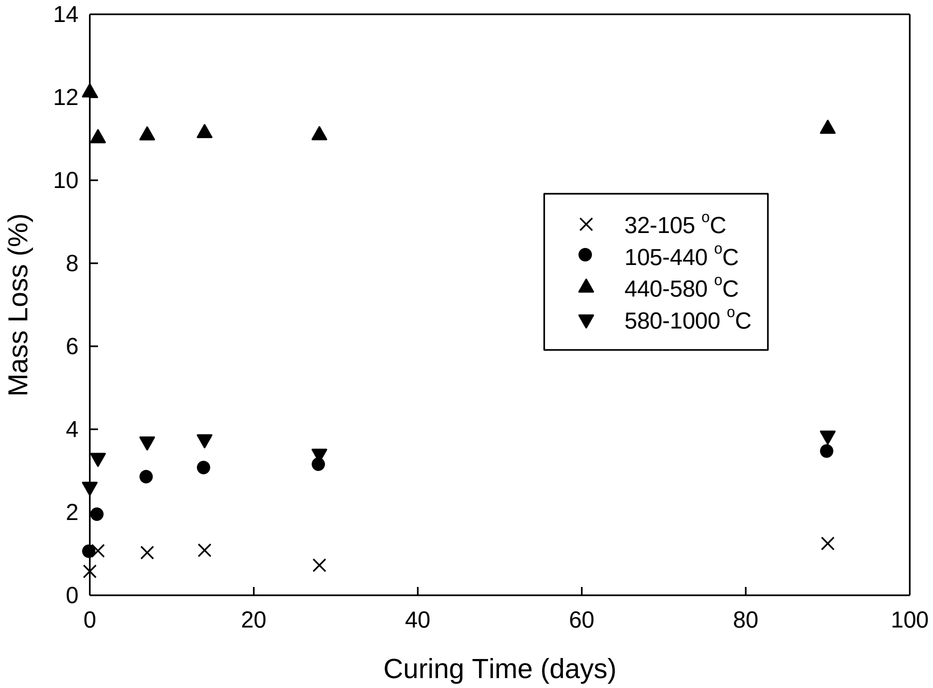

Figure 4.16: Mass Loss at Different Temperature Intervals

The percentage of mass loss appears to be generally increasing with increasing curing time in a logarithmic trend for most temperature intervals. Since the unconfined compressive strength also increases in a similar trend over time, a linear relationship between the unconfined compressive strength and the percentage of mass loss at various temperature intervals is worth investigating and is shown in Figure 4.17 – Figure 4.20.

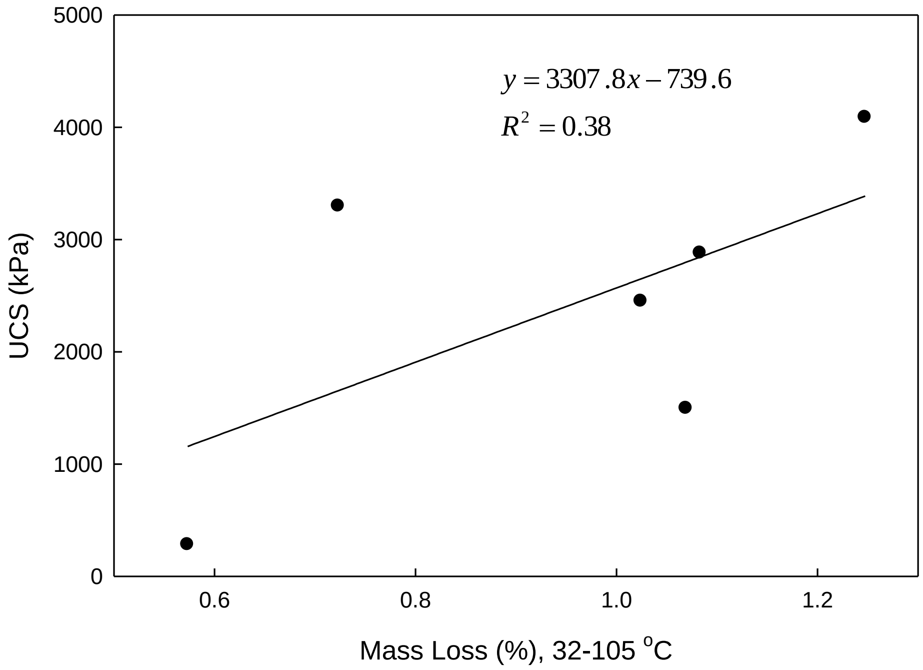

Figure 4.17: UCS vs. Percentage Mass Loss in Temperature Interval 32-105 °C

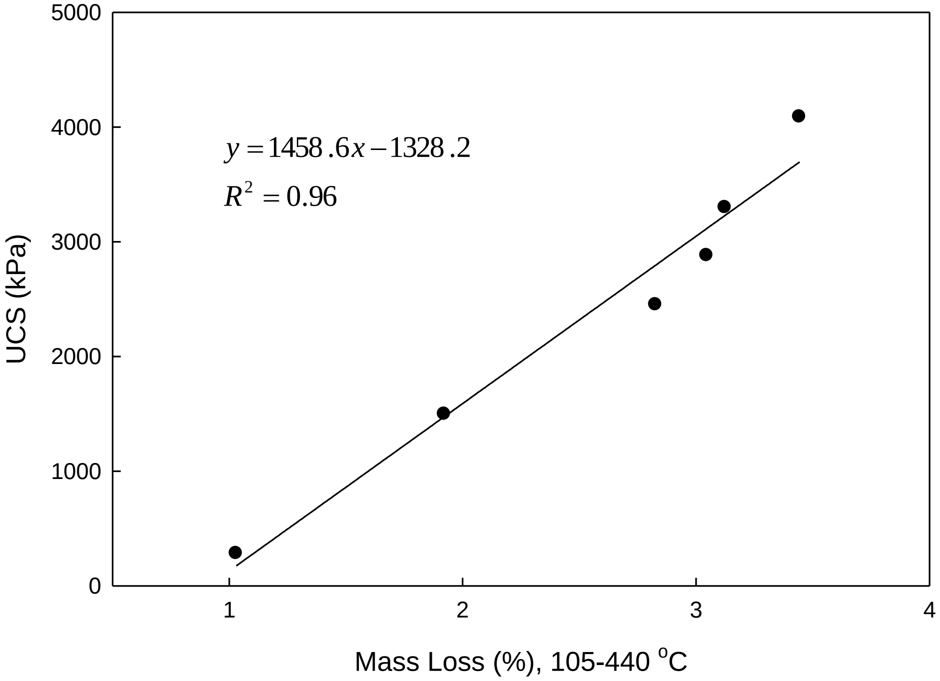

Figure 4.18: UCS vs. Percentage Mass Loss in Temperature Interval 105-440 ^{o}C

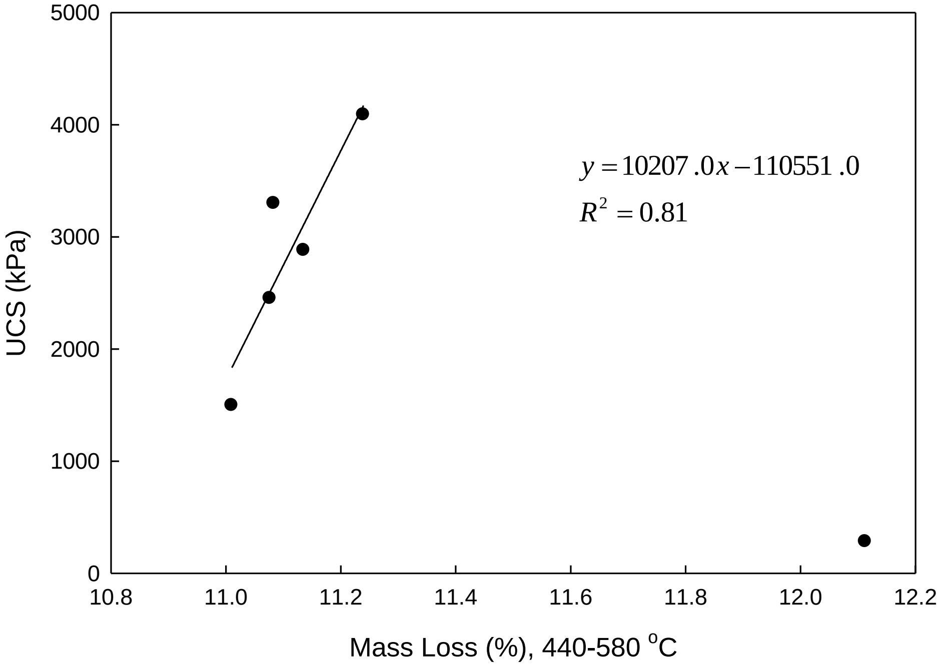

Figure 4.19: UCS vs. Percentage Mass Loss in Temperature Interval 440-580 ^{o}C

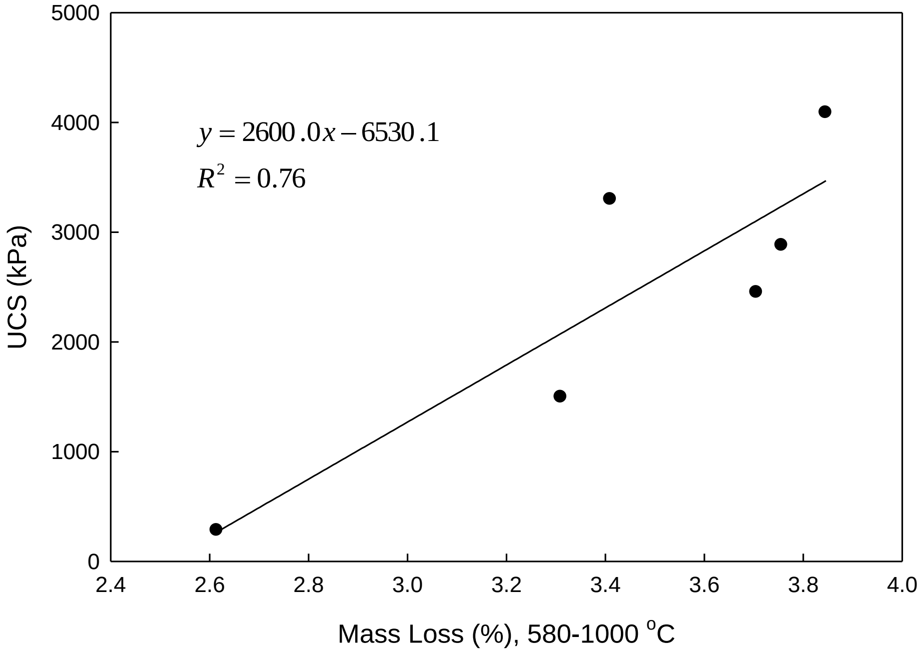

Figure 4.20: UCS vs. Percentage Mass Loss in Temperature Interval 580-1000 ^{o}C

The lack of a trend in the 32-105 ^{o}C interval (Figure 4.17) is expected given the unavoidable variability in moisture content in air-dried samples at the beginning of the test despite trying to closely duplicate the sample preparation and the surrounding conditions. In Figure 4.18, a strong linear correlation with an R^2 value of 0.96 is found between the UCS and the percentage weight loss in the temperature interval 105-440 ^{o}C. The dehydration reactions that take place in this temperature range primarily include the CSH phases which are the major hydration products responsible for strength gain. Other hydration products such as ettringite may also be present and dehydrate at this temperature range. Nonetheless, the mass loss caused by the decomposition of hydration products at the temperature interval 105-440 ^{o}C, namely CSH phases, has an excellent linear correlation with strength gain.

An interesting phenomenon occurs in the temperature interval 440-580 ^{o}C (Figure 4.19) where the mass loss from the raw soil is significantly larger than the mass loss of the stabilized soil at any curing time. A linear correlation between UCS and mass loss in this temperature range, that includes all samples, only yields an R^2 value of 0.43. However, when the mass loss from the raw soil is excluded from the fit, R^2 value is increased to 0.81. Based on cement literature, portlandite or calcium hydroxide dehydroxylates at this temperature range, and as demonstrated in the TG/DTG curve of the raw soil (Figure 4.4), the dehydroxylation of kaolinite also occurs at a similar temperature interval, thus leading to a masking effect of these overlapping peaks. The addition of cement to the kaolinite appears to have a stabilizing effect that renders the kaolinite particles more resistant to heat and decomposition at this temperature range as proved by the reduced mass loss when compared with the raw soil. On the other hand, when only observing the mass loss of the stabilized soil, it appears to increase with curing time (Figure 4.16) and the linear relationship between UCS and mass loss at this temperature range is very good with an R^2 value of 0.81 (Figure 4.19). This suggests that while the addition of cement may have initially made the kaolinite particles more resistant to decomposition through heat, the hydration products, namely calcium hydroxide, that are increasingly produced with time are susceptible to decomposition at this temperature range resulting in a net mass loss that increases with curing time in the stabilized samples. Consequently, the mass loss at this temperature range is adequate for correlation with strength gain over time only among stabilized samples relative to each other rather than with respect to the raw soil that is kaolinite which dehydroxylates at the same temperature range as calcium hydroxide.

The linear correlation between UCS and mass loss at the temperature interval 580-1000 ^{o}C (Figure 4.20) is reasonable with an R^2 value of 0.76. The mass loss in this temperature range is related to the decarbonation of calcium carbonate as previously discussed and demonstrated through the MS curves that show a carbon dioxide peak at this temperature interval. One thing worth noting here is that the precipitation of calcium carbonate is not only limited by the availability supplied by the cement but also the accessibility of carbonate controlled by the diffusion of carbon dioxide into the soil.

Pure cement paste was later prepared and cured under similar conditions as the stabilized samples for TG-MS testing. The TG and DTG curves of the cement paste cured for 1, 7, 14, 28, and 90 days are shown in Figure 4.21 – Figure 4.25, respectively, followed by their corresponding mass-spectra curves of the molecule ions H_2O^+ and CO_2^+ and the fragment ions OH^+ and O^+ illustrated in Figure 4.26 – Figure 4.30.

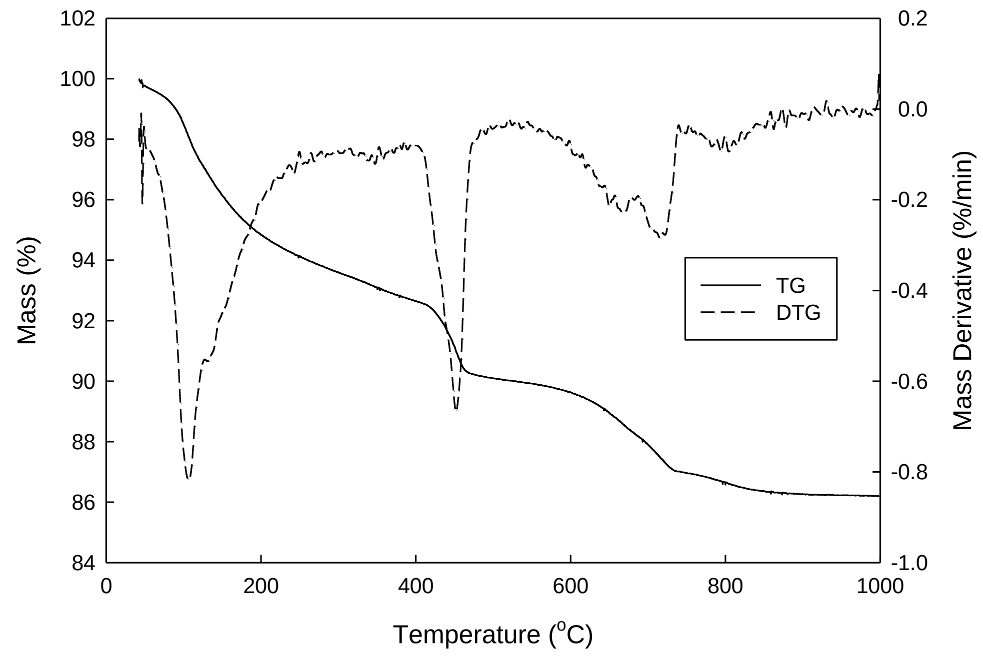

Figure 4.21: TG and DTG Curves of 1-day Cured Cement Paste

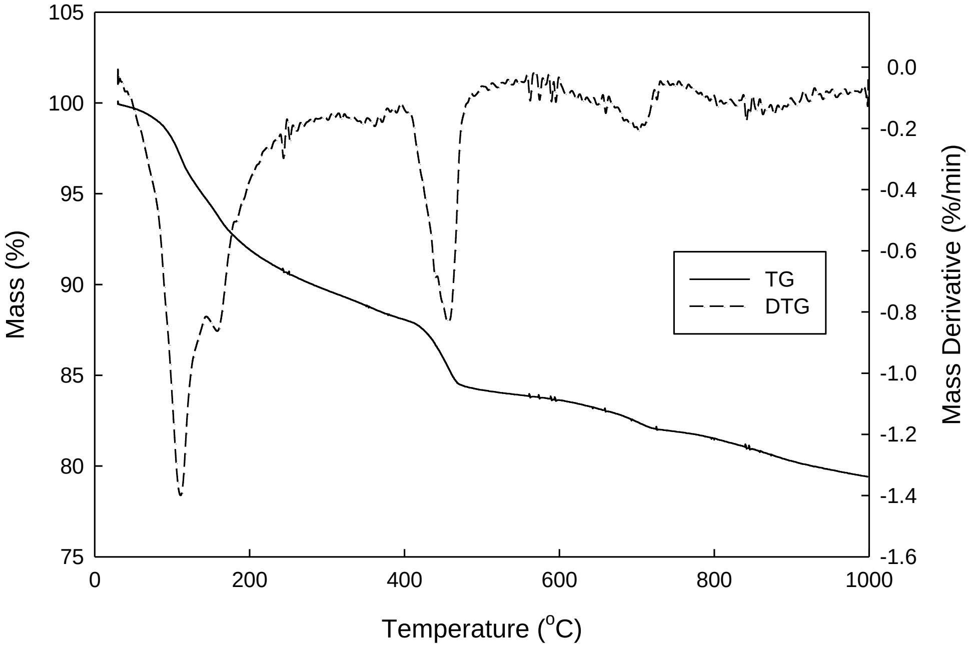

Figure 4.22: TG and DTG Curves of 7-day Cured Cement Paste

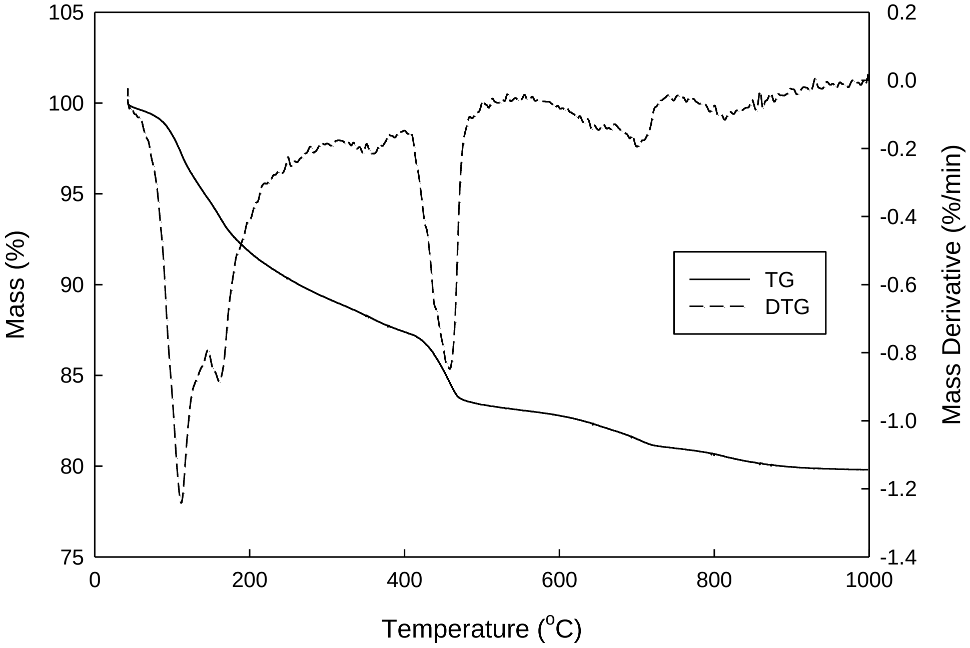

Figure 4.23: TG and DTG Curves of 14-day Cured Cement Paste

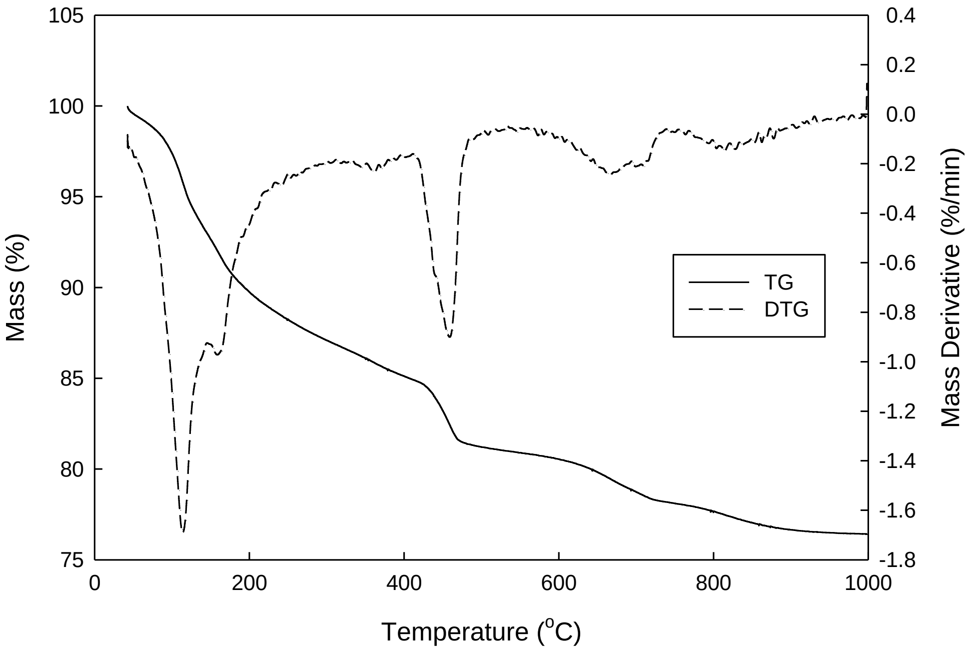

Figure 4.24: TG and DTG Curves of 28-day Cured Cement Paste

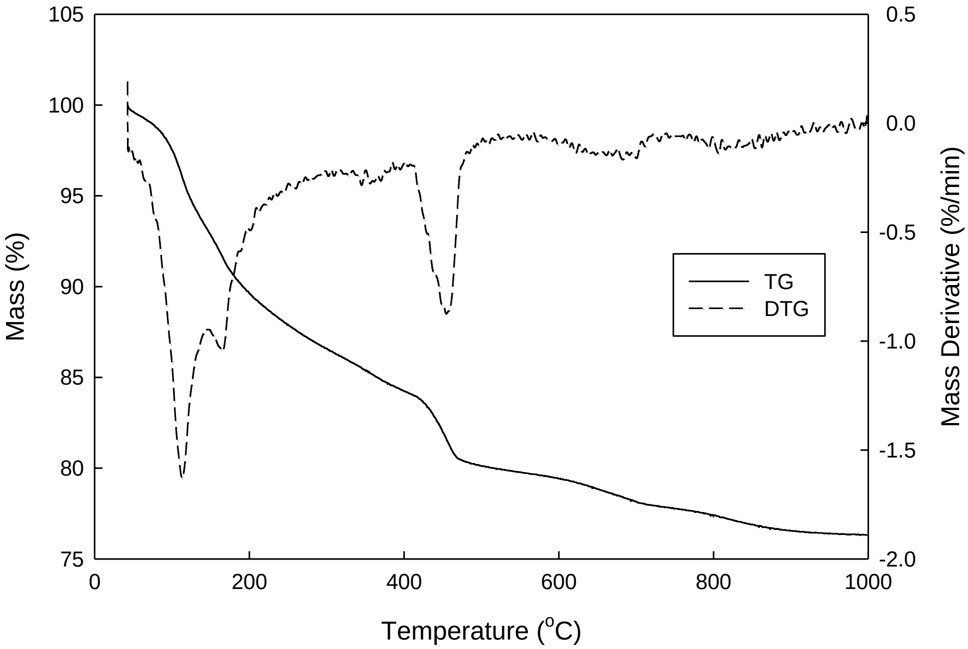

Figure 4.25: TG and DTG Curves of 90-day Cured Cement Paste

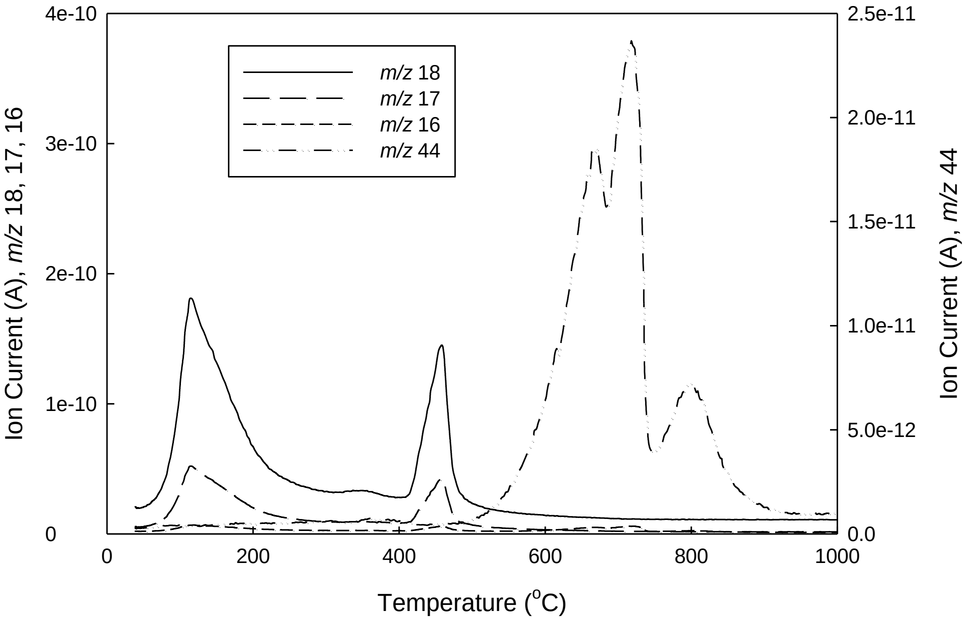

Figure 4.26: MS Spectra for 1-day Cured Cement Paste

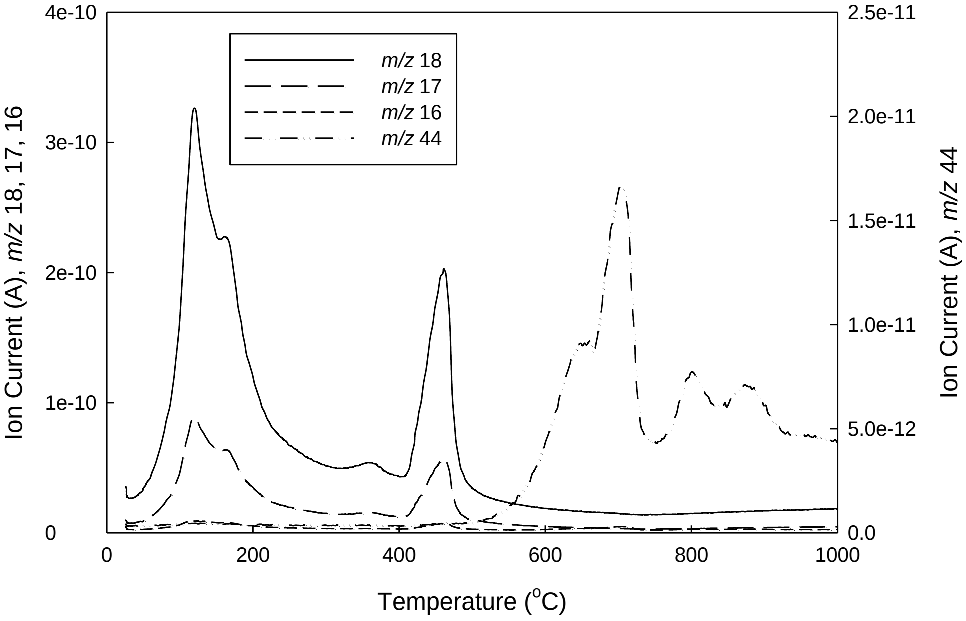

Figure 4.27: MS Spectra for 7-day Cured Cement Paste

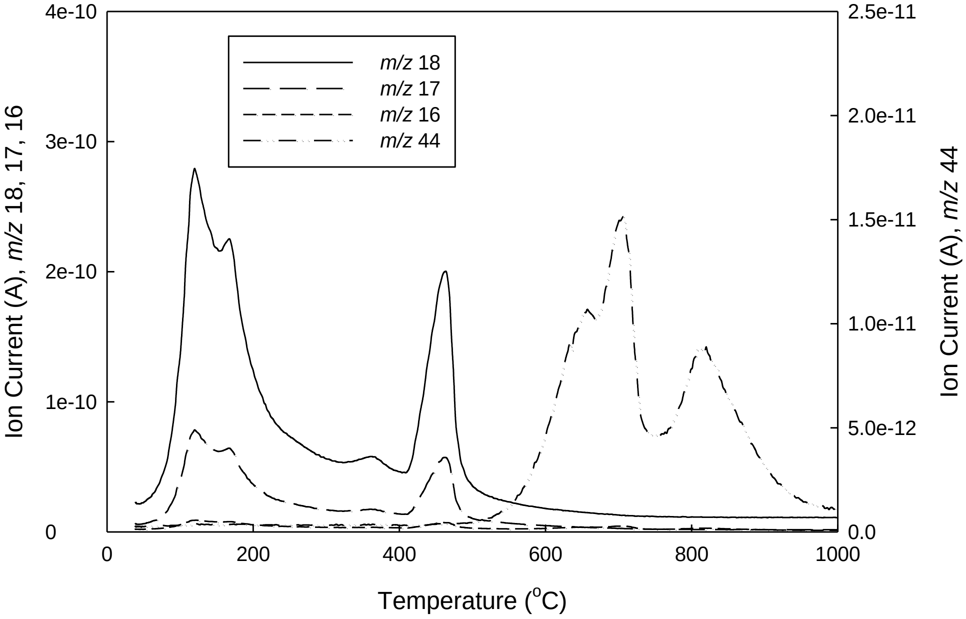

Figure 4.28: MS Spectra for 14-day Cured Cement Paste

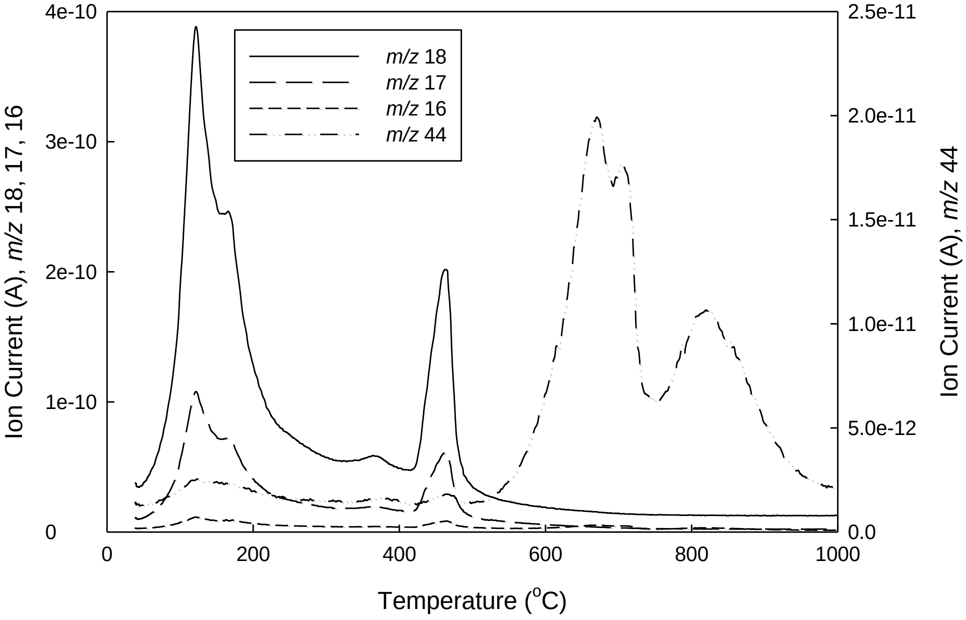

Figure 4.29: MS Spectra for 28-day Cured Cement Paste

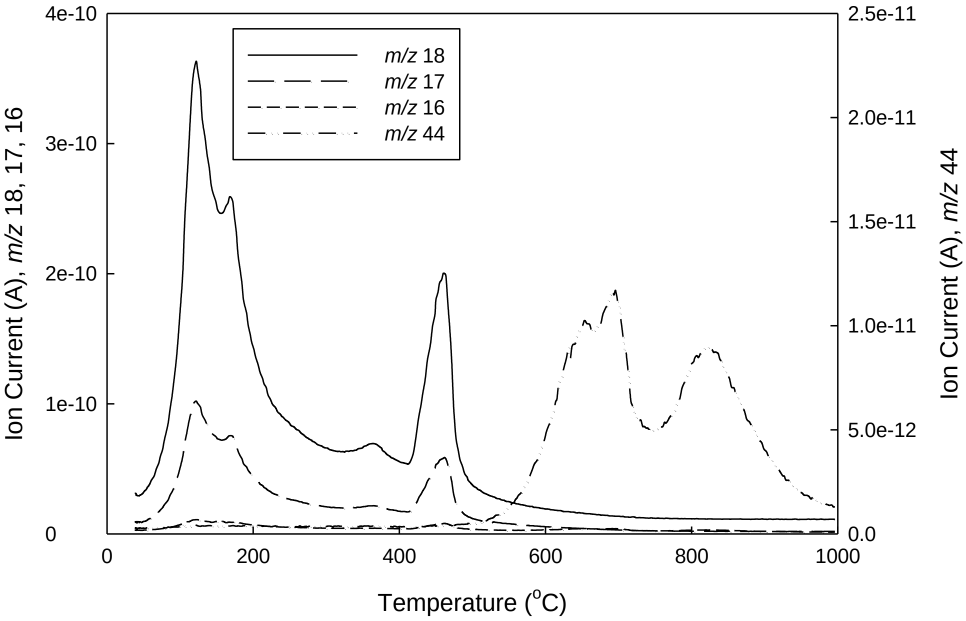

Figure 4.30: MS Spectra for 90-day Cured Cement Paste

The TG/DTG curves of cement paste cured over time (Figure 4.21 – Figure 4.25) reveal more noticeable variations than the TG/DTG of stabilized soil samples (Figure 4.6 – Figure 4.10). The complex nature of cement paste, in terms of the number of different phases and their varying degree of crystallinity and overlapping, results in a continuous mass loss at different rates throughout the entire temperature range during the dynamic TG test. Thus, a reaction may not be fully completed by the time the next one starts. Nonetheless, several peaks can be identified from Figure 4.21 – Figure 4.25. Right from the start of the test, the DTG curve shows a sharp decrease until reaching a peak around 110 ^{o}C. The mass loss up to this temperature is mostly due to evaporable water. Beyond this point, the mass loss continues to increase and a small shoulder starts to form, and then a peak becomes obvious around 158 ^{o}C, followed by another at approximately 354 ^{o}C. All these peaks mostly represent the dehydration of various CSH phases. El-Jazairi and Illston (1977) also identified AH_3 and C_3AH_6 phases around 271 ^{o}C and 350 ^{o}C, respectively, when running isothermal TG test on high alumina cement. In another study on the supercritical carbonation of calcium aluminate cement, Fernandez-Carrasco et al. (2008) also identified AH_3 and C_3AH_6 in the temperature range 150-475 ^{o}C. These phases could also be present in ordinary Portland cement paste, albeit in lesser quantities, and contribute to the mass loss. The calcium hydroxide peak occurs at approximately 455 ^{o}C and shows a well-defined water peak in the MS curve. Past this point, the MS curve of water gradually plateaus while the MS curve of the carbon dioxide picks up. Two peaks are visible on the DTG curve at approximately 700 and 816 ^{o}C signaling the decarbonation of calcium carbonate which is accompanied by the presence of similar peaks in the MS curve of carbon dioxide.

In order to better overlap and compare the results from the cement paste to the stabilized soil, the same temperature ranges are used to measure the mass loss from each TG curve then the average is calculated based on duplicate tests. The results are presented in Table 4.2 and Figure 4.31.

Table 4.2: Percentage Mass Loss of Cement Paste at Specific Temperature Intervals

	Mass Loss (%)			
Curing Time (days)	32-105 ^{o}C	105-440 ^{o}C	440-580 ^{o}C	580-1000 ^{o}C
1	2.07	7.53	2.30	4.21
7	3.31	13.67	3.68	5.25
14	2.76	14.85	3.90	4.00
28	3.91	17.01	4.18	5.23
90	3.89	18.68	4.26	4.52

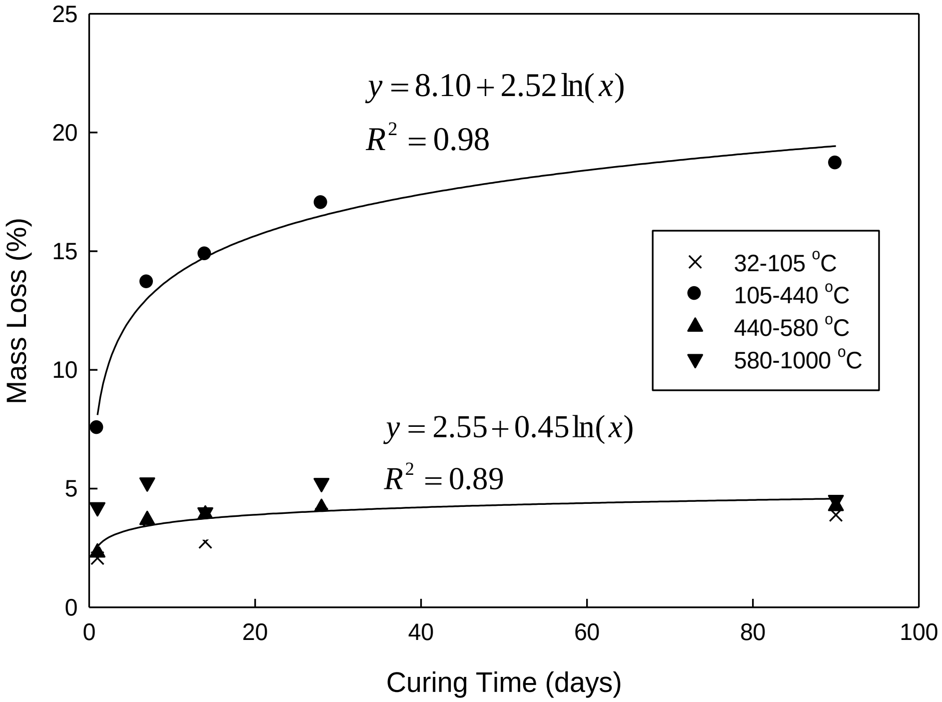

Figure 4.31: Mass Loss in Cement Paste at Different Temperature Intervals

The percentage of mass loss appears to be increasing with increasing curing time, but in particular for temperature intervals 105 to 440 ^{o}C and 440 to 580 ^{o}C, the trend is logarithmic and the fit is excellent with R^2 values of 0.98 and 0.89, respectively. As previously mentioned, the mass loss at the temperature interval 32-105 ^{o}C is not reliable due to the uncontrollable moisture loss in air-dried samples. No unconfined compression tests were performed on concrete samples, but if the gain in strength in stabilized samples is assumed to be due to the addition of cement, then the mass loss in cement paste should correlate well with the UCS of stabilized samples. In addition, it is well-known that the strength in concrete also increases in a logarithmic fashion over time and thus, a linear relationship between the unconfined compressive strength of the stabilized samples and the percentage of mass loss in cement paste is suggested and illustrated in Figure 4.32 – Figure 4.34.

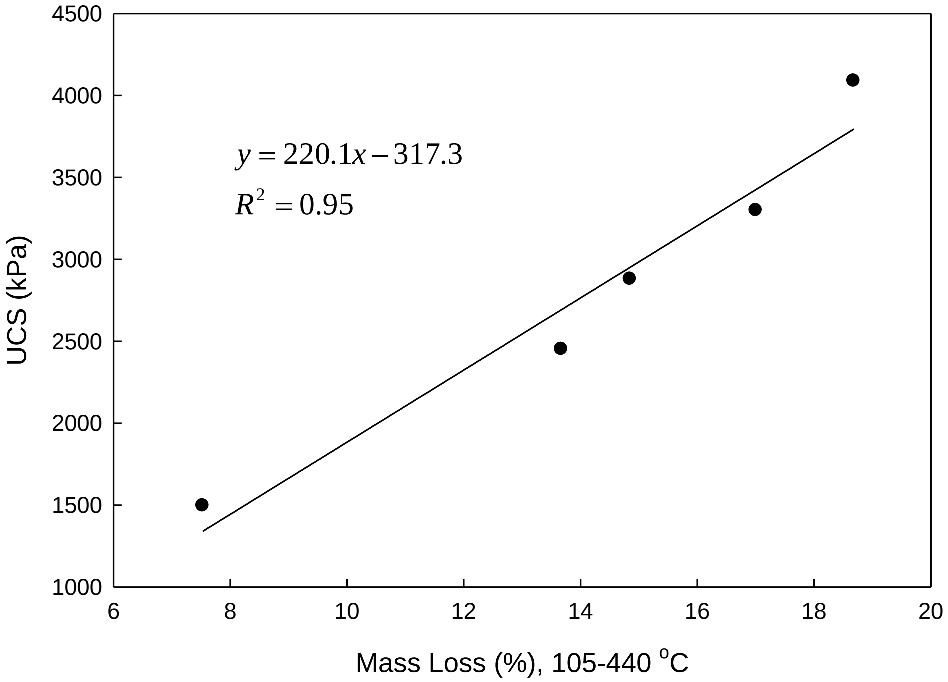

Figure 4.32: UCS of Stabilized Samples vs. Mass Loss in Cement Paste (105-440 ^{o}C)

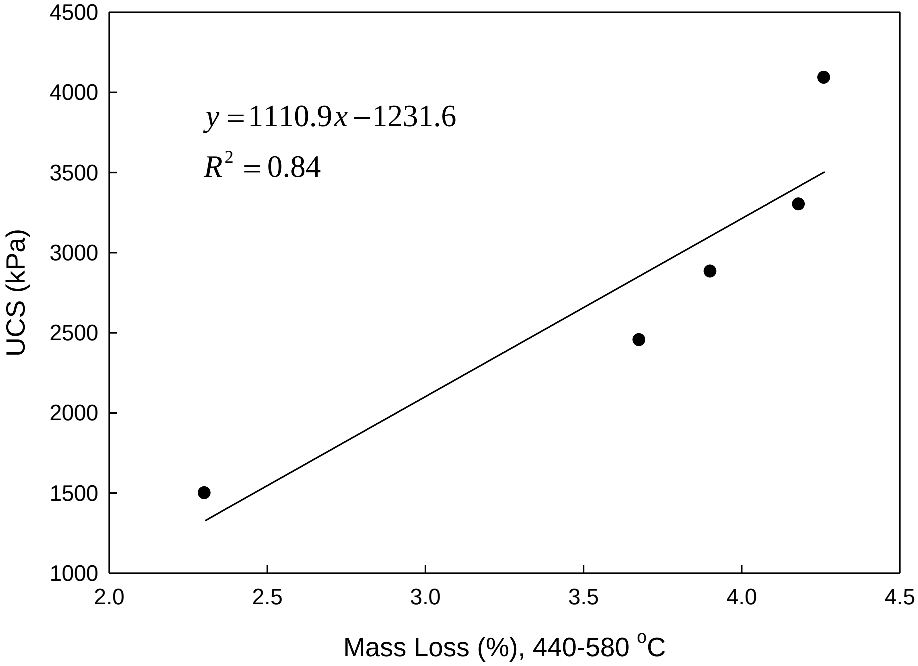

Figure 4.33: UCS of Stabilized Samples vs. Mass Loss in Cement Paste (440-580 °C)

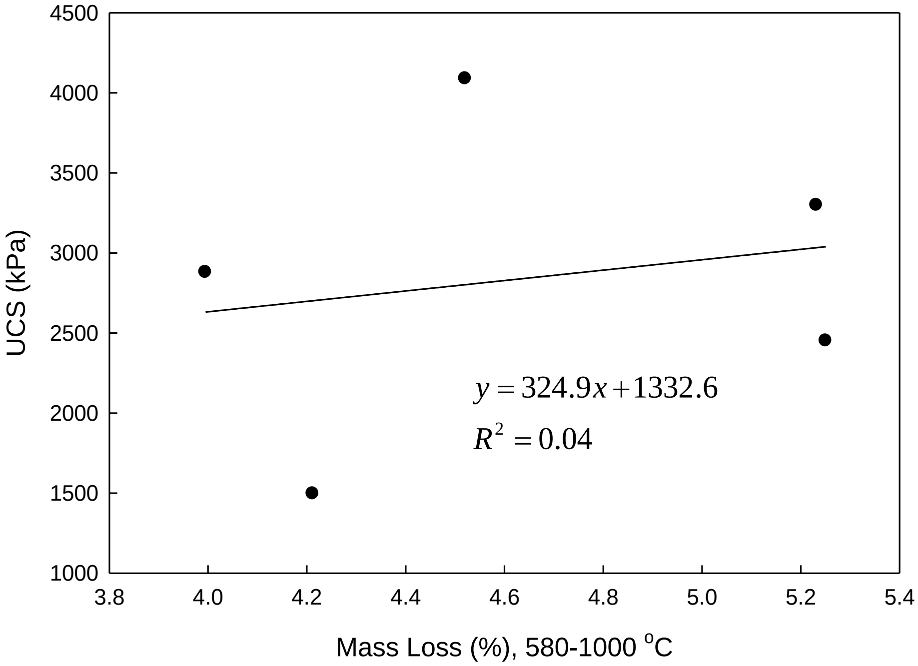

Figure 4.34: UCS of Stabilized Samples vs. Mass Loss in Cement Paste (580-1000 °C)

As expected, a strong linear relationship with an R^2 value of 0.95 is found between the UCS of stabilized samples and the percentage mass loss in the temperature interval 105-440 ^oC. The major hydration product responsible for strength gain, namely CSH, dehydrates at this temperature interval, among other possible hydration products such as ettringite and CAH (e.g. C_3AH_6). Thus it is only reasonable to obtain this excellent linear correlation between the two. Similarly, since calcium hydroxide (CH) is the other major hydration phase that dominates the properties of cement paste, the linear correlation between amount of CH, as calculated from the mass loss between 440 and 580 ^oC, and the UCS of stabilized samples is very good with an R^2 value of 0.84. An interesting observation, however, is that the goodness of fit of these two linear regressions in terms of R^2, is practically identical for the correlation of UCS of stabilized samples with their respective mass loss ($R^2 = 0.92$ for CSH and $R^2 = 0.81$ for CH), and the correlation of UCS of stabilized samples with the mass loss in cement paste ($R^2 = 0.95$ for CSH and $R^2 = 0.84$ for CH). Finally, the linear correlation between UCS of the stabilized samples and the mass loss at the temperature interval 580-1000 ^oC (Figure 4.34) is practically non-existent with an R^2 value of 0.04. As previously discussed, the mass loss in this temperature range is related to the decarbonation of calcium carbonate which is controlled by the diffusion of carbon dioxide into the soil that is susceptible to inconsistency during sample preparation and handling rather than only being dependent on elements readily present in the soil-cement-water mixture.

4.3 Mineralogy

XRD tests were performed on randomly oriented samples of raw kaolinite and cement-stabilized kaolinite mixed with an internal standard (corundum). The internal standard was used to aid in the quantification process and determine the amorphous content of the sample (De La Torre et al. 2001, Chrysochoou 2014).The data was collected between two-theta values of 2^o to 70^o for qualitative and quantitative analysis using Jade software (MDI Jade 10) with reference to the patterns of the International Center of Diffraction Data (ICDD) and the American Mineralogist Crystal Structure Database. Plots of representative XRD patterns of the raw soil and the stabilized samples are presented in Figure 4.35. Identified minerals are marked on the XRD patterns and represented with the following symbols: K = Kaolinite, C = Corundum, P = Portlandite ($Ca(OH)_2$), and Ca = Calcite ($CaCO_3$). As expected, the characteristic peaks of kaolinite and corundum are directly seen in all samples. Portlandite and calcite are detected in most the stabilized samples but not all. For instance, portlandite is not detected in any of the 90-day cured samples, and in one specimen in each of the 1-day, 14-day, and 28-day cured samples. It should be noted that in some cases, a small portlandite peak was actually visible but not detected by Jade. Also, in one of the 28-day cured samples, calcite was not detected. CSH, which is the main cementitious product responsible for strength gain, along with CAH and CASH were not observed in any of the XRD patterns. This phenomenon was reported in several previous studies (Choquette et al. 1987, Al-Rawas 2002, Chrysochoou 2014). In fact, only poorly-crystallized CSH can be formed at room temperature making it hard to detect using XRD (Glenn 1967, Diamond and Kinter 1965). Well-crystallized tobermorite (CSH) was reported by Glenn (1967) in mixtures of montmorillonite and lime cured for several years and under hydrothermal conditions at a temperature of 170 ^{o}C. These conditions, however, are not typically encountered in normal geotechnical engineering applications. The lack of new reflections on the diffractograms is not necessarily an indication of the absence of these phases but could be the result of the poorly crystalline, very disordered structure of these phases, their variable composition, and/or their very low concentration, collectively referred to as amorphous. In addition, the intensity of the primary kaolinite peaks at 12.35^{o} and 24.85^{o} two-theta (7.16 and 3.58 Å) decrease with curing time with respect to the main corundum peaks at 35.14^{o} and 43.36^{o} two-theta (2.552 and 2.085 Å) but none of the kaolinite peaks totally disappeared. This observation indicates that kaolinite is losing crystallinity and/or decreasing in amount since the internal standard is added to all samples at a constant concentration (20% by weight). Similar results have been reported in previous studies (Choquette et al. 1987, Chrysochoou 2014). When cement reacts with the water in the soil, lime is released and leads to a sharp increase in the pH of the pore solution. Silica and alumina become soluble and clay particles are subsequently attacked in these highly alkaline environments. As a result, the released elements from the clay particles combine with the calcium provided by the cement to form amorphous CSH, CAH, and CASH.

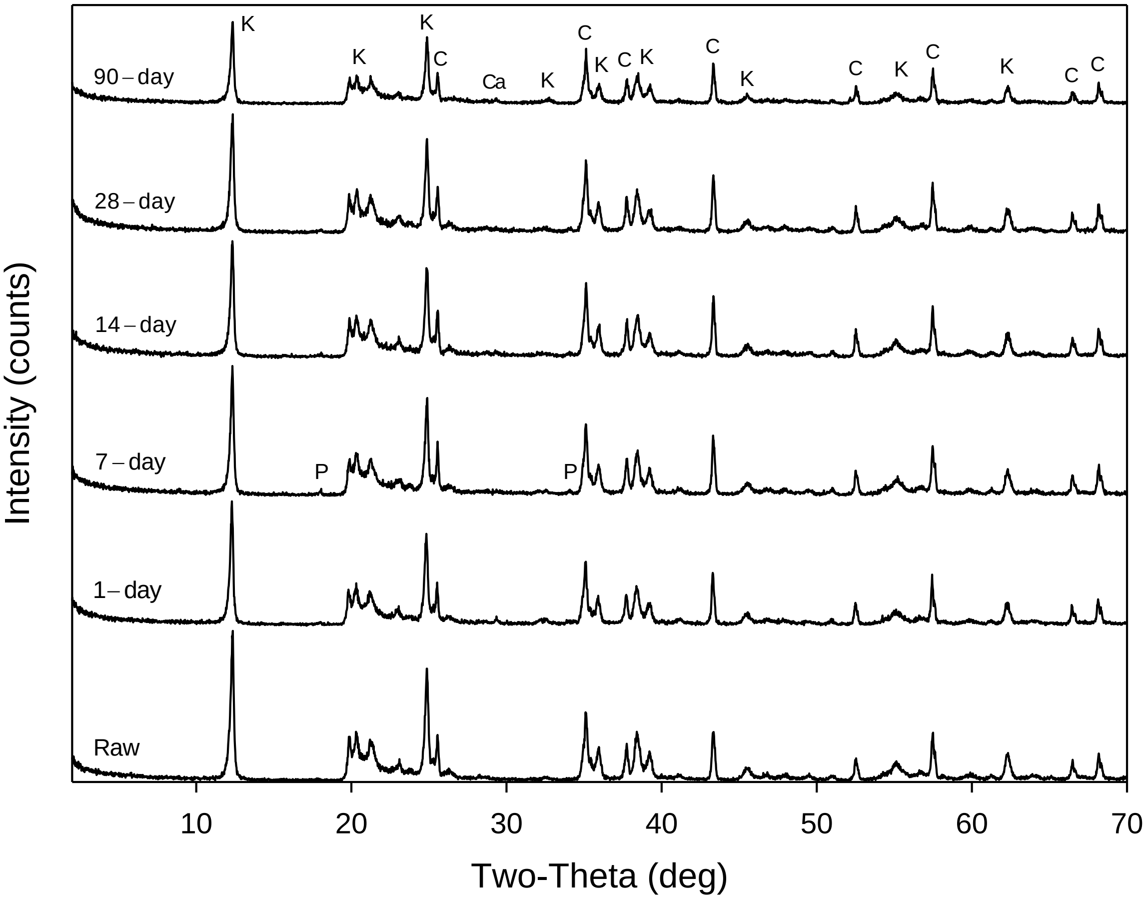

Figure 4.35: X-Ray Diffraction Patterns of Raw and Stabilized Samples*
*K, kaolinite; C, corundum; P, portlandite; Ca, calcite

In the following step, Jade software (MDI Jade 10) was used to analyze the XRD patterns by applying the whole-pattern fitting method in an attempt to quantify the existing minerals as well as the amorphous content through the use of the internal standard. Representative XRD patterns of the raw soil, the 7-day and 90-day cured samples are presented in Figure 4.36, Figure 4.37, and Figure 4.38, respectively. The rough black line represents the observed pattern while the overlaid pink smooth line represents the calculated pattern. The difference between the observed and calculated patterns is shown above them. If the fit was perfect, then the difference plot would be a flat line. The lack of large peaks in the difference plot signifies a good agreement between the observed and calculated patterns.

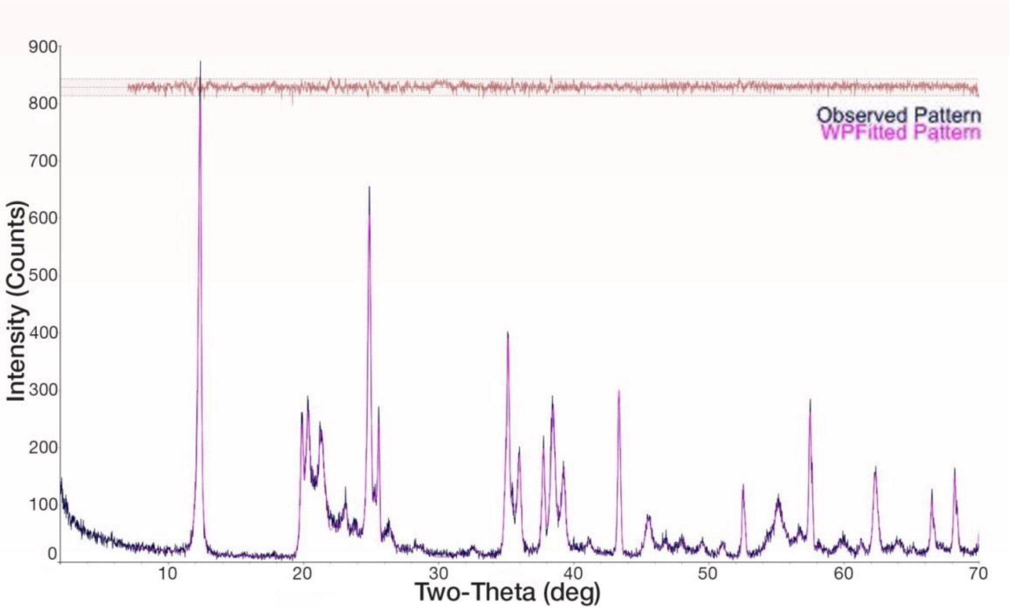

Figure 4.36: X-Ray Diffraction Pattern of Raw Kaolinite

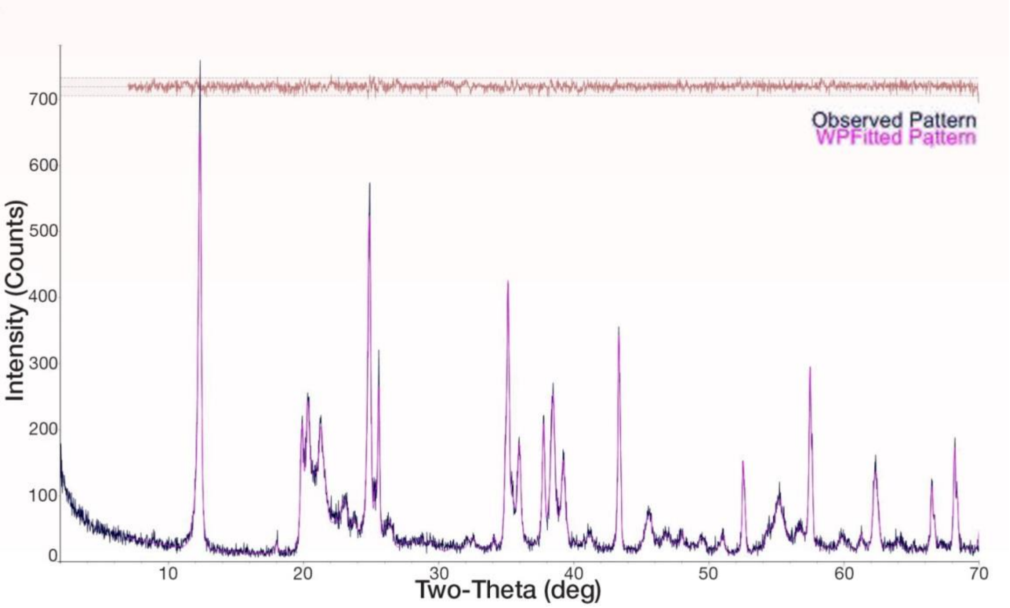

Figure 4.37: X-Ray Diffraction Pattern of 7-day Cured Stabilized Sample

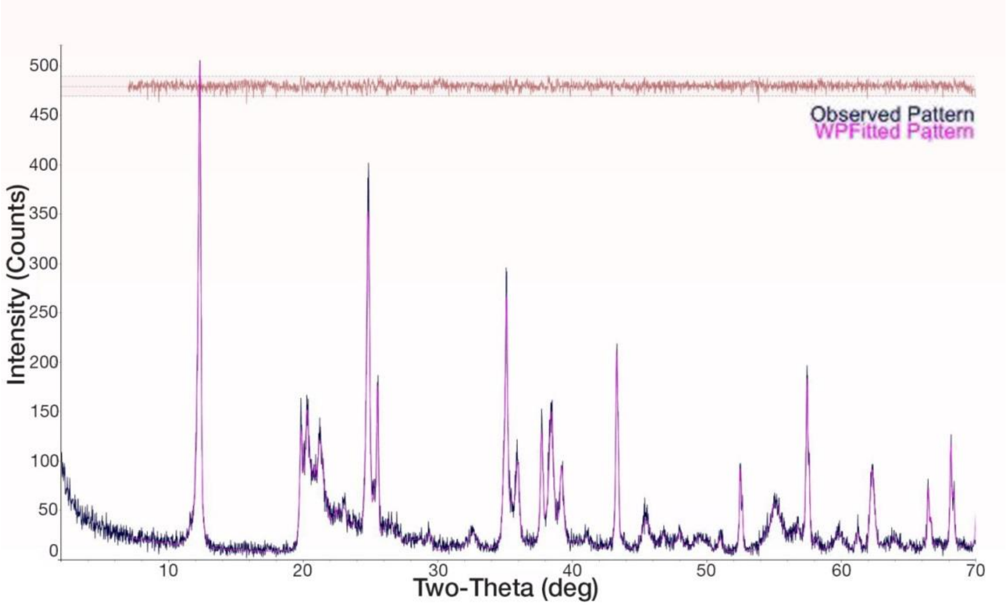

Figure 4.38: X-Ray Diffraction Pattern of 90-day Cured Stabilized Sample

As mentioned in the previous chapter, the Rietveld method is not able to capture non-crystalline or amorphous phases or those phases that are present in very low quantities, thus resulting in an overestimation of all the phases captured by the model. The internal standard that is added at a known concentration is used to determine the amorphous content as $\mathrm{A} = \frac{\mathrm{R_S} - \mathrm{W_S}}{\mathrm{R_S}(1 - \mathrm{W_S})} \times 100\%$, where R_s is the amount of the internal standard calculated by the Rietveld method and W_s is the weighed amount that was added to the sample. All phases are then normalized using the amorphous content to obtain their true weight percentages. Table 4.3 shows the percentage by weight of each mineral as calculated by the model and after adjustment through amorphous content calculation for one raw sample and one 7-day cured sample.

Table 4.3: Minerals Percentages as Calculated by Jade and after Adjustment

Minerals (%)	Raw Sample	Raw Adjusted	7-day Sample	7-day Adjusted
Kaolinite	79.7	78.2	75.5	62.5
Corundum	20.3	20.0	23.2	20.0
Calcite	-	-	1.0	0.8
Portlandite	-	-	0.3	0.2
Amorphous	-	1.8	-	17.2

For each XRD sample, the model is run several times, then a minimum of three runs per sample are randomly selected and averaged, thus resulting in a minimum of eighteen runs for each curing time. The amount of kaolinite, percent by weight, is then calculated and plotted with curing time as shown in Figure 4.39. The amount of kaolinite appears to sharply decrease after short times of stabilization and slow down with longer curing times. This behavior is best captured by fitting a logarithmic trendline with an R^2 value of 0.76. The fit does not seem great mainly due to the data points of the 90-day cured samples falling higher than the trendline. It is important to note that in this study, the whole-pattern fitting by Jade was directly applied to the diffractograms using the structural models for kaolinite already preloaded in the software with no further adjustments or measures taken. In a similar study, Chrysochoou (2014) was able to obtain R^2 values higher than 0.95 when fitting a logarithmic trendline for the amount of kaolinite using the Rietveld method only after experimentally measuring the reflections and the Reflection Intensity Ratios (RIR) then producing an XRD Powder Diffraction File (PDF) for the kaolinite used in that study. In addition, the results from the 0-day cured samples were removed from the fitted curve due to the large errors associated with the determination of the amorphous content when present in small amounts. Despite using preloaded structural models for kaolinite, the whole-pattern fitting applied by Jade is still considered a powerful and accurate tool to quantify the mineralogical makeup even for highly variable minerals such as kaolinite.

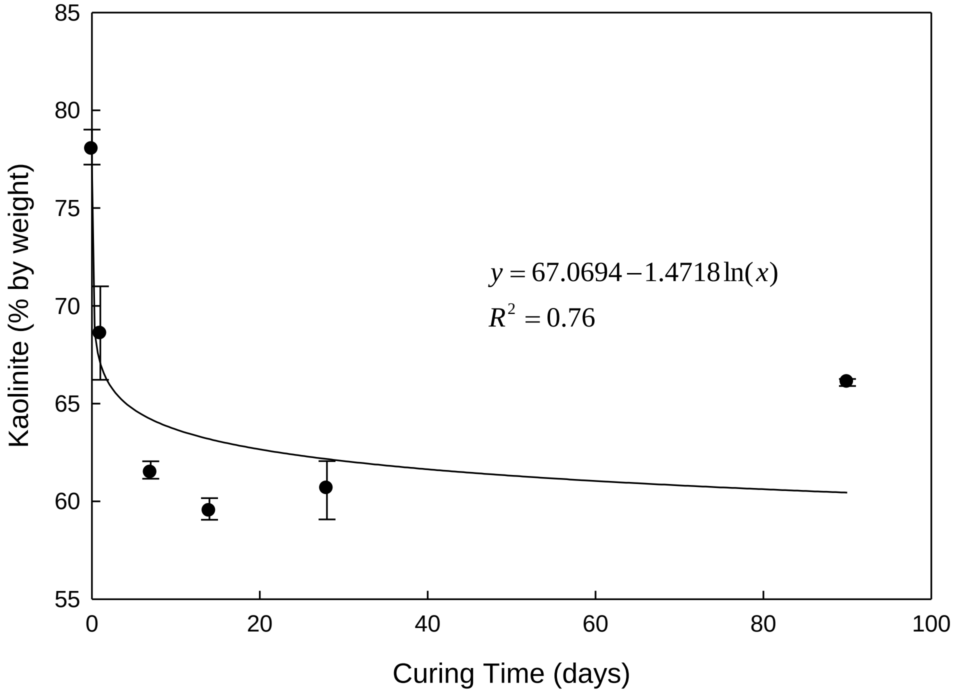

Figure 4.39: Amount of Kaolinite as Calculated by Jade with Curing Time

Another method for quantitative analysis was implemented in general accordance with the Reference Intensity Ratio (RIR) method. This method consists of calculating the ratio of the integrated intensity of the major kaolinite peak at 12.35^o two-theta (7.16 Å) to that of corundum at 43.36^o two-theta (2.085 Å) and use this ratio to monitor the evolution of kaolinite dissolution due to stabilization with curing time. These two peaks were specifically chosen because they are one of the major peaks of each respective mineral and they basically do not overlap with peaks from other minerals. A total of six different XRD tests were analyzed for each curing time (a total of 36 tests) and the average ratio of integrated intensity of kaolinite to corundum along with range bars indicating the minimum and maximum values are shown in Figure 4.40. As can be seen, the ratio of kaolinite to corundum has a logarithmic relationship with time and the fit of the curve is excellent with an R^2 value of 0.93.

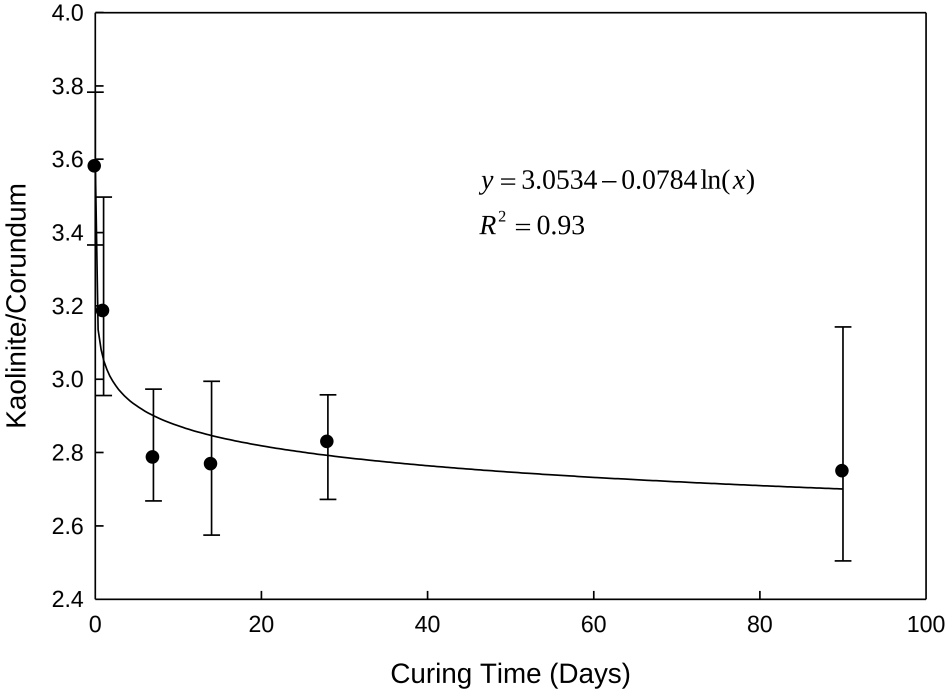

Figure 4.40: Change of Kaolinite to Corundum Ratio with Curing Time

Since the evolution of the unconfined compressive strength shares a similar trend with the evolution of the kaolinite to corundum ratio with time, both being logarithmic, it becomes only logical to check for any linear relationship between the two. At each curing time, the average and range bars of three unconfined compression tests and six XRD tests are depicted in Figure 4.41. The relationship between the unconfined compressive strength and the kaolinite to corundum ratio is linear with an R^2 of 0.86. This observation can be explained by the fact that as kaolinite is being attacked in a high pH environment, the released elements, mainly silica and alumina, are reacting with the calcium present in the pore solution to form the cementitious compounds directly responsible for the strength gain. In other words, the rate at which the kaolinite is dissolving is similar to the rate of strength gain and thus the relation between the cause and consequence is highly linear.

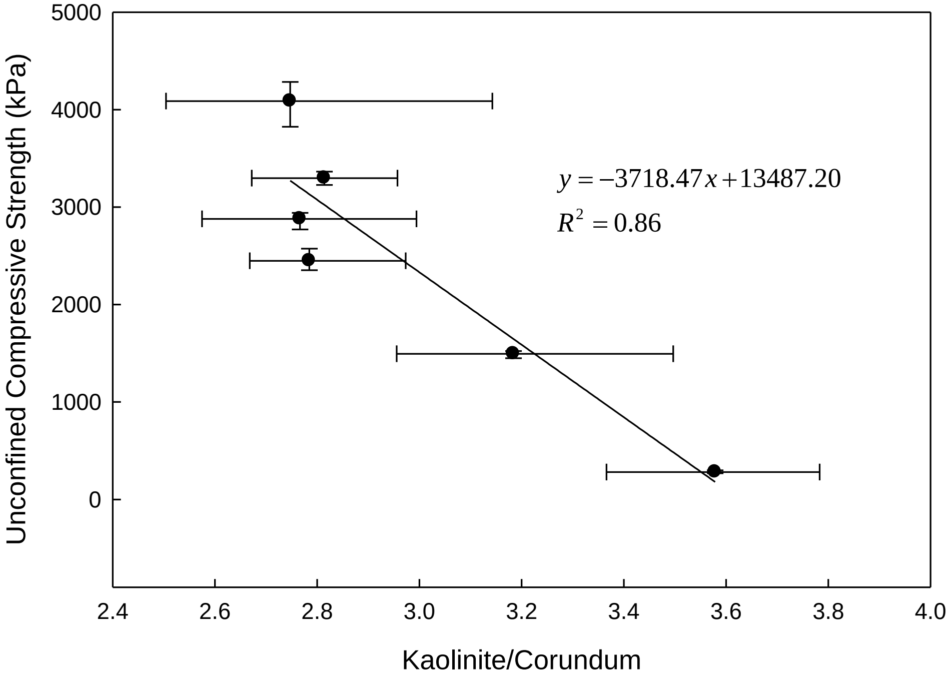

Figure 4.41: Correlation between UCS and Kaolinite to Corundum Ratio

In addition, since CSH is the major hydration product responsible for the strength gain in cement stabilized soil, the relationship between the amount of CSH that is forming, as estimated indirectly by the mass loss in the TG test between 105 and 440 ^{o}C, is linearly correlated to the amount of the dissolving kaolinite (kaolinite to corundum ratio) as shown in Figure 4.42. The fit of the linear trendline is excellent with an R^2 value of 0.96.

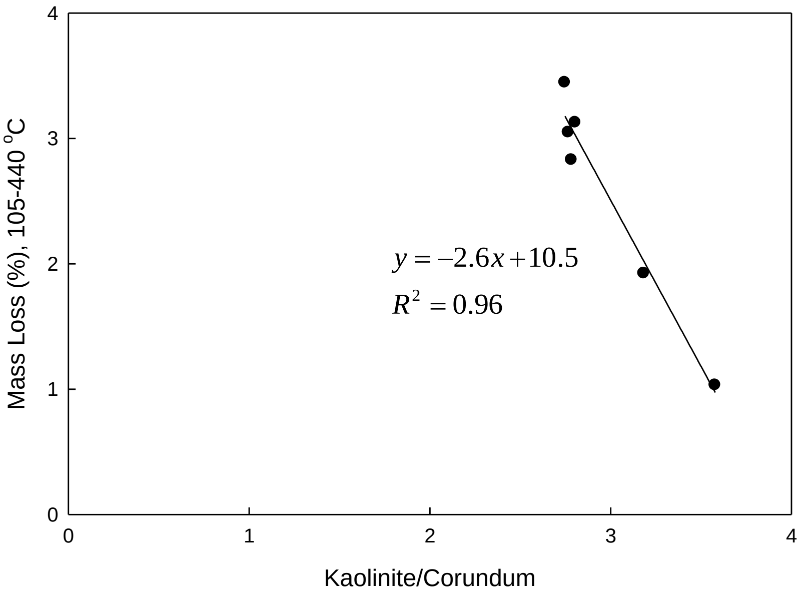

Figure 4.42: Correlation between Amount of CSH and Kaolinite to Corundum Ratio

4.4 Microstructure

4.4.1 SEM and EDS

SEM is a common and powerful technique used for the observation and characterization of the microstructure of soils. After each unconfined compression test, small cubic samples were recovered from the center of each sample, freeze-dried, mounted on aluminum stubs, and coated with iridium before running SEM tests. The Zeiss NEON 40 EsB FE-SEM was used in this study in secondary electron detection mode to obtain high resolution images of surface topography and morphology. Two detectors, SE and InLens, were used at different magnifications. The SE detector provides a better angle to visualize the topography at low magnifications while the InLens detector is suitable for high magnifications because it gives better resolution. This SEM is equipped with INCA Energy 250 Energy Dispersive X-ray Microanalysis system with Analytical Drift Detector used for chemical composition analysis. Despite the fact that quantitative measurements and weight percentages of elements are obtained from EDS spectra, they should be used carefully and only as general guidelines to what is present in the sample because they are not collected from smooth surfaces but rather from fractured rough surfaces. The software used for EDS quantification is AZtec by OXFORD Instruments. Micrographs obtained for the horizontal and vertical planes at various magnifications are used to characterize the general fabric and the arrangement of clay particles, observe the cementitious products, and monitor the evolution of the microstructure due to stabilization.

Nearly 2000 micrographs were collected during this study but only a few are presented herein. The comments made in this section are based on evidence from all the gathered data. Representative micrographs at different magnifications taken for horizontal and vertical planes of the raw kaolinite are presented in Figure 4.43 and Figure 4.44, respectively.

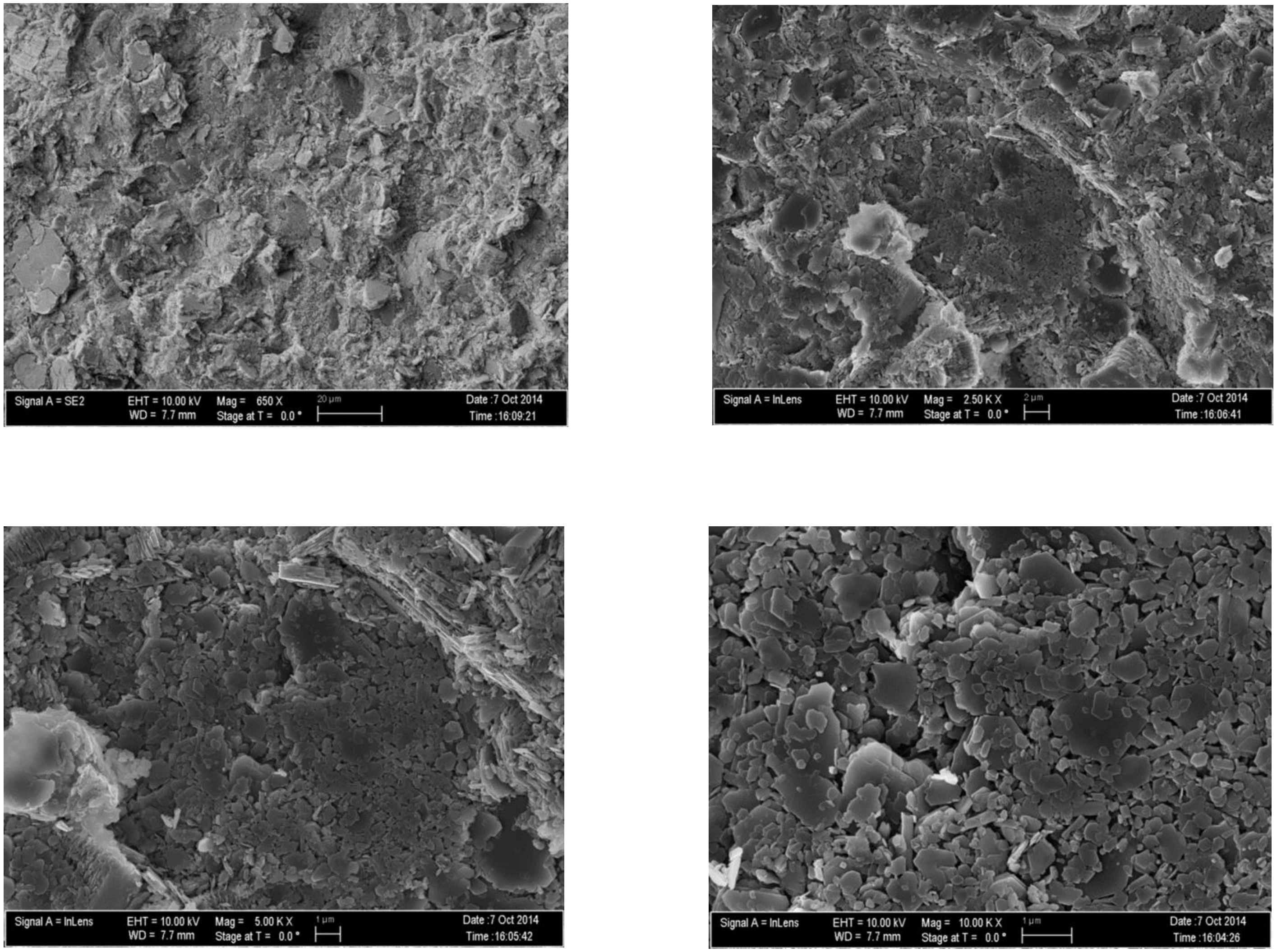

Figure 4.43: SEM Micrographs of Horizontal Planes of Raw Kaolinite at Different Magnifications

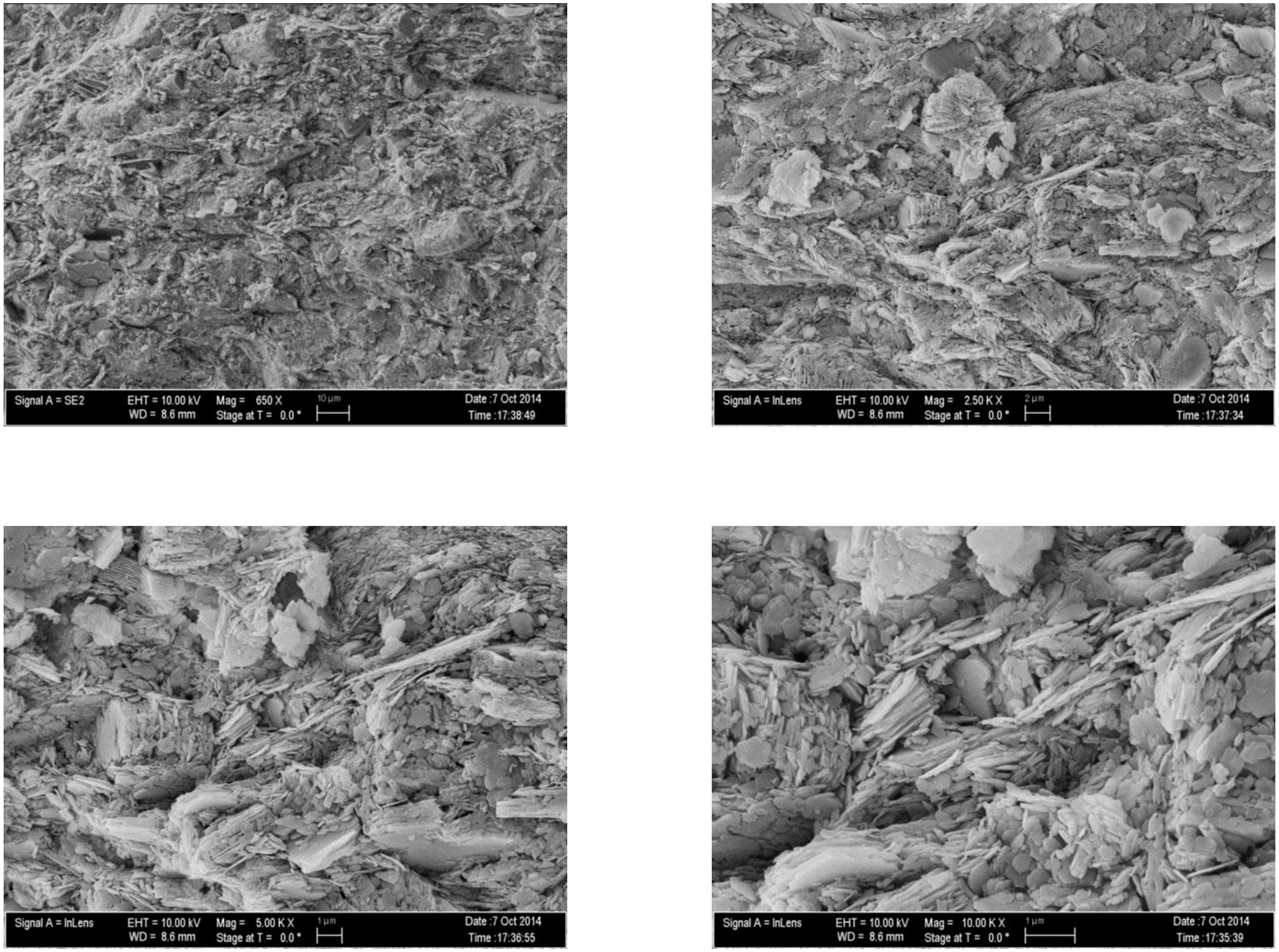

Figure 4.44: SEM Micrographs of Vertical Planes of Raw Kaolinite at Different Magnifications

Book-like morphology is seen in the kaolinite samples. Groups of vermicular crystals of stacked clay platelets are sporadically spotted throughout the samples which is not unusual in certain kaolinites. Clay particles lying flat on and next to each other are easily seen in the horizontal plane. Despite looking nicely packed from this angle, they seem loose and disconnected from each other. The vertical plane contrasts well with the horizontal plane. It looks less organized and the edges of the clay particles are mostly exposed. Raw kaolinite samples were compacted at the optimum moisture content (OMC) and maximum dry density. At OMC, the diffuse double layer is well-developed and tends to promote dispersion due to the dominance of repulsive forces between neighboring particles resulting in a more orderly arrangement of particles characterized by face to face contacts. As seen in the micrographs of the vertical plane, the platy kaolinite particles show a high degree of preferred orientation; they lay parallel to each other and normal to the direction of compaction. The actual moisture content at the end of the unconfined compression test was about 0.5 % lower than OMC. This may have led to a slight decrease in preferred orientation of the clay particles which is expected at moisture contents dry of optimum.

EDS was performed at low magnification (300 X) to reveal the general elemental makeup of the sample. EDS spectrum of raw kaolinite is presented in Figure 4.45.

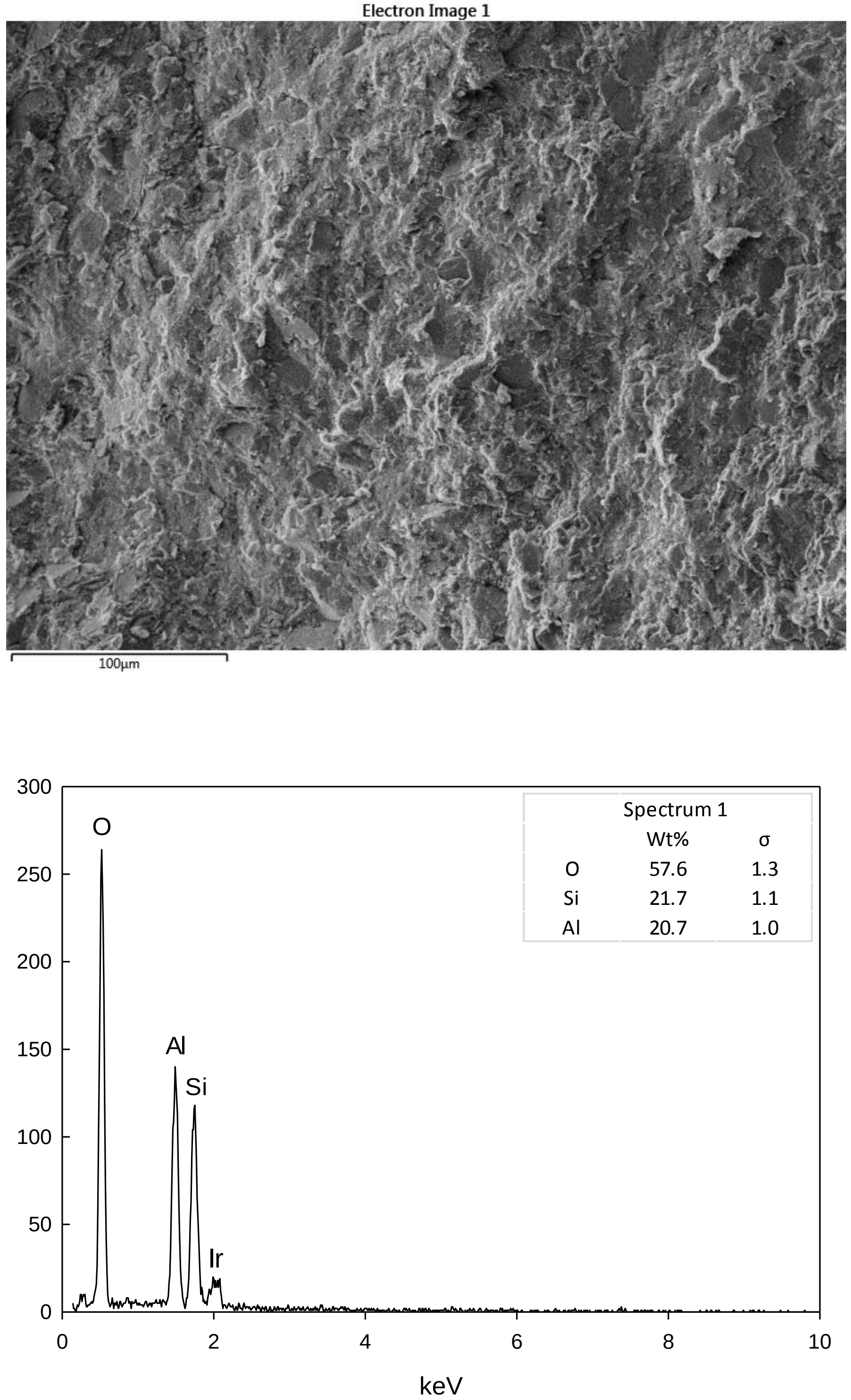

Spectrum 1	Wt%	σ
O	57.6	1.3
Si	21.7	1.1
Al	20.7	1.0

Figure 4.45: Micrograph of Raw Kaolinite (top) and EDS Spectrum (bottom)

Oxygen, silicon, aluminum, and iridium are detected by the EDS. Beside iridium which is present due to the coating, the remaining elements are the constituents of kaolinite, $Al_2Si_2O_5(OH)_4$., with the exception of hydrogen which cannot be detected by EDS. The theoretical weight percentages of oxygen, silicon, and aluminum in pure kaolinite are 55.8, 21.8, and 20.9 %, respectively. After excluding the iridium, the quantitative analysis by EDS from several spectra yields the average weight percentages of oxygen, silicon, and aluminum as 55.4, 23.7, and 20.9 %, respectively, which are similar to the theoretical values. The close agreement is primarily due to the averaging effect resulted from scanning a large surface and interaction volume. In other words, the EDS loses its accuracy when scanning a small and thin feature because characteristic x-rays will penetrate the small feature and will be affected by the surrounding volume.

The program CASINO (monte CArlo SImulation of electroN trajectory in sOlids) was used to simulate the trajectory of the electrons originating from the incident beam and penetrating the kaolinite sample in order to estimate the interaction volume that contributes to the EDS spectra. The interaction volume in terms of energy dissipation contour lines of the electron beam with 5 and 10 kV energy is illustrated in Figure 4.46. The $\phi(\rho z)$ curves give information about the X-ray generation depth of each of the major chemical elements in the sample and are illustrated in Figure 4.47 and Figure 4.48 for the electron beam energies of 5 and 10 kV, respectively. These curves also show the comparison between the intensity of the emitted X-rays (absorbed intensity) and the generated intensity. Representative micrographs at different magnifications taken for horizontal and vertical planes of the 1-day cured stabilized kaolinite are presented in Figure 4.49 and Figure 4.50, respectively.

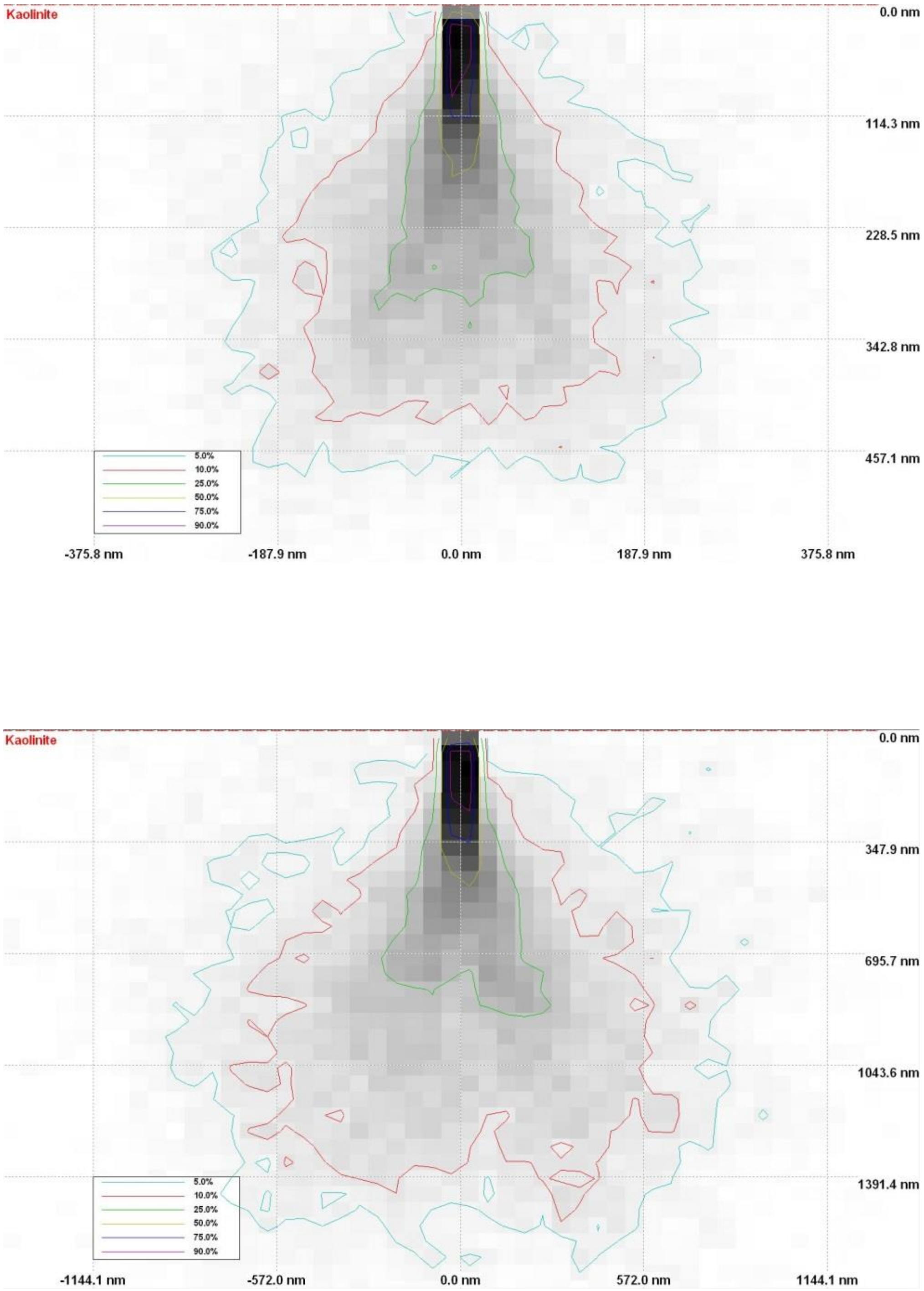

Figure 4.46: Energy Dissipation of 5 kV (top) and 10 kV (bottom) Electron Beam

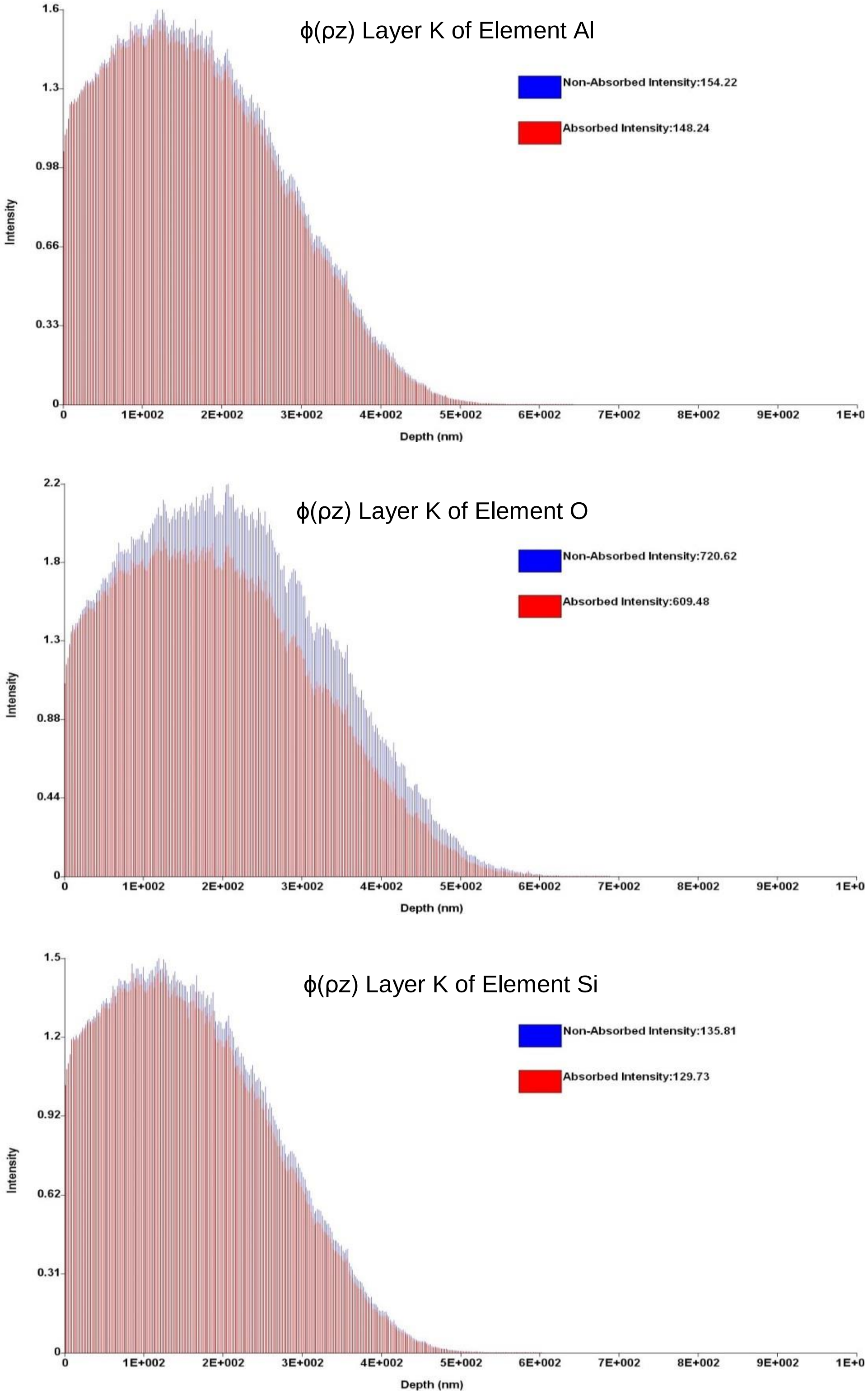

Figure 4.47: ϕ(ρz) Curves of Major Chemical Elements in Kaolinite for Electron Beam Energy of 5 kV

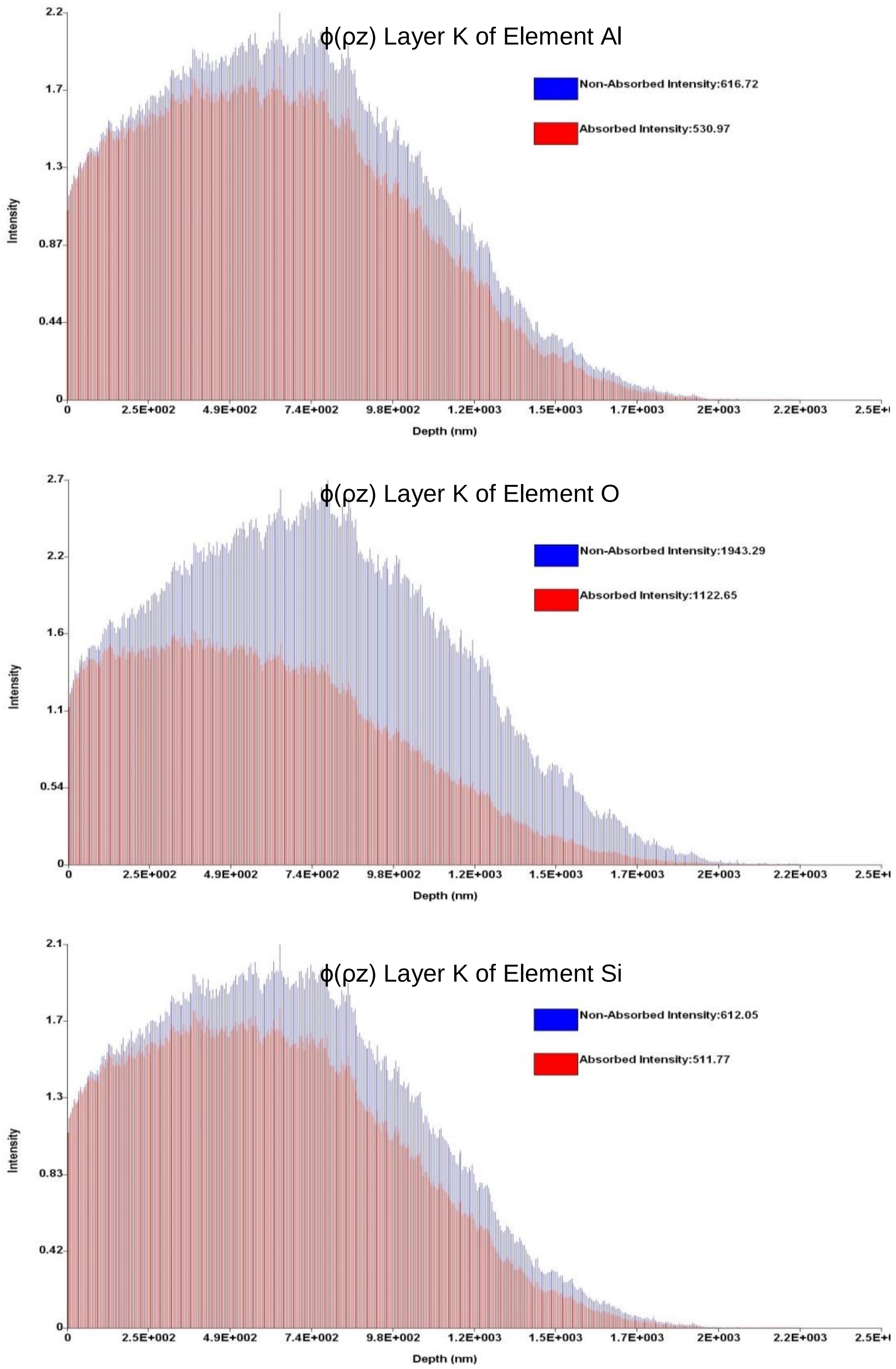

Figure 4.48: ϕ(ρz) Curves of Major Chemical Elements in Kaolinite for Electron Beam Energy of 10 kV

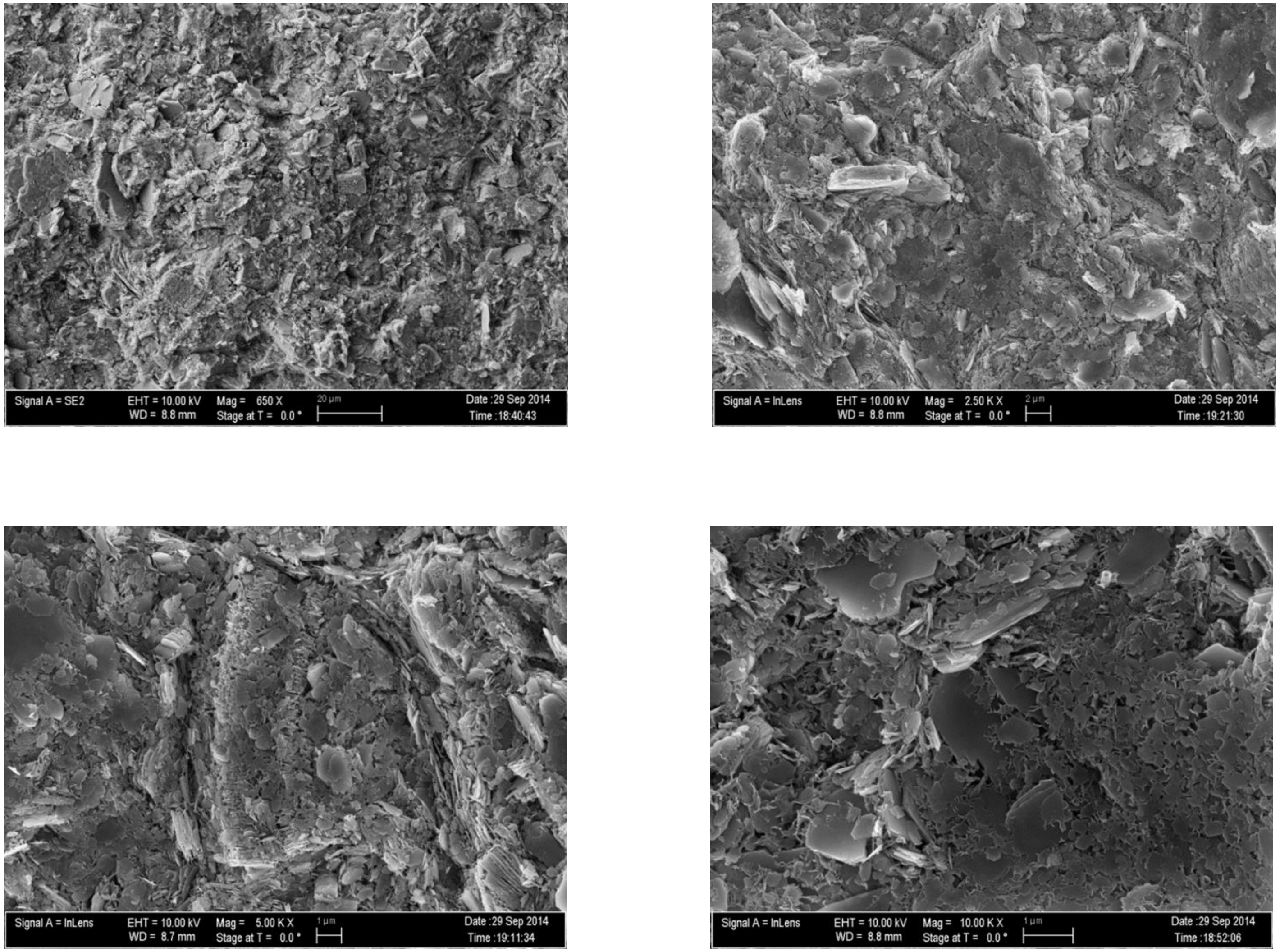

Figure 4.49: SEM Micrographs of Horizontal Planes of 1-day Cured Samples at Different Magnifications

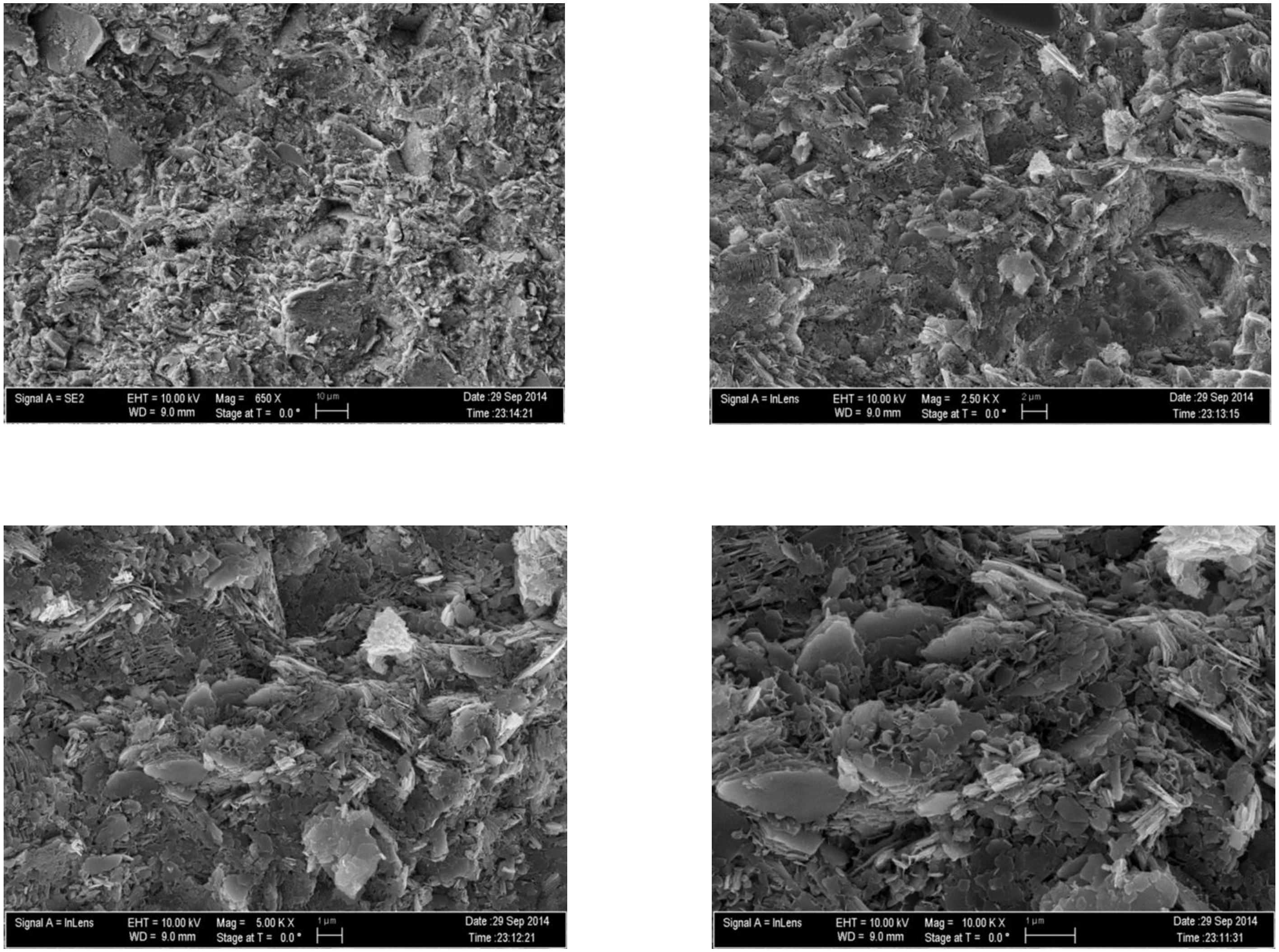

Figure 4.50: SEM Micrographs of Vertical Planes of 1-day Cured Samples at Different Magnifications

In comparison with the raw soil, differences between the horizontal and vertical planes are less obvious in the stabilized soil. The preferred particle orientation is less pronounced resulting in similarities between the two planes. After the addition of cement and water to the soil, calcium is released in the pore solution at a high concentration. The divalent calcium cation has a greater replacement power than monovalent ions such as sodium and potassium, and thus fewer divalent cations are needed to balance the net negative charge of the clay particles. The thickness of the diffuse double layer is then reduced and attractive forces become dominant resulting in a flocculated structure characterized by edge to face contacts between clay particles. Here it should be noted that after mixing the cement and water with the soil, the forces induced by compaction may still cause some preferential alignments in clay particles. Slender fibers of CSH are easily detected in all the specimens as shown in both planes (Figure 4.49 and Figure 4.50). They appear to protrude from the edges of the clay particles and connect them together. The kaolinite particles in the 1-day cured samples do not seem to show any noticeable difference in size compared to those in the raw samples. Although the CSH fibers were generally present throughout the samples, few areas were encountered in the 1-day cured samples where a lack of fibers was noticeable as shown in Figure 4.51. This may be due to either the retardation in the formation of hydration products or the absence of stabilizer in these areas despite every effort for obtaining a homogeneous mix.

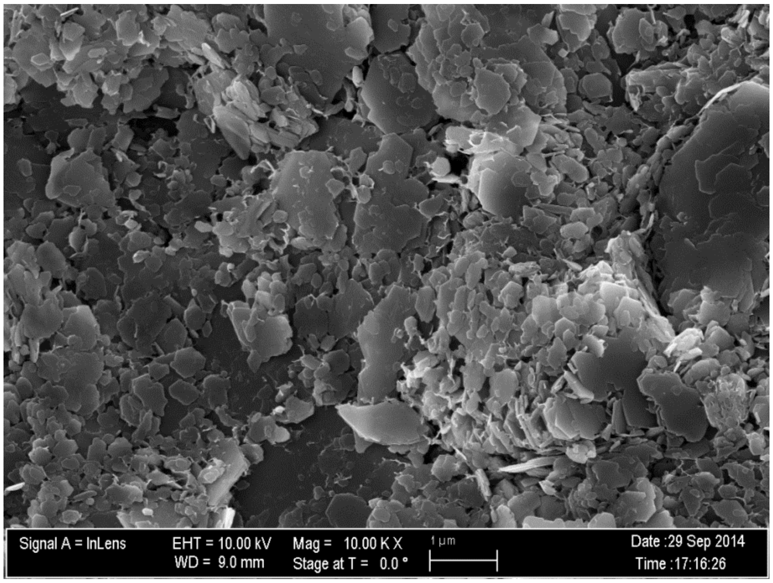

Figure 4.51: SEM Micrograph Showing Lack of CSH Fibers in 1-day Cured Samples

A cement particle, most likely alite (C_3S), that is in the process of hydrating can be seen in Figure 4.52 with its corresponding EDS spectrum. It shows hydration products being formed on the surface and branching out from the grain. A few of these instances were encountered in the 1-day cured samples reflecting the effect of the short curing time. The EDS spectrum shows primarily oxygen and calcium, followed by silicon, in approximately the expected proportions of alite, and trace amounts of aluminum and magnesium likely originating from surrounding hydration products and clay particles.

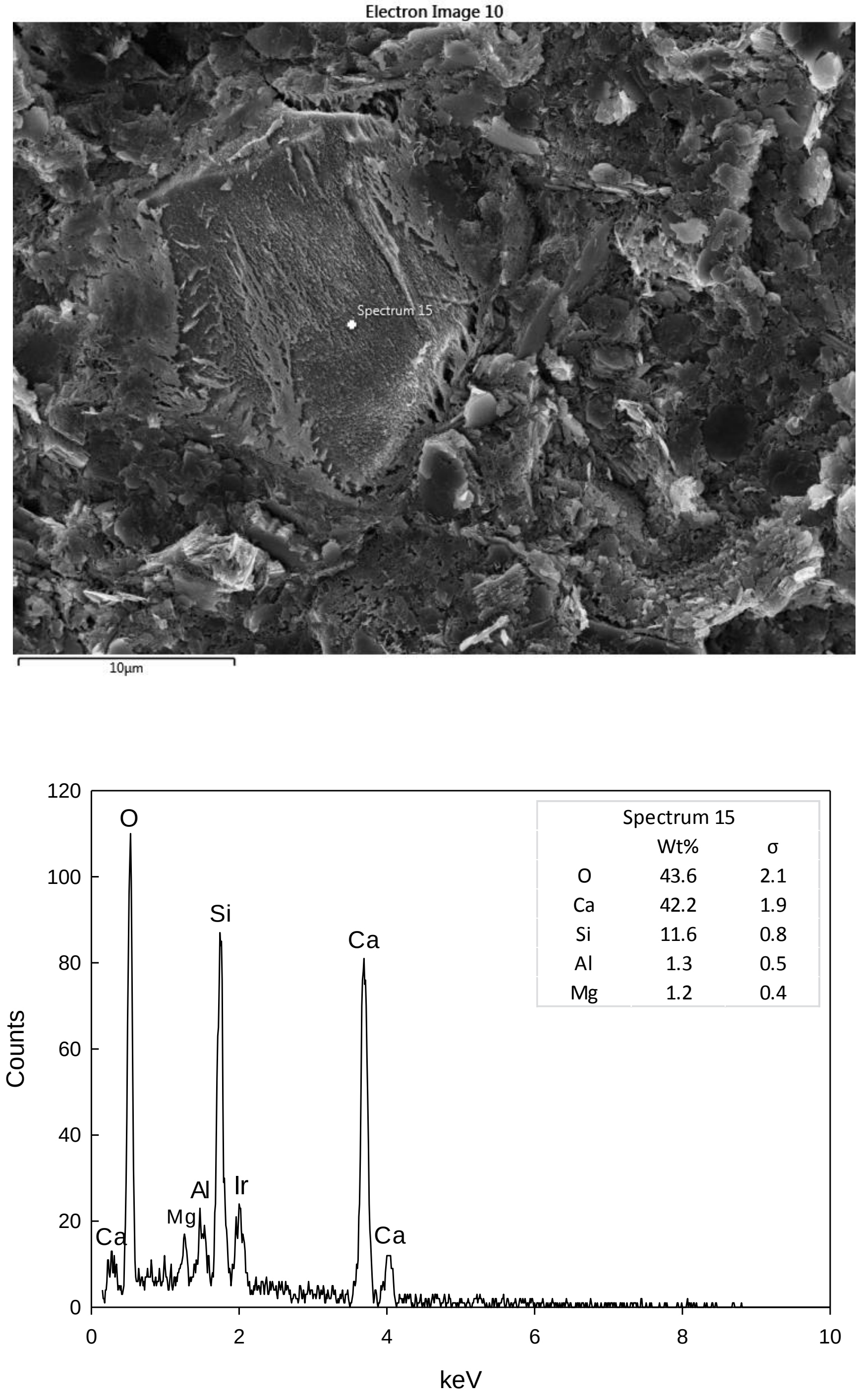

Figure 4.52: SEM Micrograph Showing Hydration of Cement Particle in 1-day Cured Sample (top) and Corresponding EDS Spectrum (bottom)

Other hydration products such as calcium hydroxide and ettringite are sometimes seen mainly in the crevices of the compacted soil as shown in Figure 4.53. Calcium hydroxide exhibits the typical platy crystal habit, whereas ettringite is recognized by its acicular crystal habit that consists of radiating thin needle-like crystals with a high aspect ratio. The presence of these characteristic crystal shapes is controlled by the availability of voids for unrestrained crystal growth. Ettringite is the most common member of the AFt (alumina, ferric oxide, tri-sulfate) phases which are a group of calcium sulfoaluminate hydrates. Gypsum is intentionally added to the cement to prevent flash setting by retarding the hydration of C_3A through the formation of ettringite on its surface. Once the gypsum is depleted and insufficient sulfate ions are present in the solution, ettringite becomes unstable and converts to monosulfate (AFm). The identification of calcium hydroxide and ettringite is confirmed through the EDS spectrum which reveals the presence of oxygen, calcium, aluminum, sulfur, and silicon.

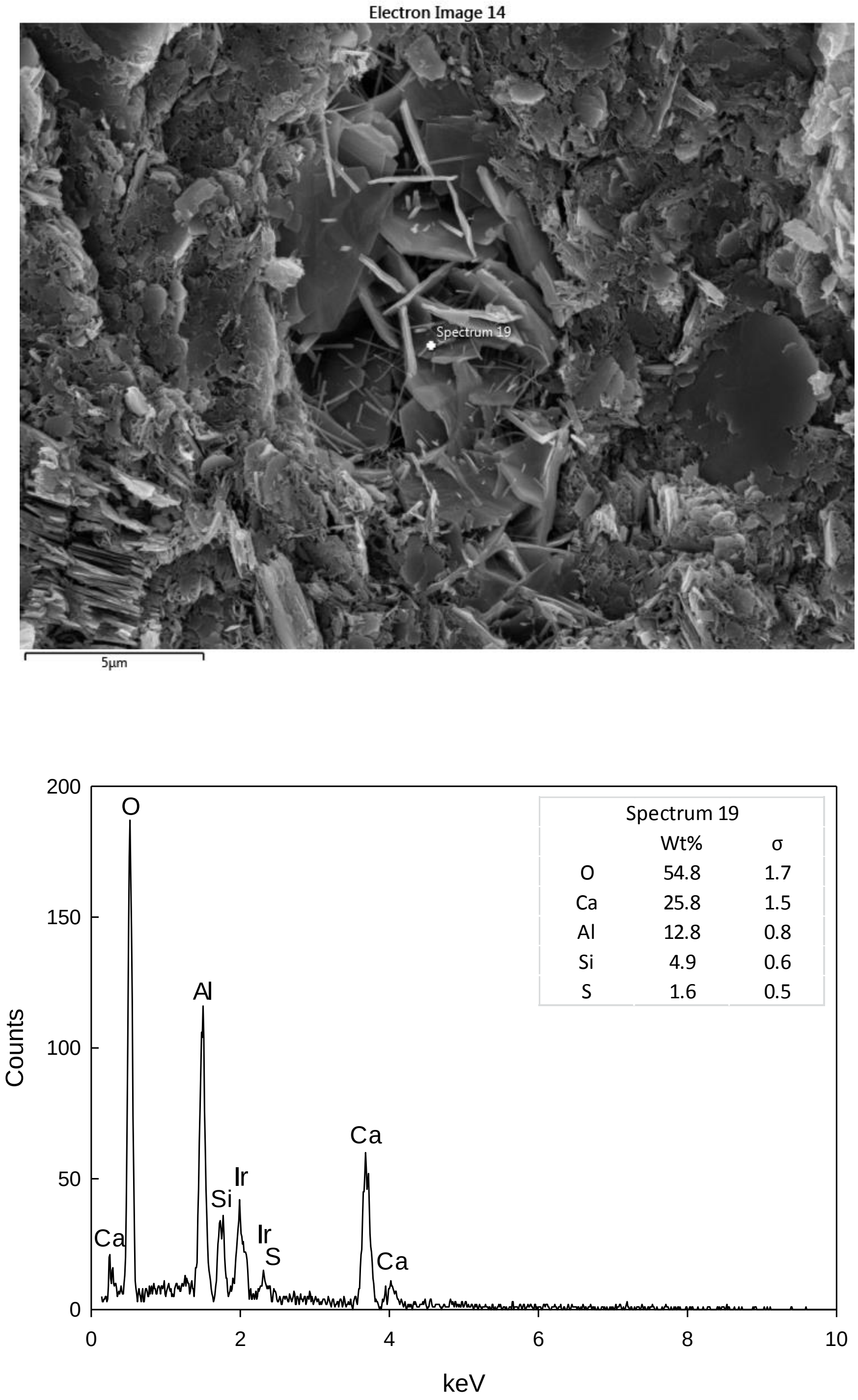

Spectrum 19

	Wt%	σ
O	54.8	1.7
Ca	25.8	1.5
Al	12.8	0.8
Si	4.9	0.6
S	1.6	0.5

Figure 4.53: Micrograph of Platy Calcium Hydroxide and Needle-like Ettringite Crystals in 1-day Cured Samples (top) and Corresponding EDS Spectrum (bottom)

An example of an EDS spectrum performed at low magnifications (300 X) to reveal the overall chemical composition of the 1-day cured samples is illustrated in Figure 4.54.

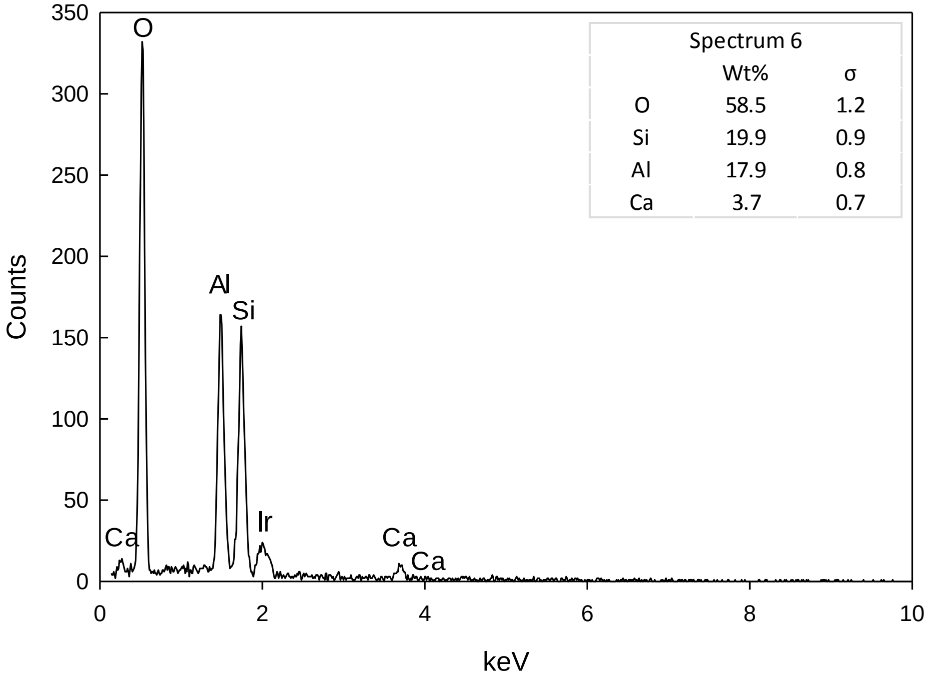

Spectrum 6

	Wt%	σ
O	58.5	1.2
Si	19.9	0.9
Al	17.9	0.8
Ca	3.7	0.7

Figure 4.54: EDS Spectrum of 1-day Cured Sample at 300 X

Micrographs of the horizontal and vertical planes for the 7-day cured stabilized kaolinite are shown in Figure 4.55and Figure 4.56, respectively.

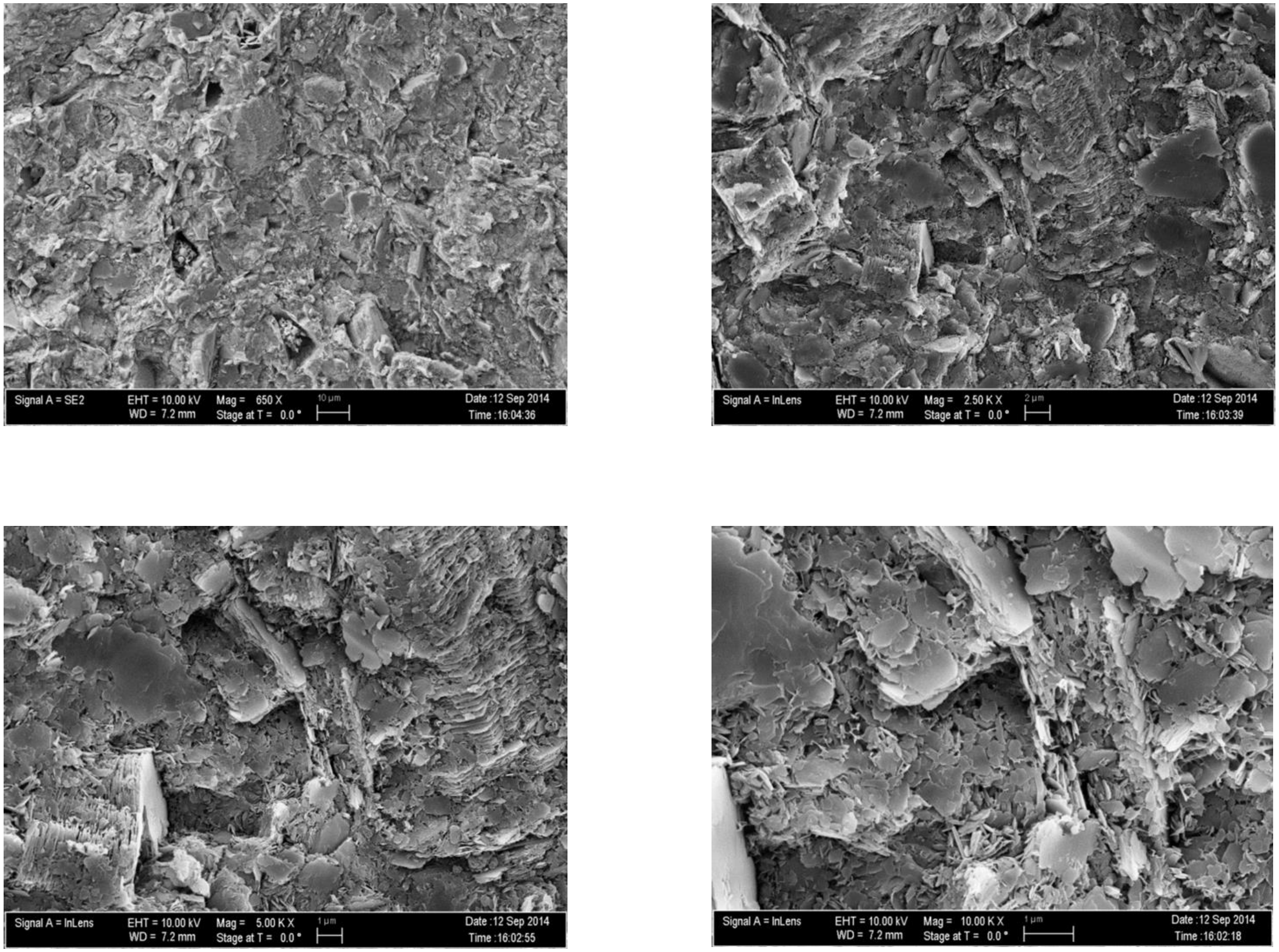

Figure 4.55: SEM Micrographs of Horizontal Planes of 7-day Cured Samples at Different Magnifications

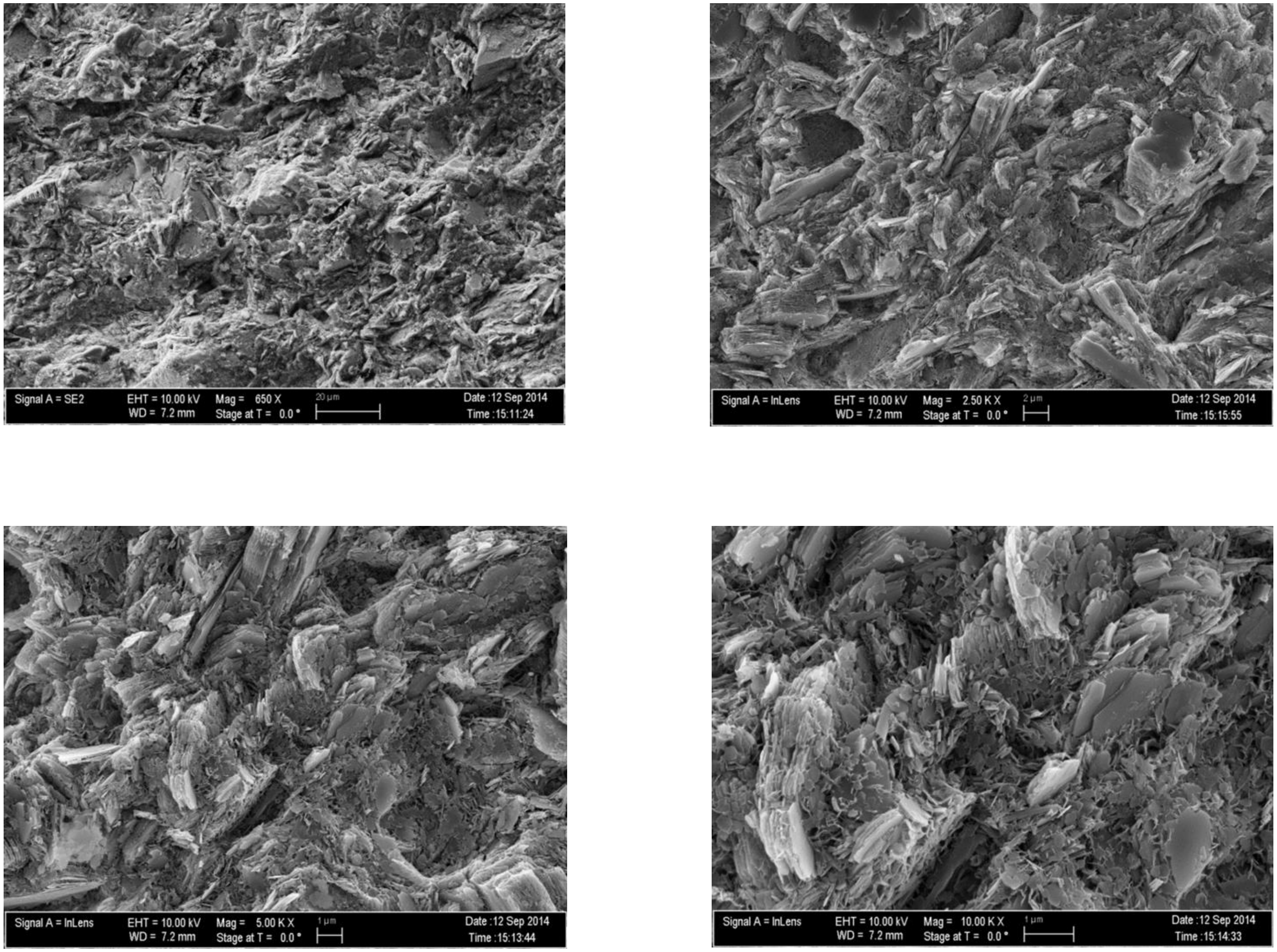

Figure 4.56: SEM Micrographs of Vertical Planes of 7-day Cured Samples at Different Magnifications

Similar to the 1-day cured samples, the soil generally exhibits a flocculated structure in which preferred particle orientation is not obvious and the differences between the two planes is insignificant. In the 7-day cured samples, CSH fibers are spread rather continuously, binding the clay particles together. Few areas are encountered where the lack of fibers is visible. The other hydration products, which form as isolated crystals, are more common than the 1-day cured samples and are detected more easily in the void spaces as illustrated in Figure 4.55 at 650 X. Denser CSH crystals are sometimes spotted as shown in Figure 4.57 along with its corresponding EDS spectrum. Brucite or $Mg(OH)_2$, which is another hydration product is shown in Figure 4.58. Calcium hydroxide and ettringite can be seen in Figure 4.59.

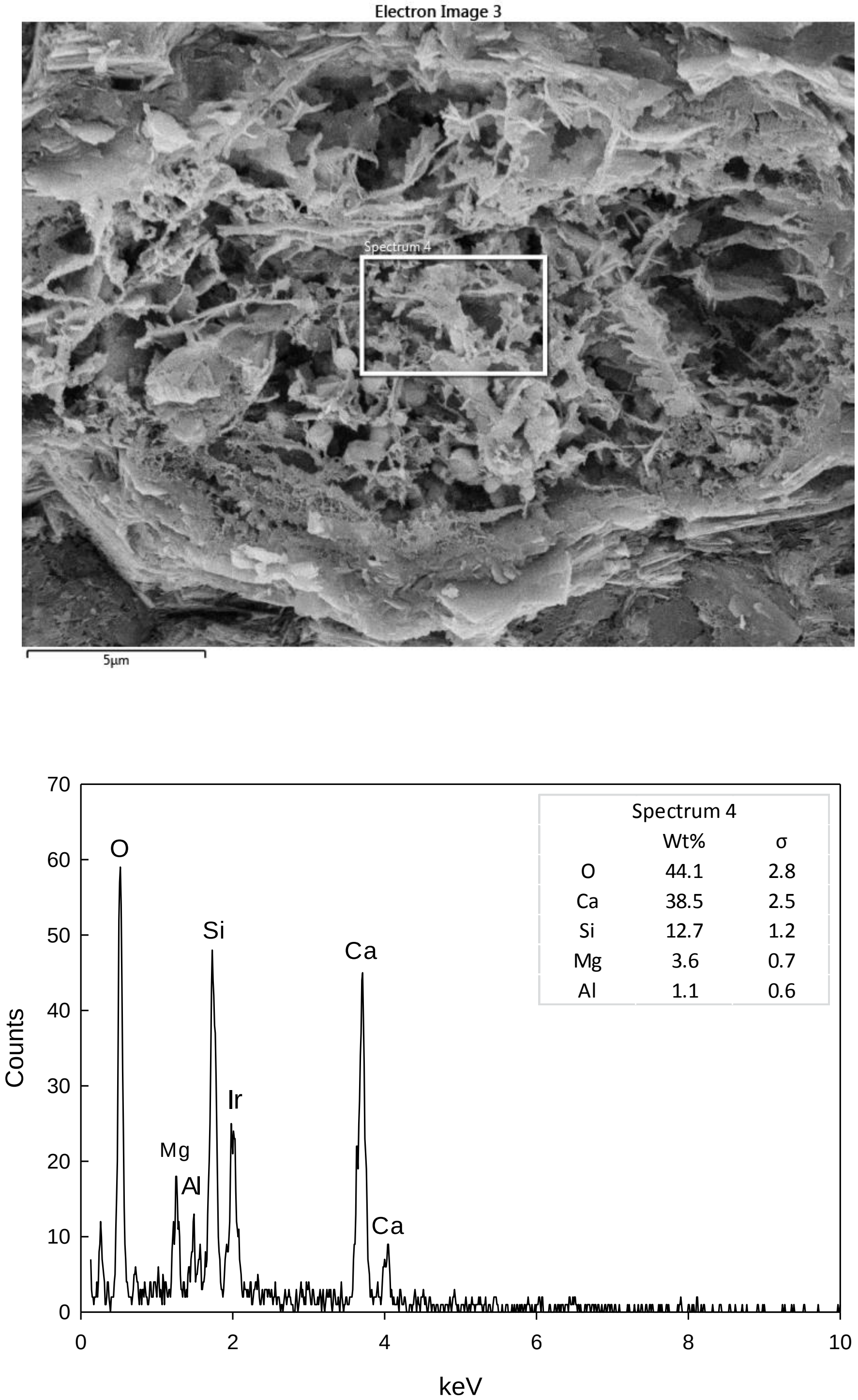

Spectrum 4		
	Wt%	σ
O	44.1	2.8
Ca	38.5	2.5
Si	12.7	1.2
Mg	3.6	0.7
Al	1.1	0.6

Figure 4.57: Micrograph of Dense CSH Crystals in 7-day Cured Samples (top) and Corresponding EDS Spectrum

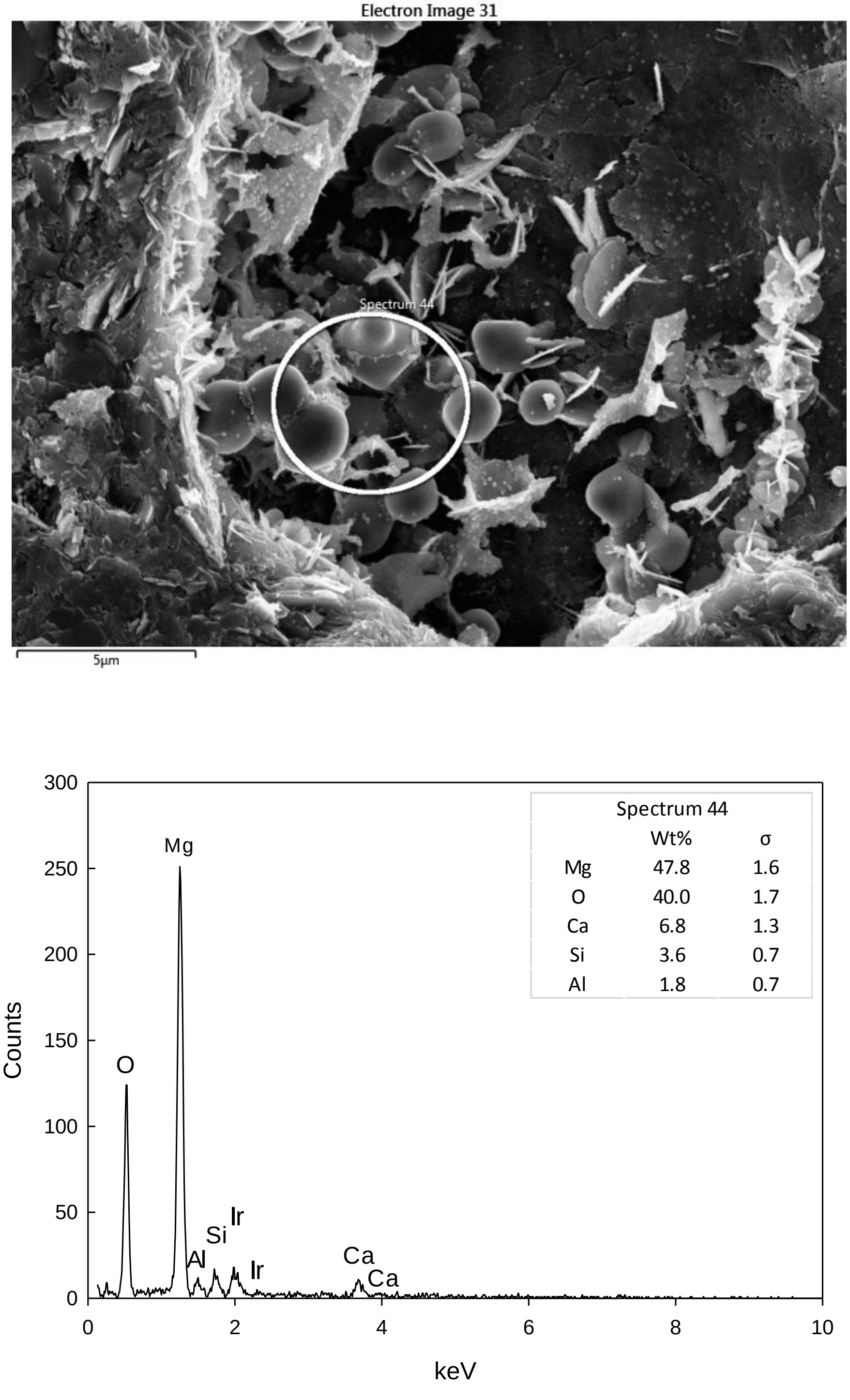

Spectrum 44		
	Wt%	σ
Mg	47.8	1.6
O	40.0	1.7
Ca	6.8	1.3
Si	3.6	0.7
Al	1.8	0.7

Figure 4.58: Micrograph of Brucite (top) and Corresponding EDS Spectrum

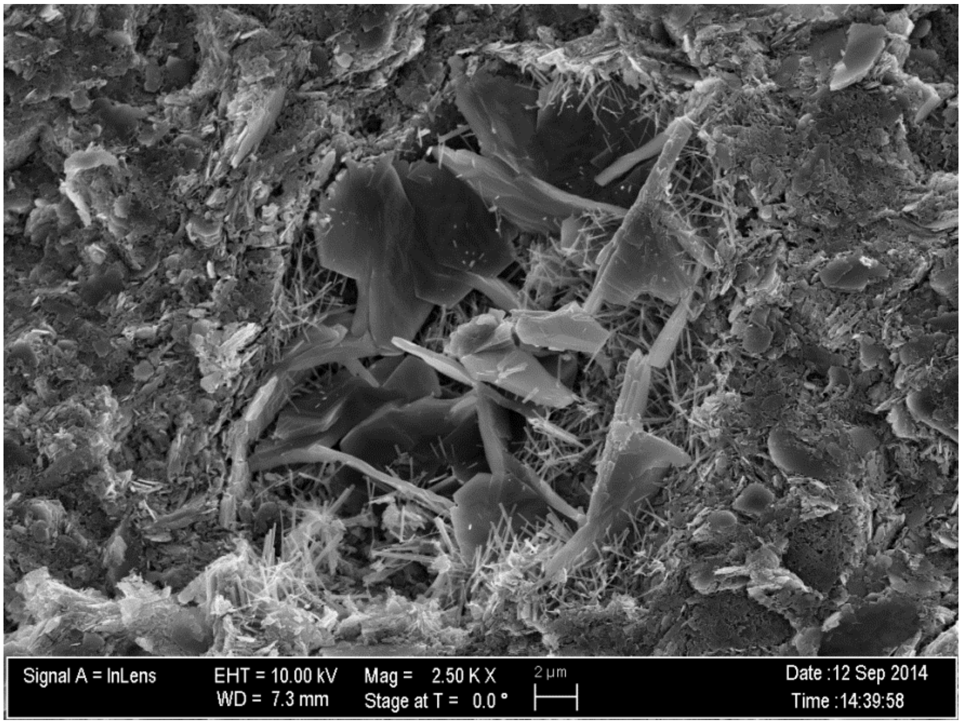

Figure 4.59: Micrograph of Calcium Hydroxide and Ettringite Crystals

Calcium hydroxide crystals appear to be larger and thicker in the 7-day cured sample than those seen in the 1-day cured sample (Figure 4.53) and the ettringite prismatic needles are denser. It is worth noting that ettringite was not commonly encountered in the 7-day cured samples. As previously mentioned, ettringite usually converts to monosulfate phases when the gypsum is depleted and insufficient ions are present in the solution. Monosulfate crystals are typically thin hexagonal plates or irregular rosettes and are more commonly found in the 7-day cured samples. Figure 4.60 shows monosulfate crystals with its corresponding EDS spectrum.

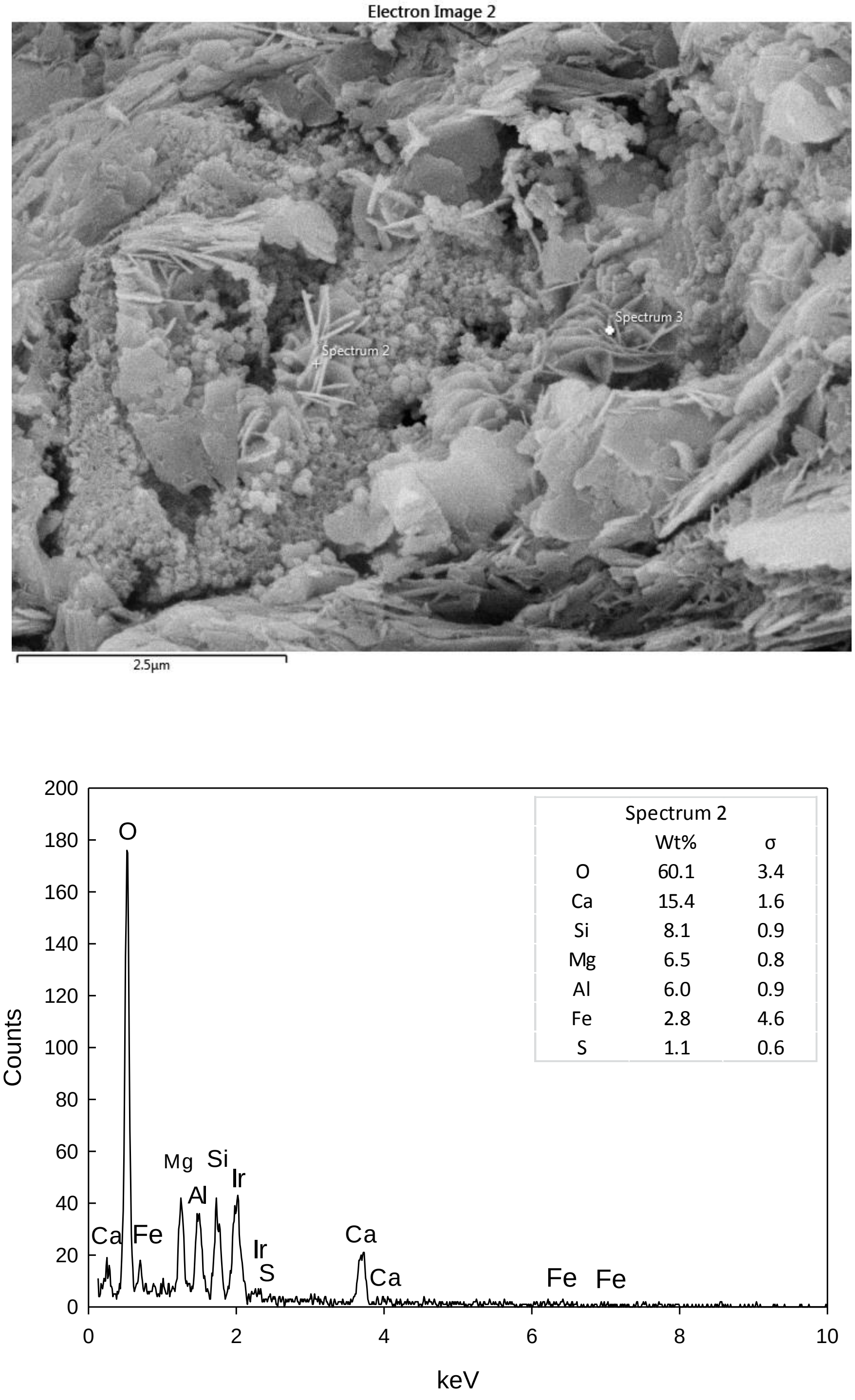

Figure 4.60: Micrograph of Monosulfate Crystals (top) and Corresponding EDS Spectrum (bottom)

A representative EDS spectrum performed at low magnifications (300 X) to reveal the overall chemical composition of a 7-day cured sample is illustrated in Figure 4.61. The average weight percentages of oxygen, silicon, aluminum, and calcium obtained from several EDS spectra are 55.4, 21.1, 18.6, and 4.9 %, respectively.

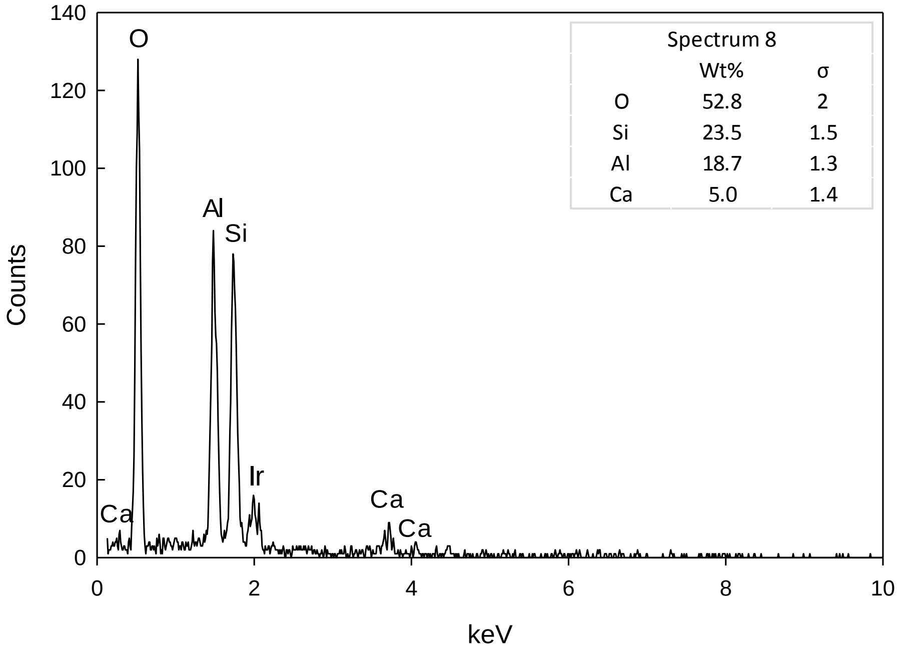

Figure 4.61: EDS Spectrum of 7-day Cured Sample at 300 X

SEM micrographs of the 14-day cured stabilized kaolinite samples are presented in Figure 4.62and Figure 4.63, micrographs of the 28-day cured samples are presented in Figure 4.64 and Figure 4.65, and those of the 90-day cured samples are presented in Figure 4.66 and Figure 4.67.

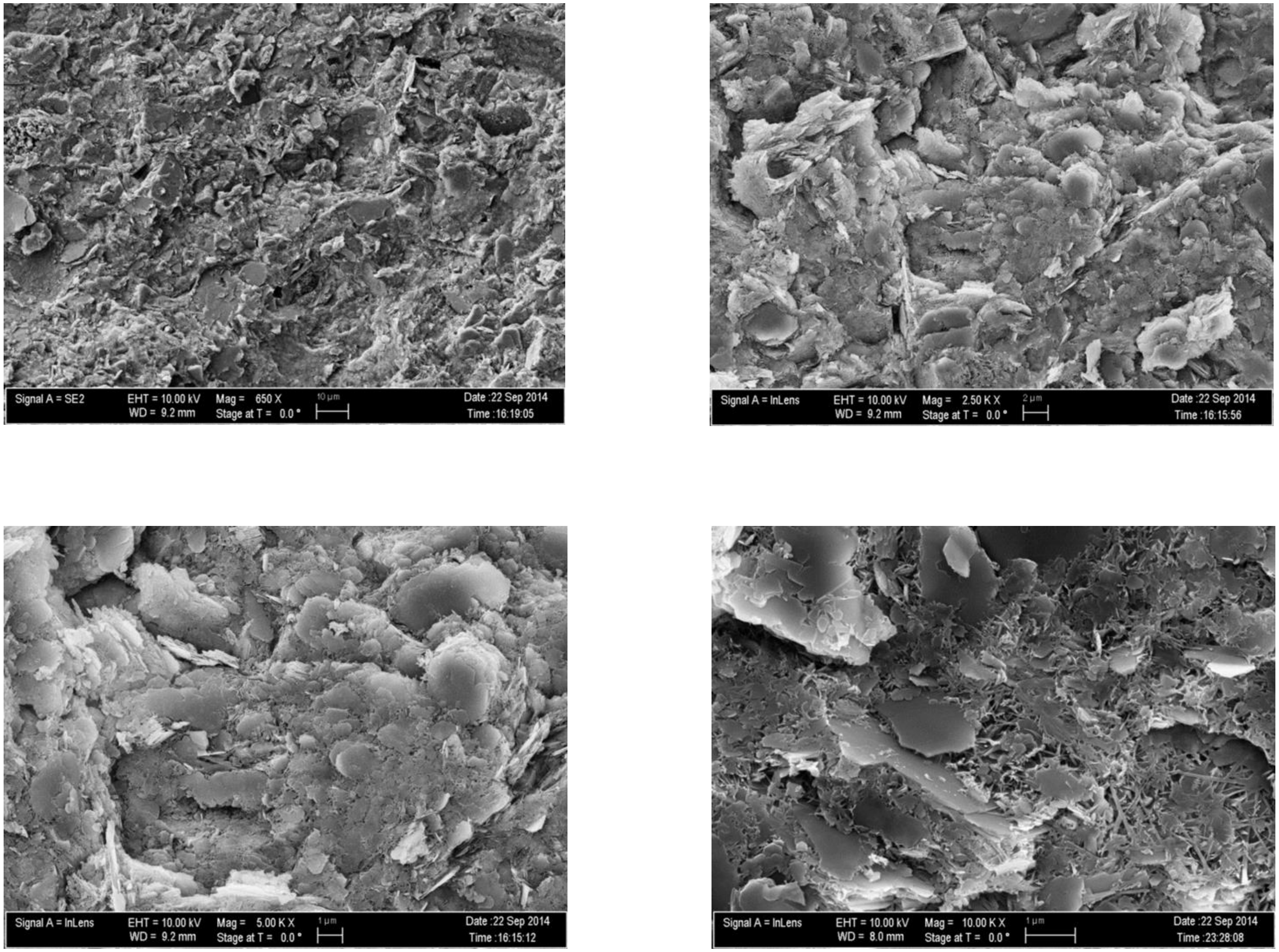

Figure 4.62: SEM Micrographs of Horizontal Planes of 14-day Cured Samples at Different Magnifications

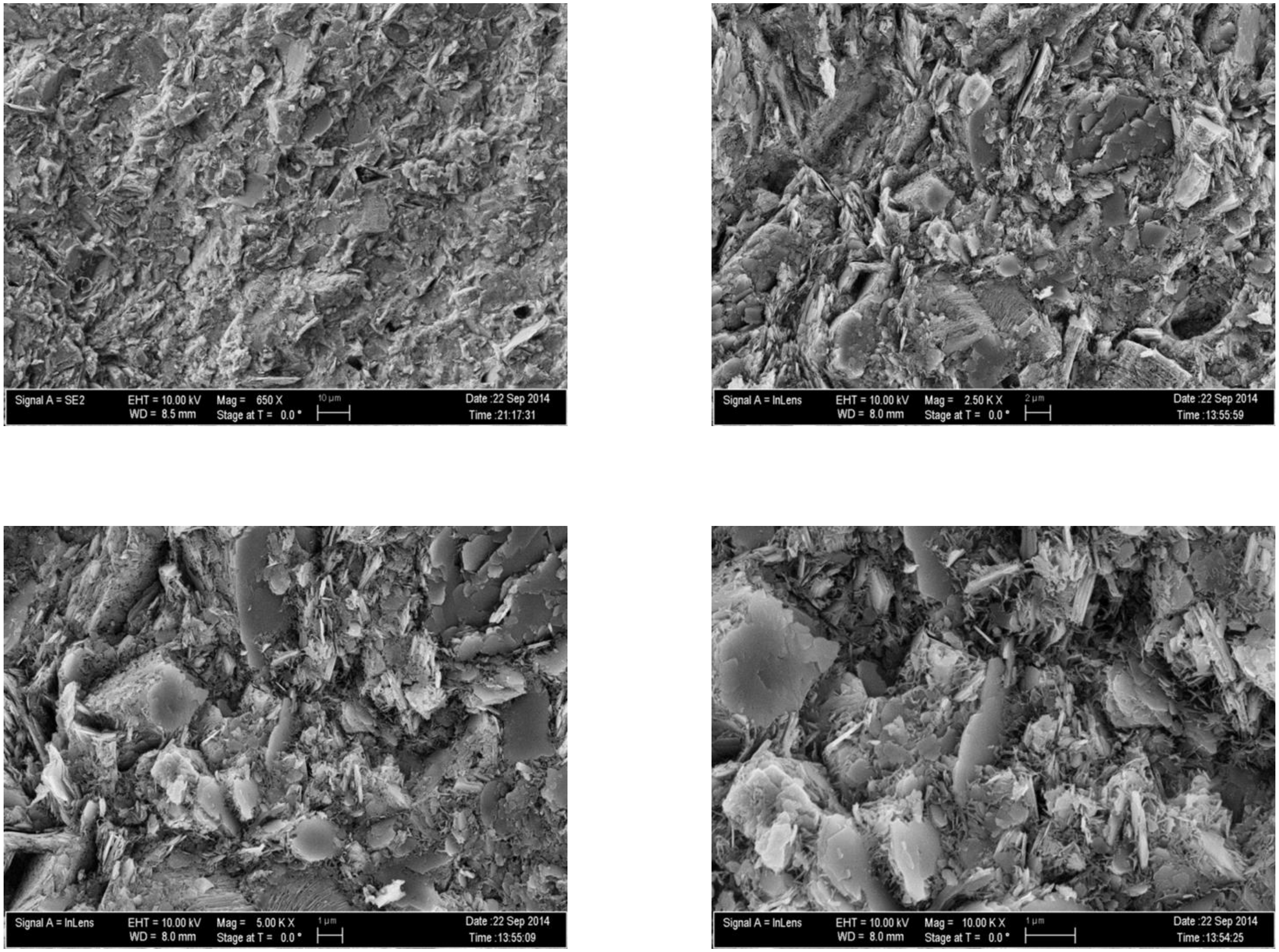

Figure 4.63: SEM Micrographs of Vertical Planes of 14-day Cured Samples at Different Magnifications

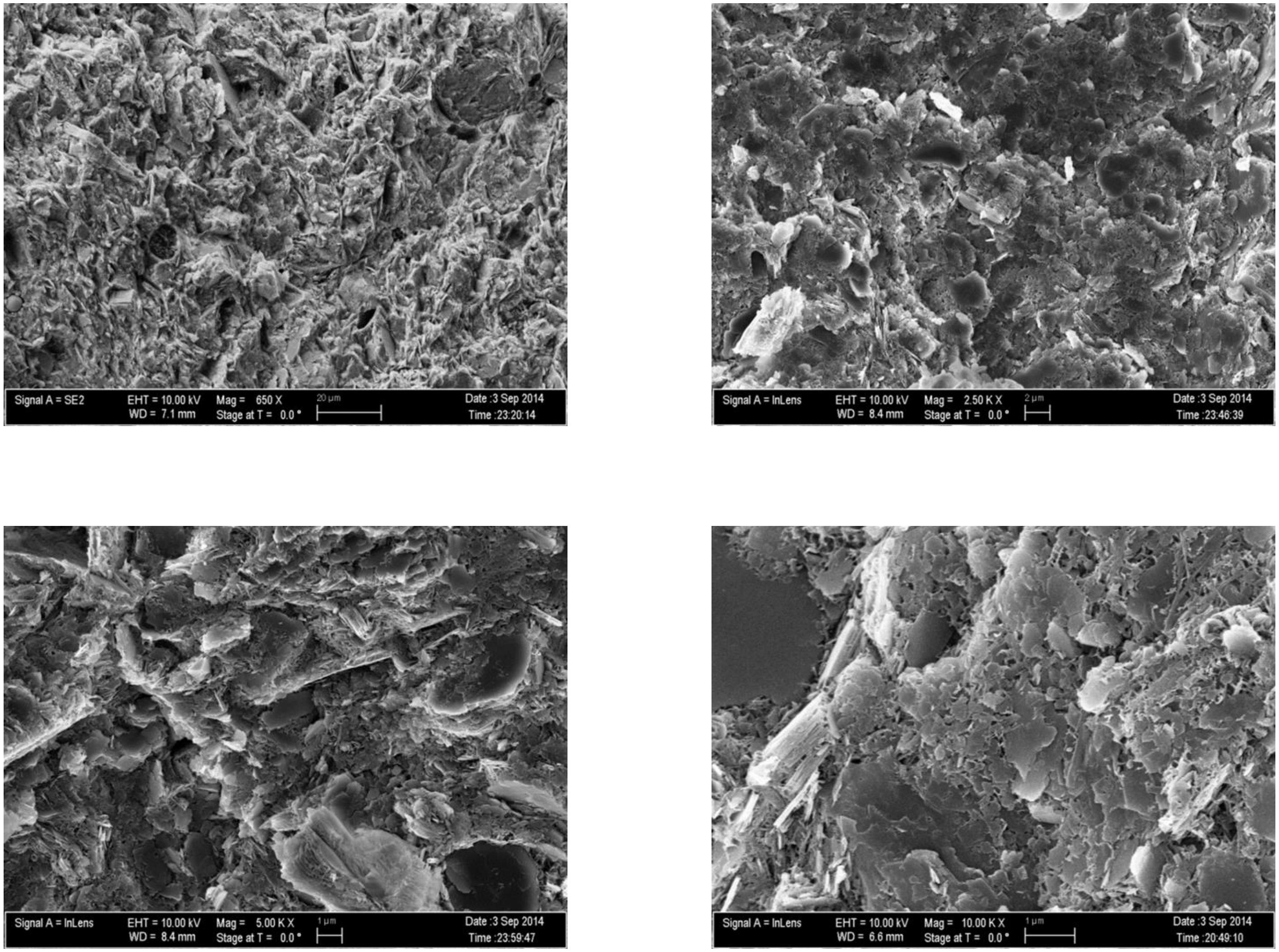

Figure 4.64: SEM Micrographs of Horizontal Planes of 28-day Cured Samples at Different Magnifications

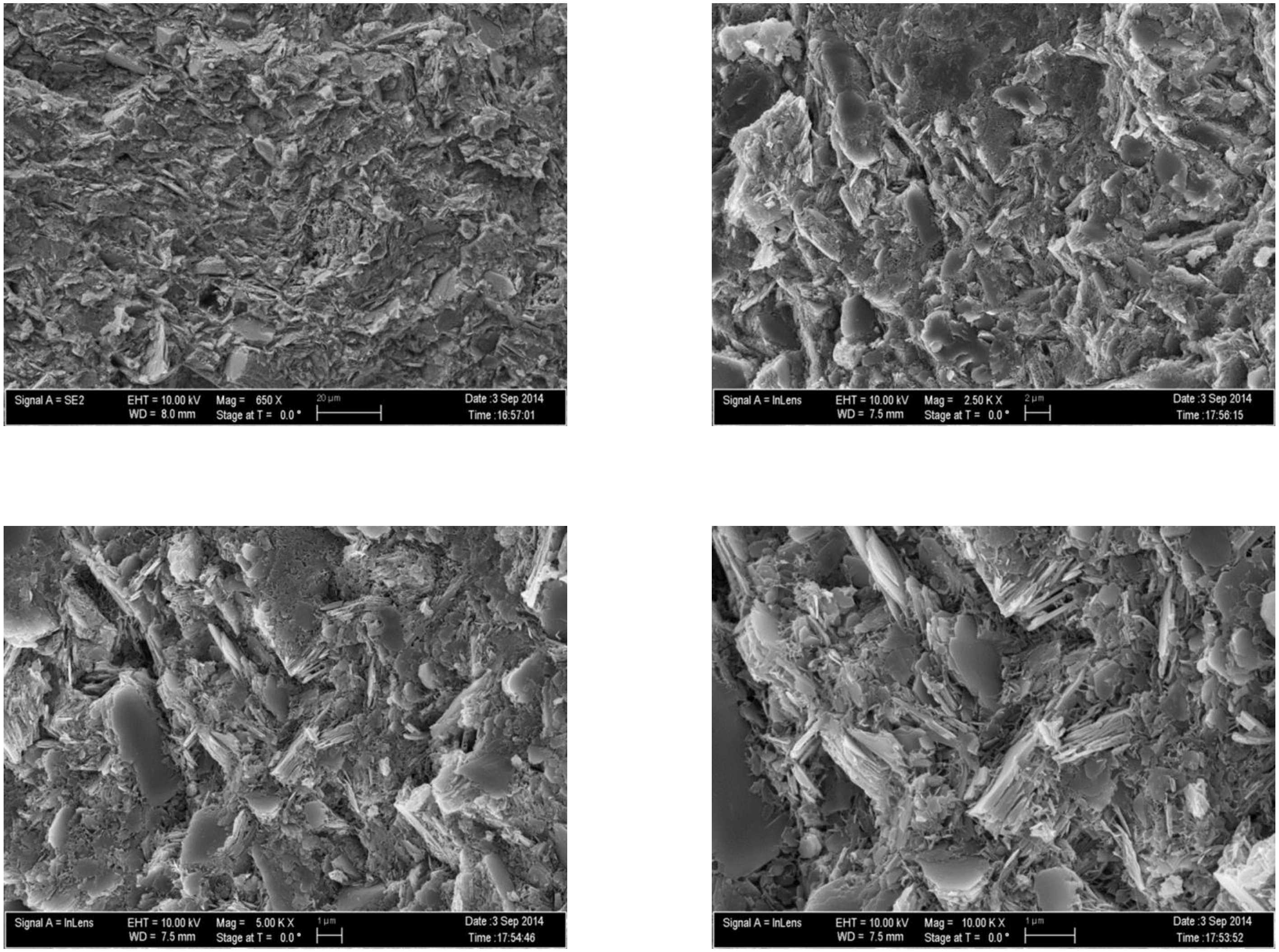

Figure 4.65: SEM Micrographs of Vertical Planes of 28-day Cured Samples at Different Magnifications

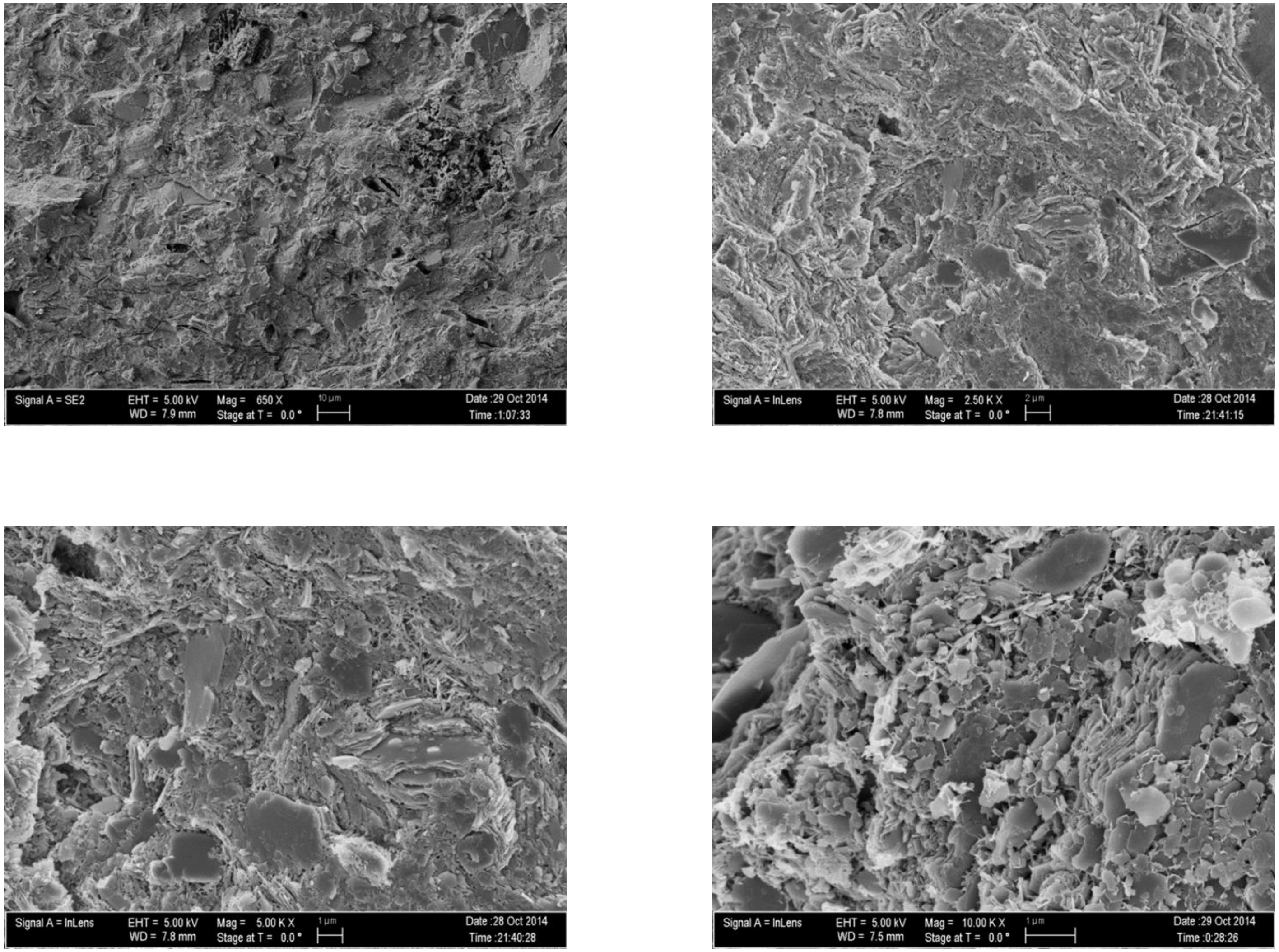

Figure 4.66: SEM Micrographs of Horizontal Planes of 90-day Cured Samples at Different Magnifications

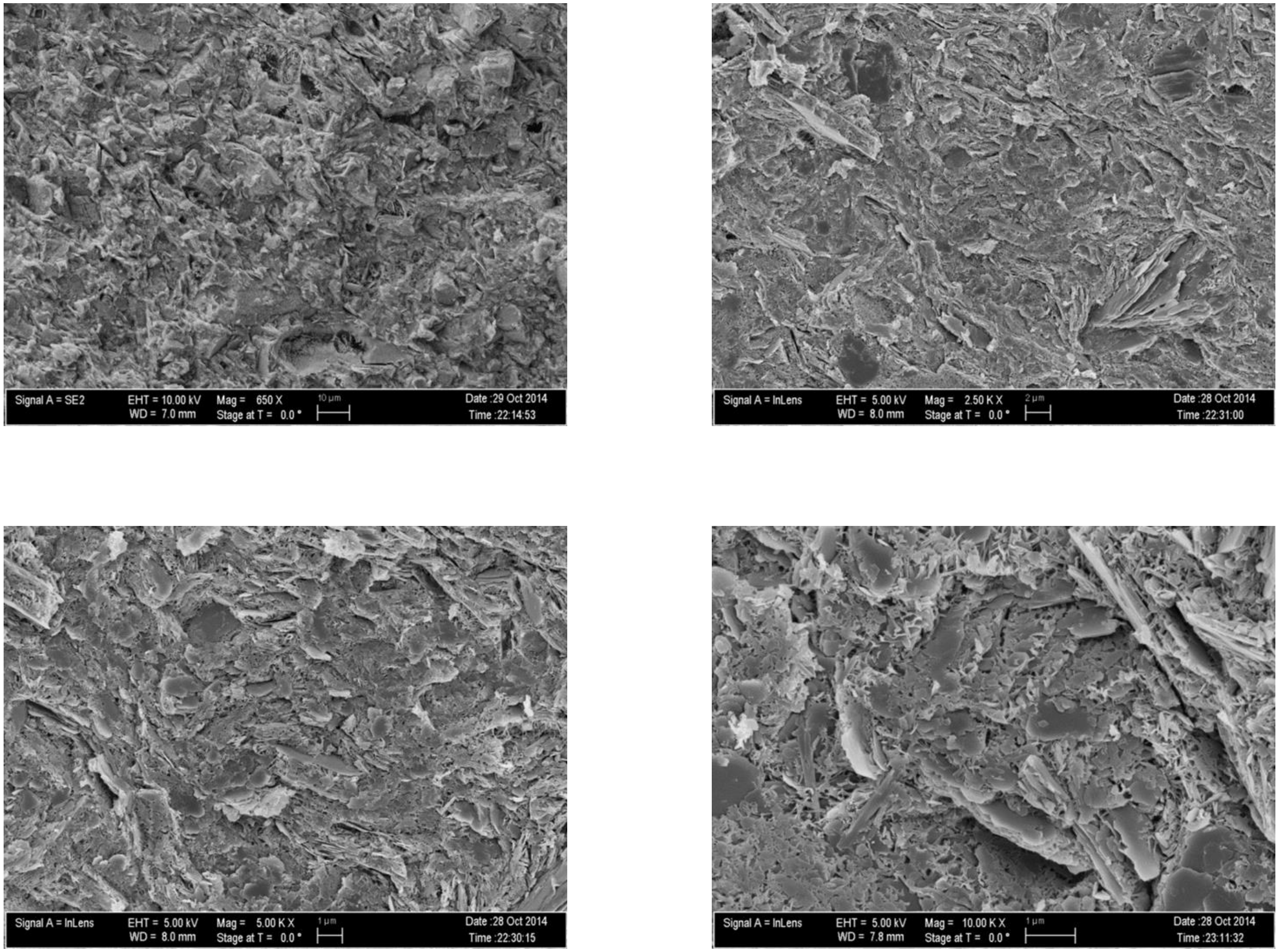

Figure 4.67: SEM Micrographs of Vertical Planes of 90-day Cured Samples at Different Magnifications

Micrographs of the 14, 28, and 90-day cured samples reveal an open structure and a flocculated fabric. The formation of a well-developed reticular network resembling a net is evident and is attributed to the increase in the amount of CSH also known to have a reticular morphology (Kamruzzaman et al. 2009). Two micrographs illustrating the honey-combed or reticular structure of CSH are shown in Figure 4.68. Kaolinite particles appear to be all connected together by CSH fibers forming a continuous matrix resulting in an abundance of tiny pores between particles (intra-aggregate pores). The size of the kaolinite particles show noticeable decrease with increasing curing time compared to the raw sample. The dissolution of the clay particles due to the addition of stabilizer is apparent and the typical hexagonal shape of kaolinite is often missing. An image analysis program can be used to measure and monitor the change in average particle size with curing time. Large pores are rarely encountered, and when found most are filled by cementitious products. An example of a CASH crystal filling a void space is presented in Figure 4.69. Monosulfate crystals in the form of thin hexagonal plates or irregular rosettes are similarly encountered and an example is shown in Figure 4.70. Hydrotalcite or $[Mg_{0.75}Al_{0.25}(OH)_2](CO_3)_{0.125}(H_2O)_{0.5}$ which is a layered double hydroxide is also sometimes found in these samples. A relatively large agglomeration of hydrotalcite crystals showing a typical blade-like structure is presented in Figure 4.71. Small spherical shapes in nanometer size range are sometimes visible accompanying other crystals such as those seen with the monosulfate and hydrotalcite crystals in Figure 4.70 and Figure 4.71. These may be some carbonate precipitates such as calcite, but it remains hard to identify them with certainty using

SEM/EDS. Other hydration products also appear to precipitate or form on the surfaces of the clay particles as illustrated in Figure 4.72.

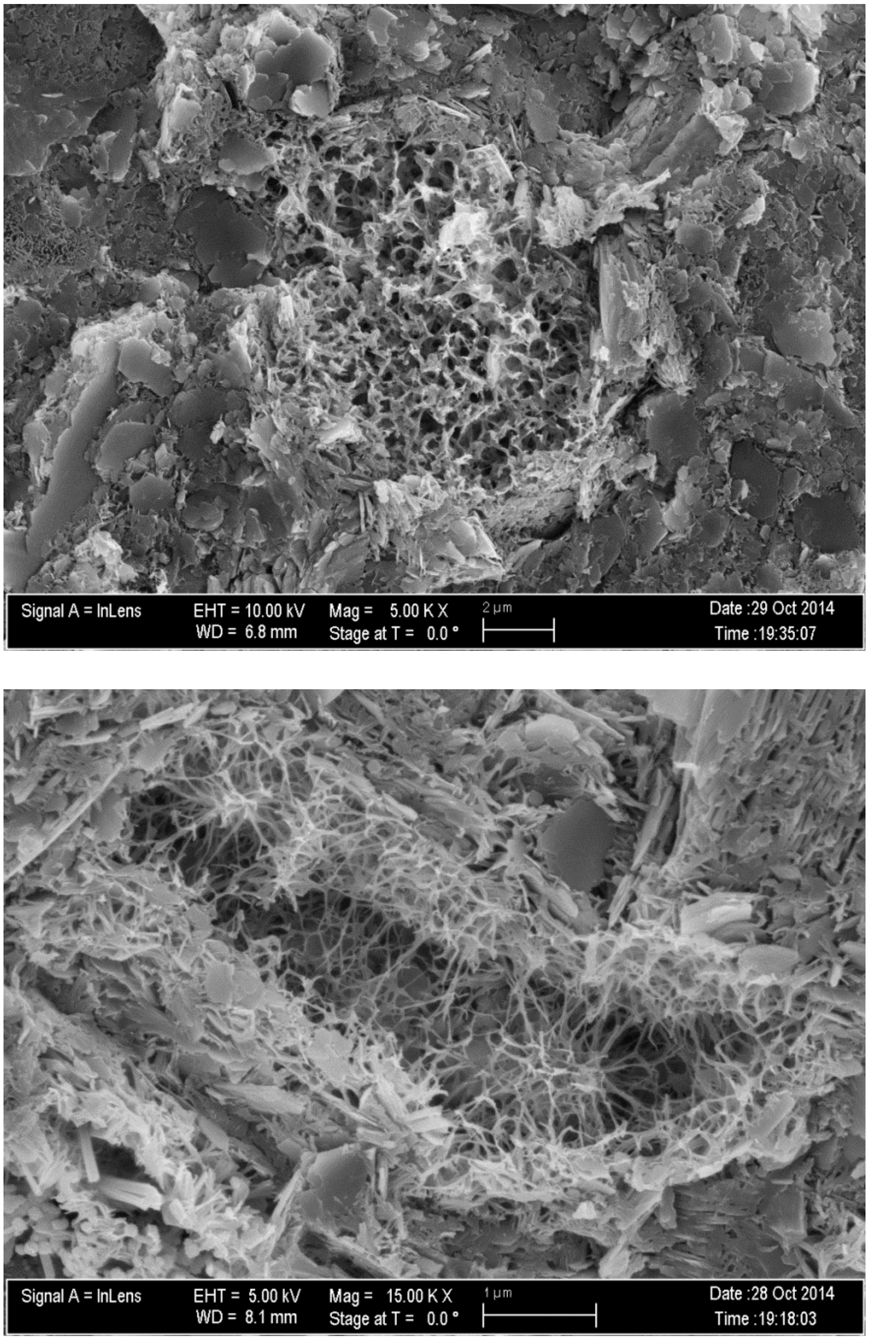

Figure 4.68: Micrographs of CSH Network of Reticulation in 90-day Cured Samples

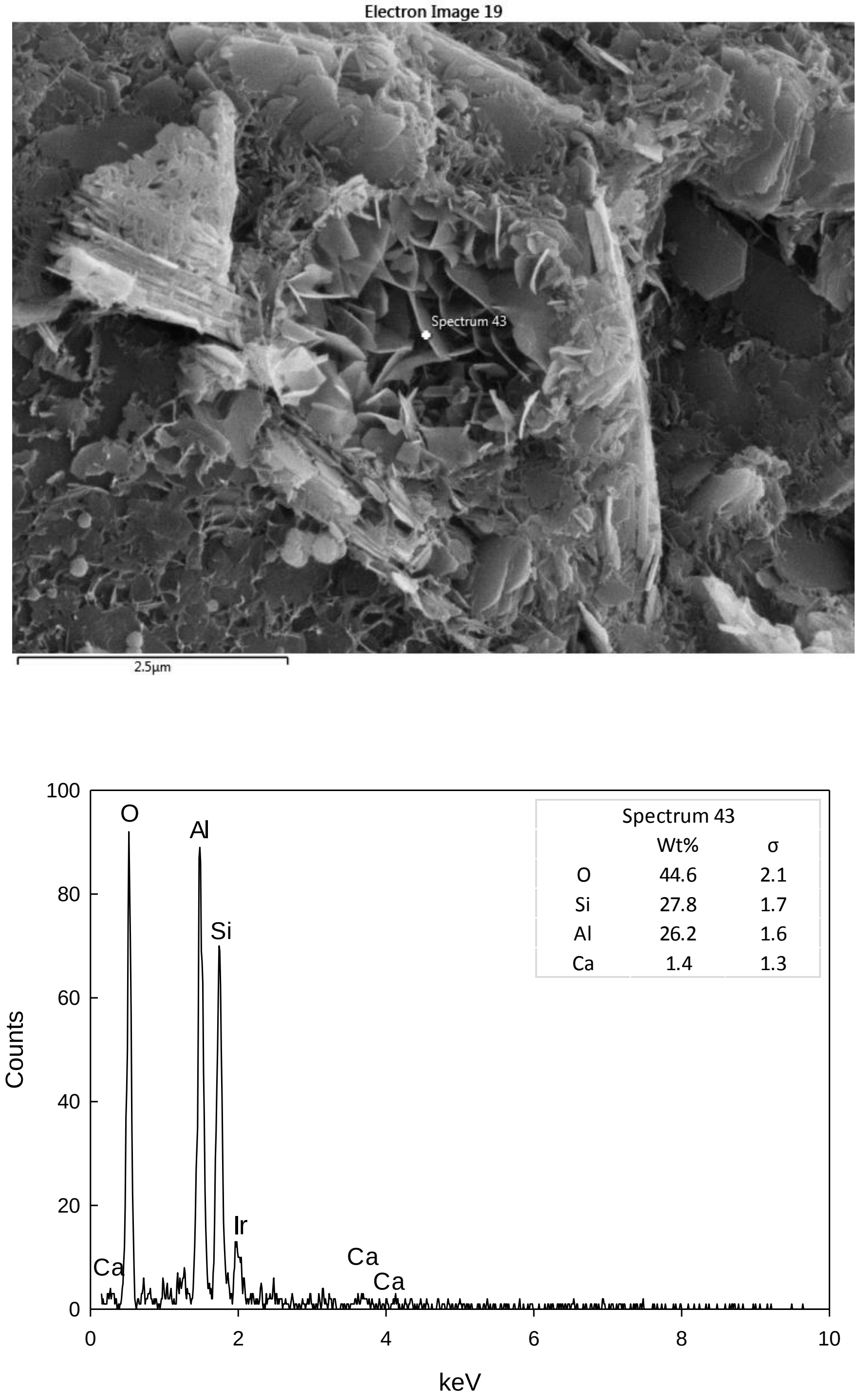

Figure 4.69: Micrograph of CASH Crystals Growing in Void Spaces in 90-day Cured Samples (top) and Corresponding EDS Spectrum (bottom)

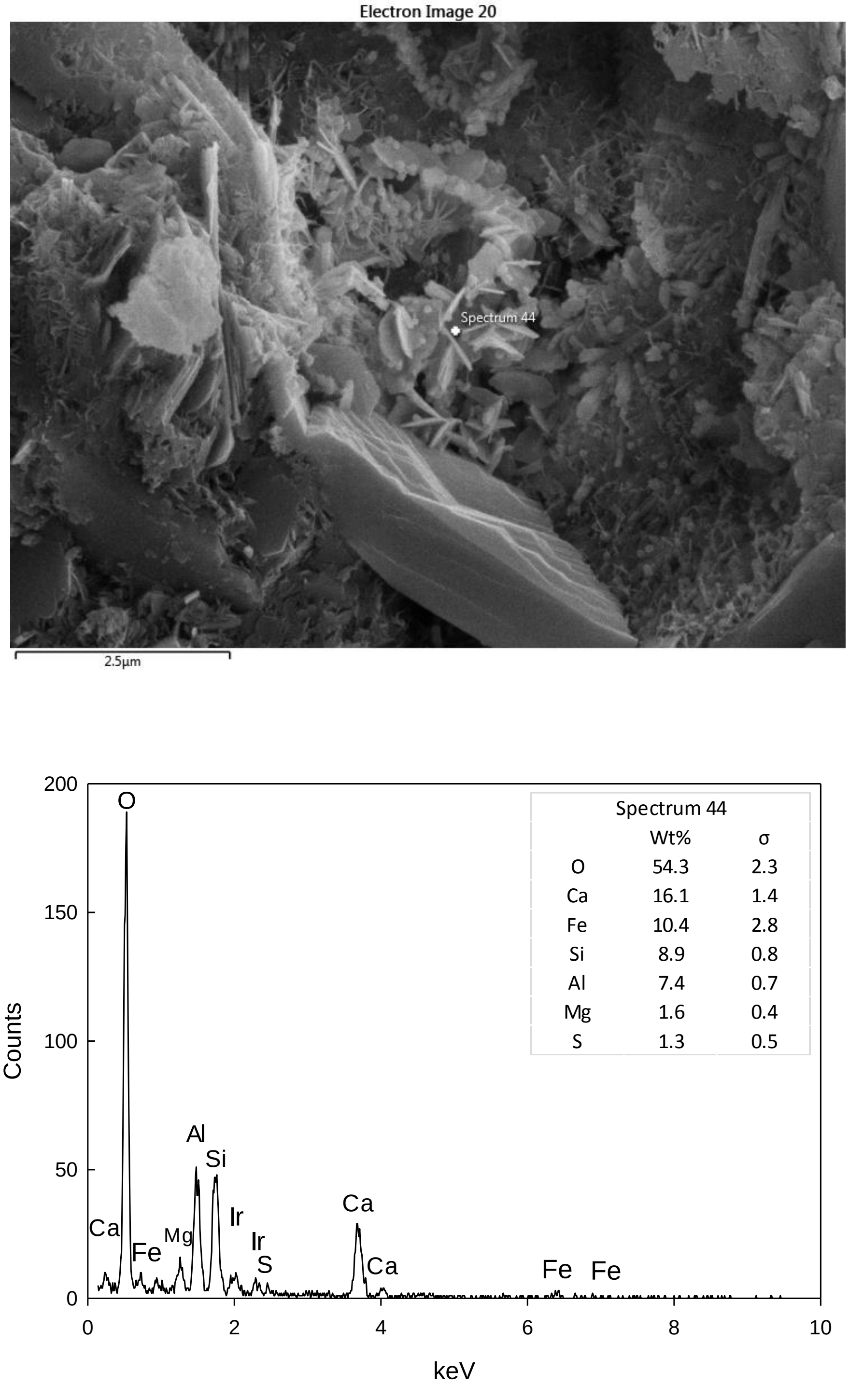

Spectrum 44

	Wt%	σ
O	54.3	2.3
Ca	16.1	1.4
Fe	10.4	2.8
Si	8.9	0.8
Al	7.4	0.7
Mg	1.6	0.4
S	1.3	0.5

Figure 4.70: Micrograph of Monosulfate Crystals in 90-day Cured Samples (top) and Corresponding EDS Spectrum (bottom)

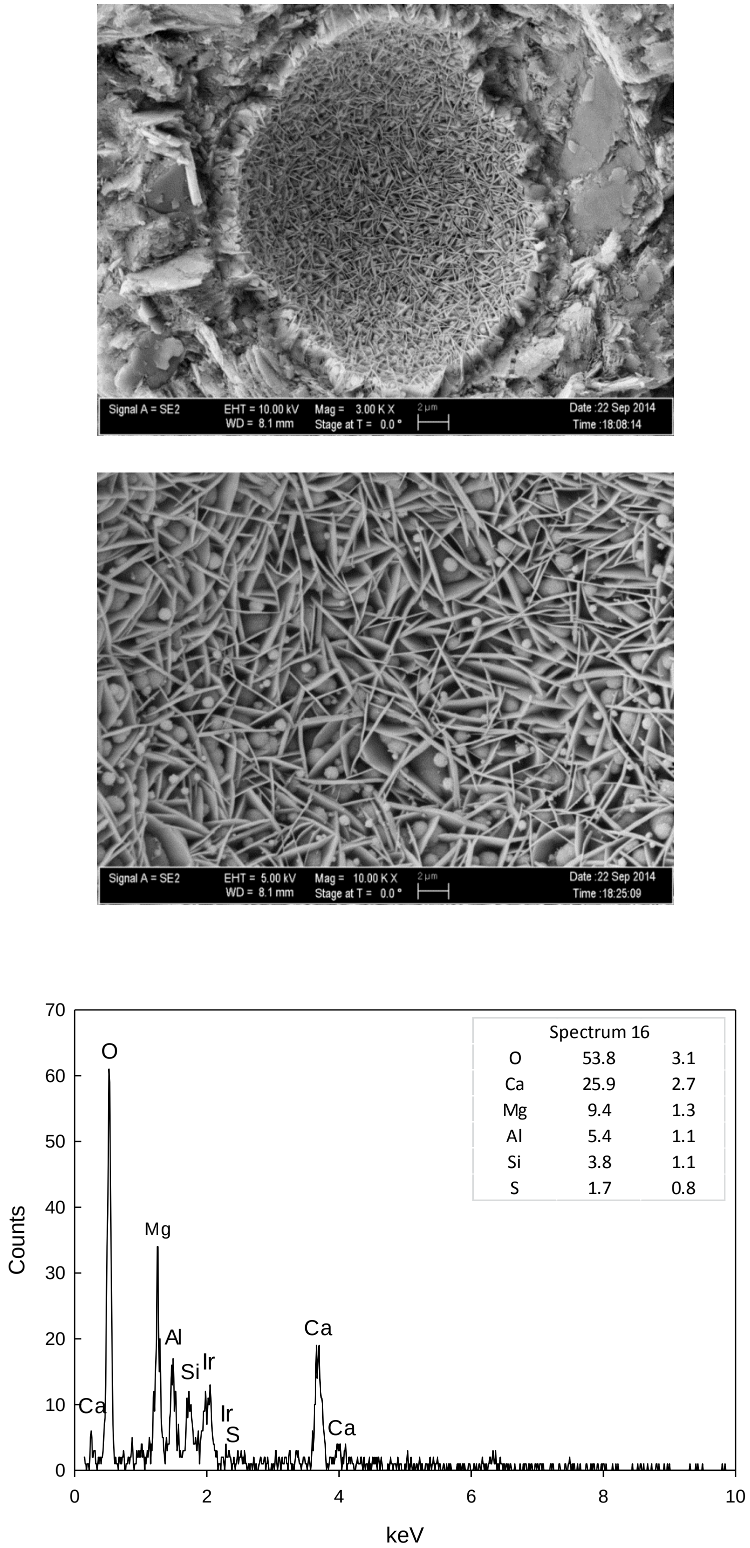

Spectrum 16		
O	53.8	3.1
Ca	25.9	2.7
Mg	9.4	1.3
Al	5.4	1.1
Si	3.8	1.1
S	1.7	0.8

Figure 4.71: Micrographs of Hydrotalcite Crystals in 14-day Cured Samples with Corresponding EDS Spectrum

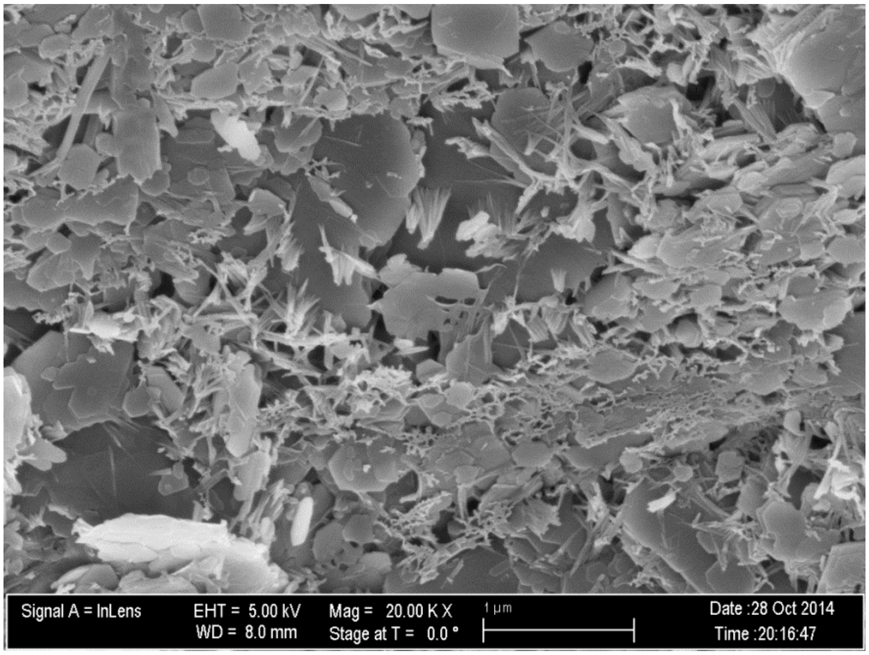

Figure 4.72: Hydration Products on the Surfaces of Clay Particles in 90-day Cured Samples

4.4.2 MIP

For the microstructure analysis using MIP, one cubic sample was cut from each UCS sample after shearing and from the fourth sample that was not subjected to an unconfined compression test. The purpose of analyzing samples from the same cure time, both before and after shear, was to determine the microstructural changes and how those changes could help explain soil strength just before failure. The cubic sample was recovered from the middle layer, whenever possible, except when the layer was totally broken after shear, and then freeze-dried as described in detail in the previous chapter. The correlation between the porosity obtained from MIP measurement and the porosity calculated based on phase relations of all samples is presented in Figure 4.73.

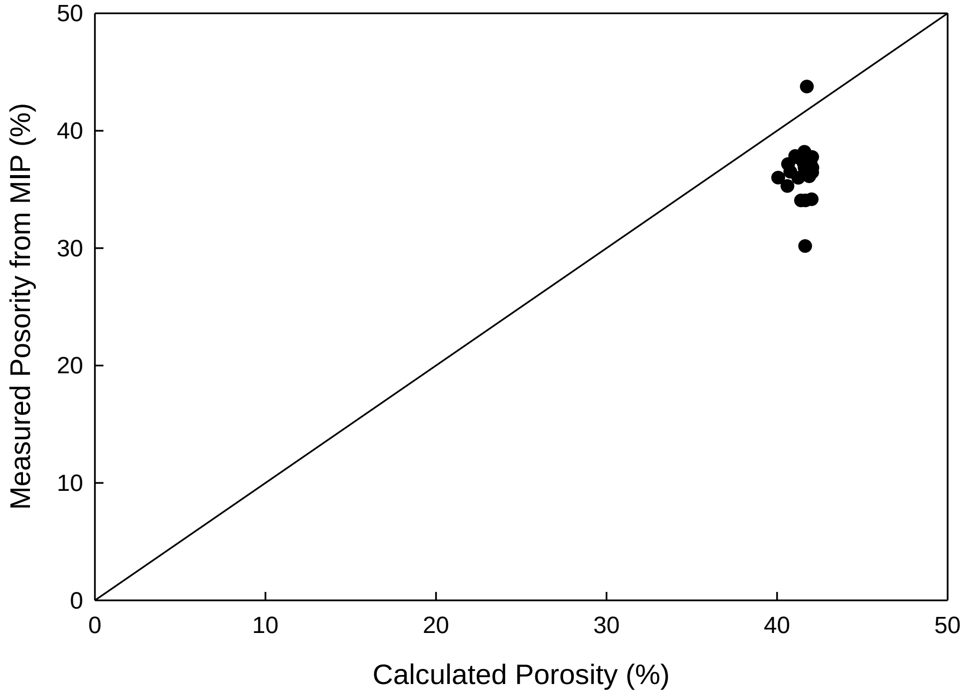

Figure 4.73: Comparison between Porosity from MIP and Calculated Porosity

All samples are reasonably plotted near the 1:1 line, and all except one are located below the line. The MIP method is typically known to underestimate the porosity due to several limitations. The porosimeter used in this study is capable of measuring pore diameters from about 0.003 to 400 μm. Thus, the maximum pressure provided by the apparatus is not capable of entering pores smaller than 0.003 (non-intruded porosity) and the minimum pressure limits the largest pore size that can be detected (non-detected porosity). In addition, the mercury is not able to fill isolated pores that are fully enclosed by soil particles; this enclosed porosity is considered insignificant in soils (Romero and Simms 2008).

The comparison between the sheared samples and the un-sheared samples at each curing time is revealed in Figure 4.74 through Figure 4.79.

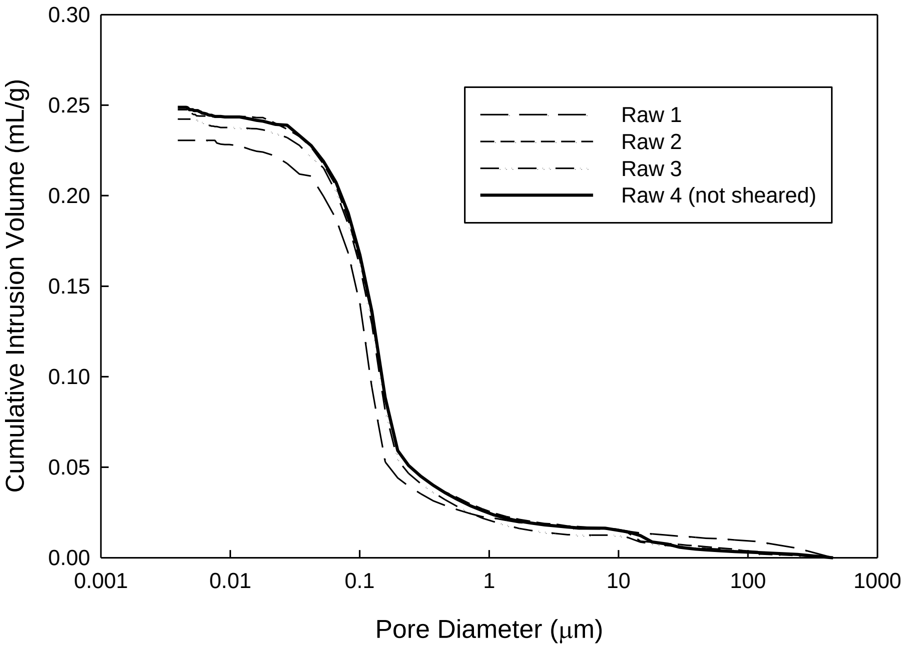

Figure 4.74: Comparison between Sheared and Un-sheared Raw Kaolinite Samples

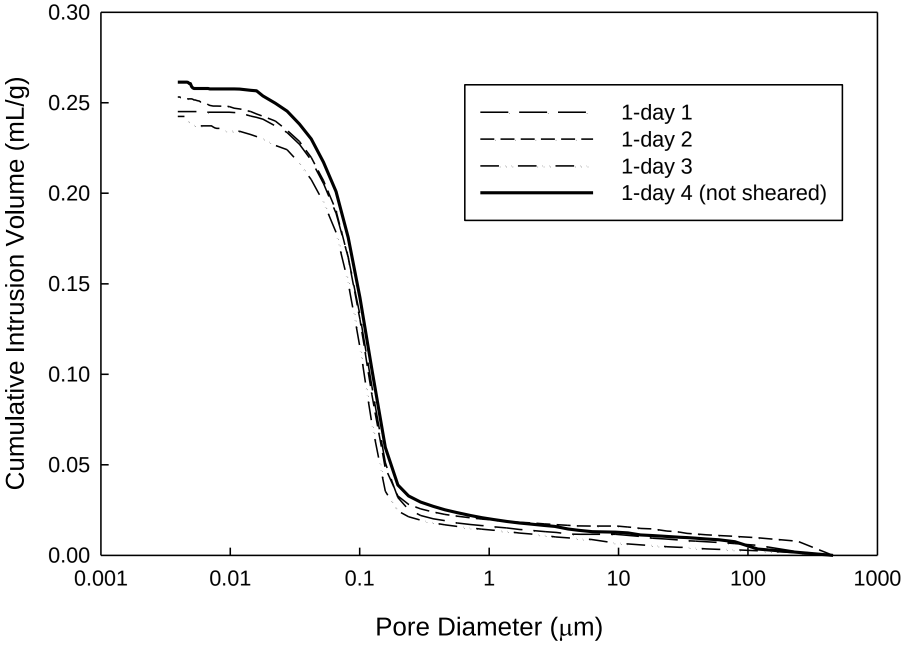

Figure 4.75: Comparison between Sheared and Un-sheared 1-day Cured Samples

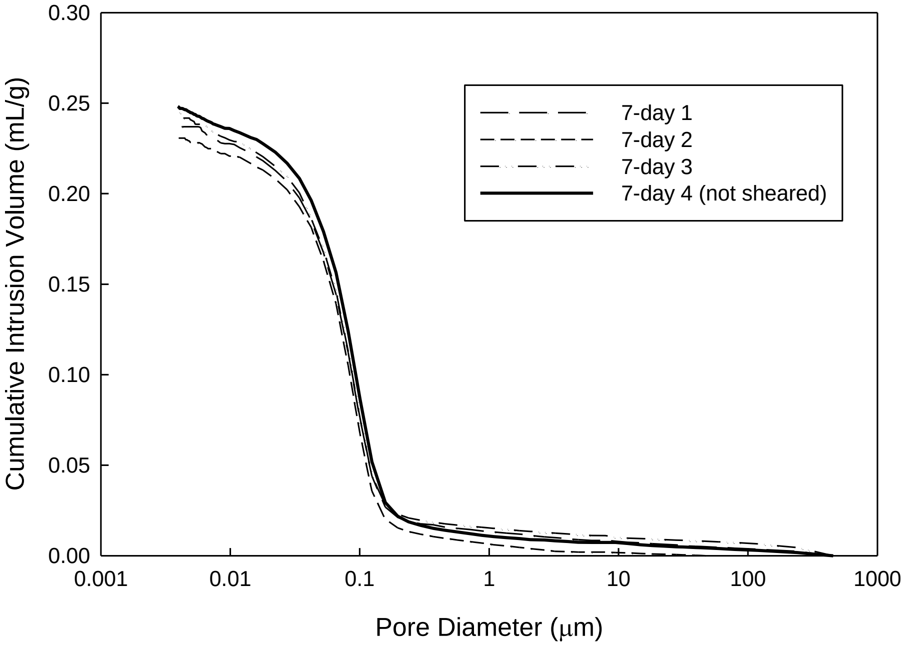

Figure 4.76: Comparison between Sheared and Un-sheared 7-day Cured Samples

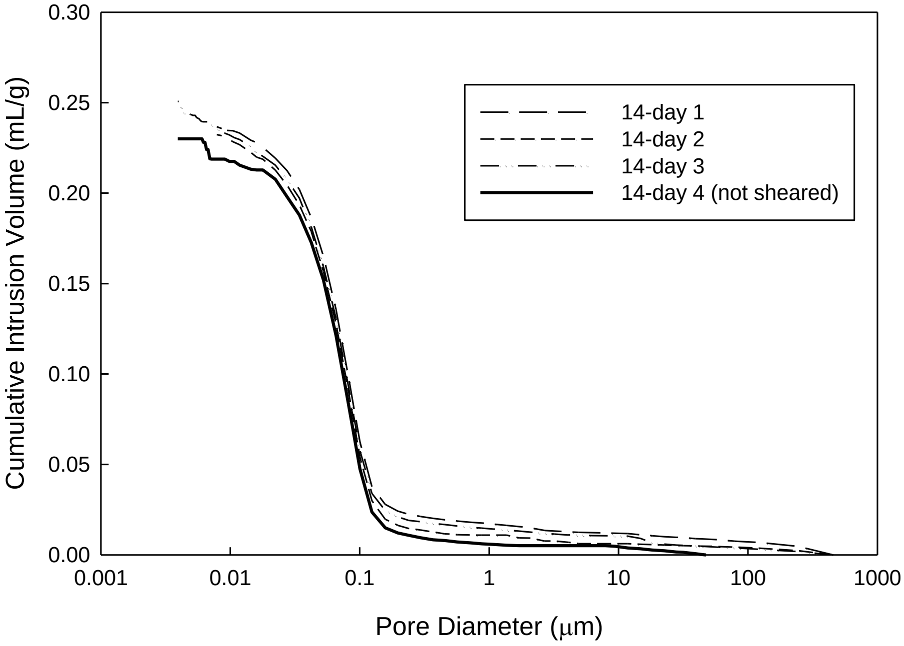

Figure 4.77: Comparison between Sheared and Un-sheared 14-day Cured Samples

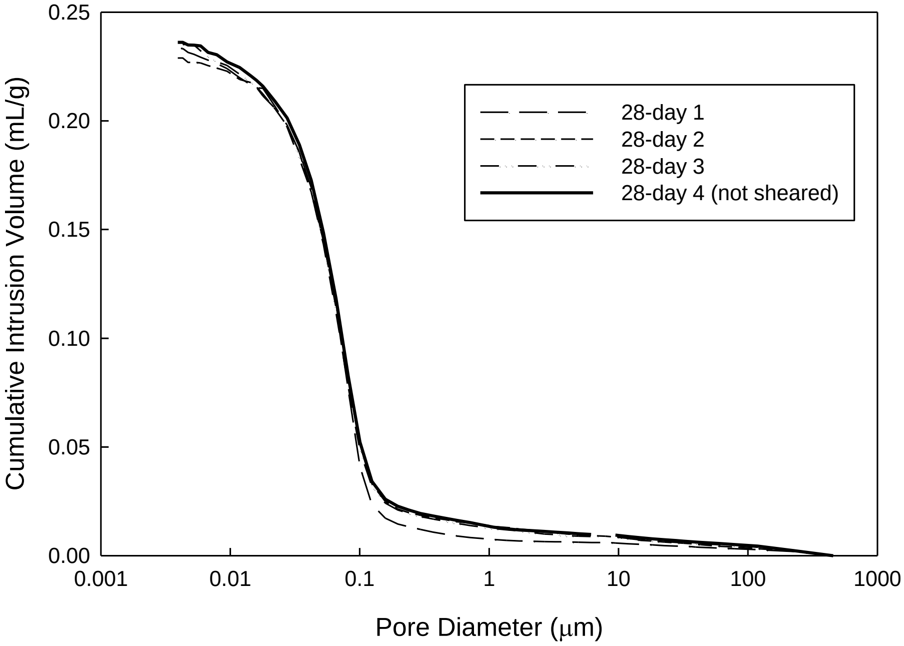

Figure 4.78: Comparison between Sheared and Un-sheared 28-day Cured Samples

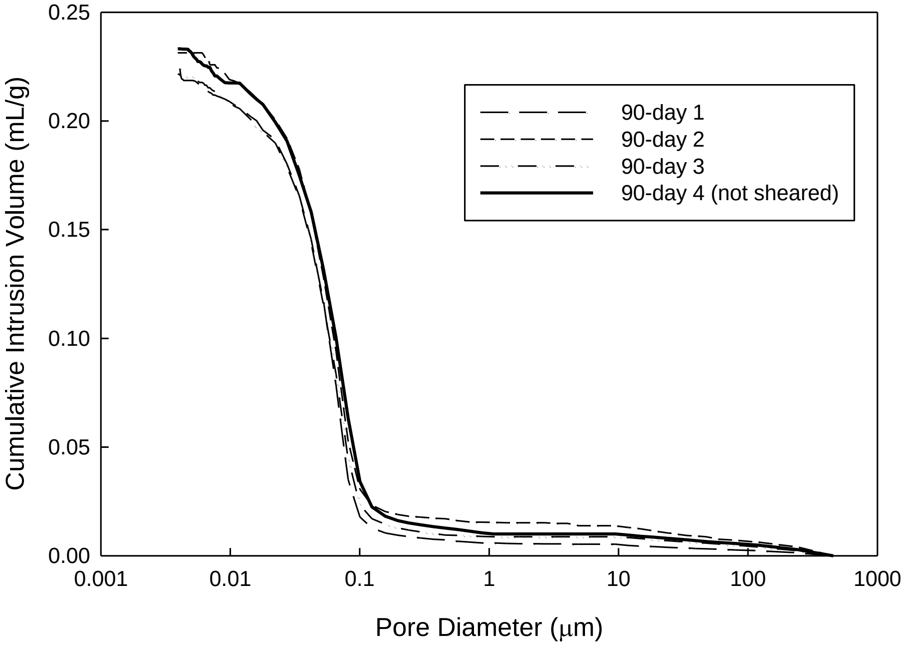

Figure 4.79: Comparison between Sheared and Un-sheared 90-day Cured Samples

With the exception of the 14-day cured samples, all un-sheared samples consistently have a larger cumulative intrusion volume, although by a small margin, compared to their sheared counterparts. As expected, the shearing process compresses the samples resulting in a final porosity smaller than the original one. In the case of the 14-day cured and un-sheared sample, the discrepancy may be caused by local variability in density, or possibly due to instrumental problems given the odd shape of the curve at small pore sizes. The cumulative pore size distribution curves for samples cured for the same time are very similar and yield a narrow band. These small differences are mainly due to the inherent variation among samples. From this point on, an average cumulative pore size distribution is generated and compiled from the individual cumulative pore size distributions of the sheared samples cured for the same time to make further representation of the results clearer. As an example, the average cumulative pore size distribution for the sheared 1-day cured samples is shown in Figure 4.80.

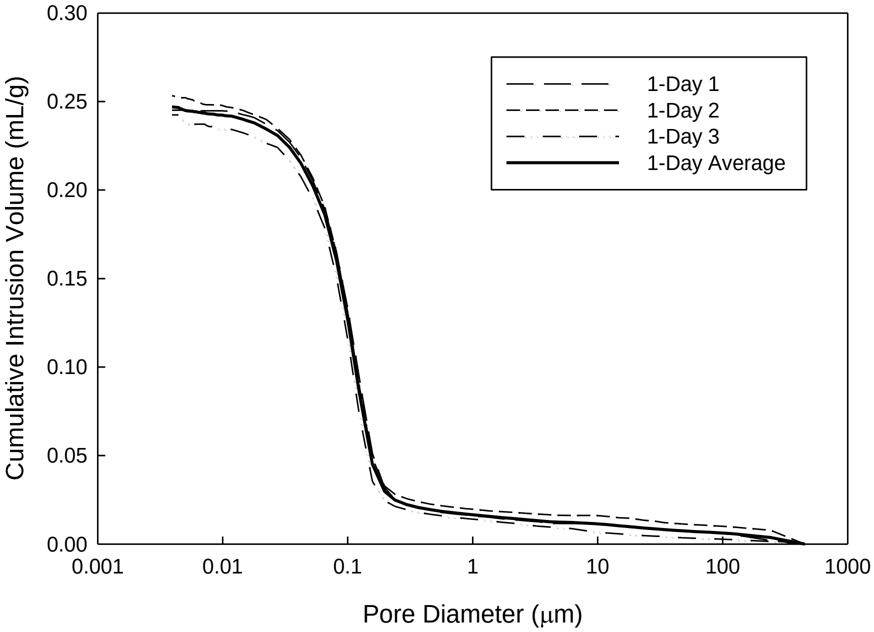

Figure 4.80: Average Cumulative Pore Size Distribution for Sheared 1-day Cured Samples

Plots of incremental intrusion volume versus pore size for all the tests were generated, averaged for the sheared samples cured for the same time, and presented in Figure 4.81.

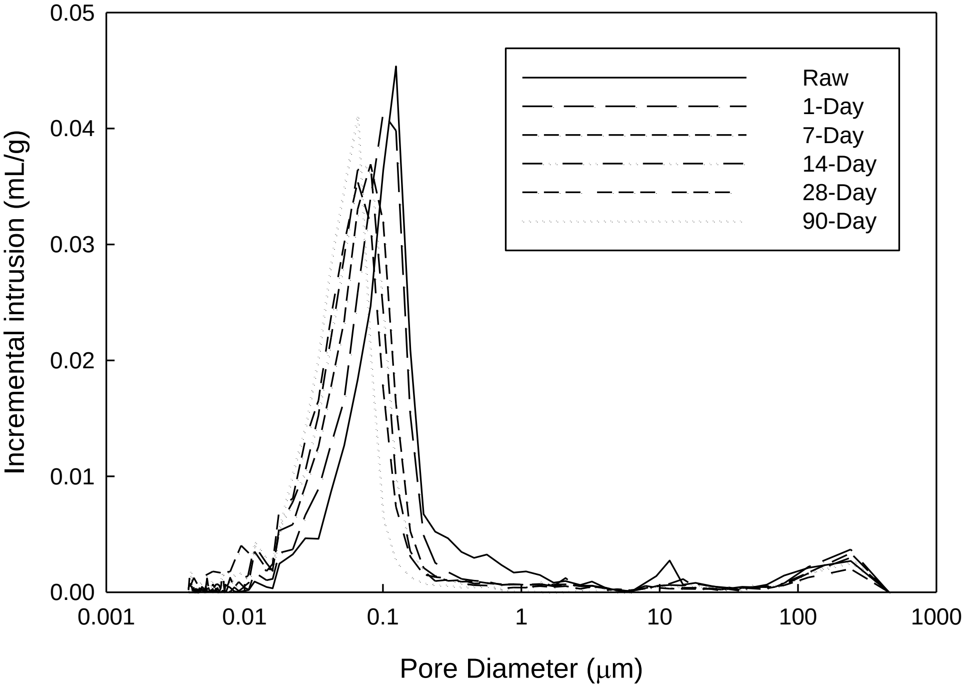

Figure 4.81: Average Incremental Intrusion Curves of Sheared Samples at each Curing Time

This graph is commonly used in MIP testing and permits better observation of the dominant pore, and in this case, monitor its evolution with curing time. As can be seen from Figure 4.81, the raw soil shows a weak dual-porosity structure with the main peak at about 0.12 μm and a small peak at about 11.82 μm. The third small peak at about 240 μm, common among all the samples, cannot be reliably measured due to the lack of precise control of low pressures on high volumes of mercury (Koliji et al. 2010). The dual-porosity structure is typically formed in compacted soils and describes the intra-aggregate and inter-aggregate pores (Romero and Simms 2008, Li and Zhang 2009, Koliji et al. 2010). The weak bimodal distribution in the case of this raw soil may be due to the presence of a single mineral only, kaolinite, and the fact that it was compacted at optimum moisture content which prompts the formation of a dispersed fabric. A broad shoulder is also noticeable on the right side of the main peak for the raw soil signifying the presence of larger pores compared to the rest of the samples. The pore size distribution quickly shifts from a weak bimodal distribution to a unimodal distribution for the stabilized soil even at early curing times, with the disappearance of the inter-aggregate pores. Choquette et al. (1987) noticed that when clays are treated with lime, flocculation occurs rapidly and this microstructure is sustained during the maturation process. A closer look at Figure 4.81 reveals that the dominant pore size slowly but steadily shifts to smaller pore sizes with curing time from about 0.12 μm for the raw soil to 0.06 μm for the 90-day cured sample.

To provide a better observation of the evolution of the porosity and pore size distribution with curing time, the relationship of the incremental volume with curing time and the percent incremental intrusion with curing time are presented in Figure 4.82 and Figure 4.83. It should be noted here that the pore size distribution obtained from the MIP test may not exactly represent the true distribution of the pores due to the several limitations of the MIP as discussed earlier. Moreover, larger pores with smaller pore entrance size are not detected until the intrusion pressure is large enough to penetrate the smaller pores (i.e. constricted porosity), thus leading to small inaccuracies in the pore size distribution. Despite these limitations, the pore size distribution obtained from the MIP is still considered very useful and provides a quantitative characterization of the microstructure (Romero and Simms 2008). The evolution of porosity can be deduced from the progress of the intrusion volume with curing time as illustrated in Figure 4.82. The porosity appears to generally decrease with increasing curing time.

Choquette et al. (1987) reported an insignificant and irregular total pore volume variation in four lime-treated soils cured for 0, 30, and 300 days. Conversely, a graph of pore volume versus curing time reported by Horpibulsuk et al. (2010) shows a decrease in porosity with curing time. The small decrease in porosity as observed in this study is consistent with the formation of cementitious products in the cement-stabilized soil with increasing curing time. The percentage of incremental intrusion for each pore size range shown in Figure 4.83 better describes the trends in the evolution of the pore size distribution. The larger pores, between 0.1μm and 10μm are greatly diminishing at the expense of the smaller pores (smaller than 0.1μm) that are increasing with increasing curing time. This relationship is captured in Figure 4.84 and shows an excellent correlation between the decrease of the large pores and the increase in small pores with an R^2 equal to 0.999. This observation further confirms that the cementitious products are being formed in the larger pores resulting in their partitioning into a larger number of smaller pores.

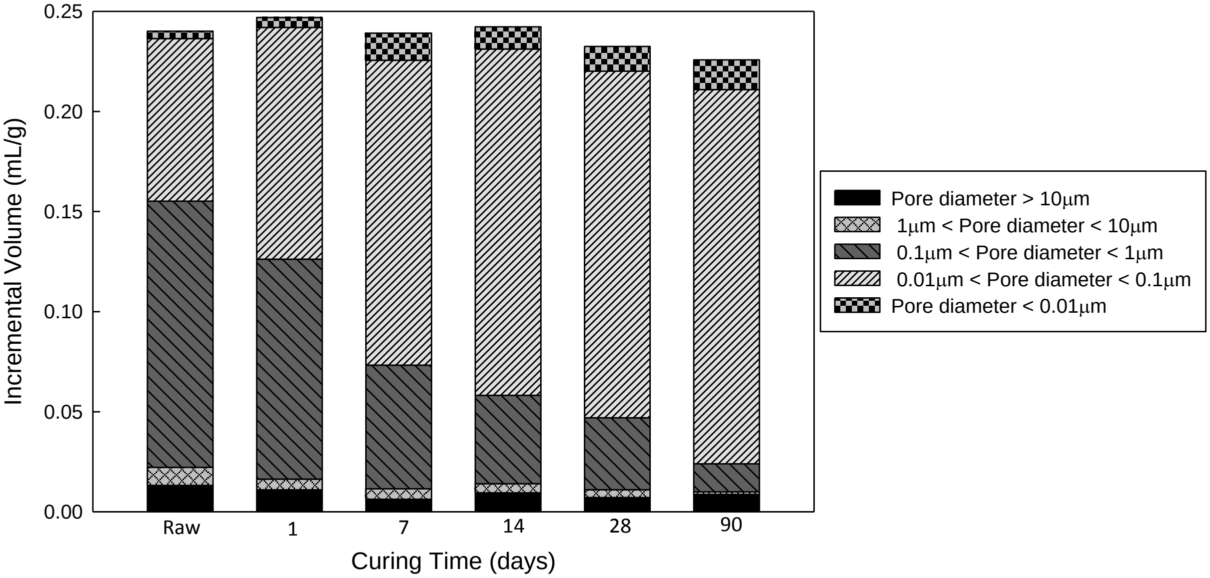

Figure 4.82: Evolution of Pore Size Distribution with Curing Time

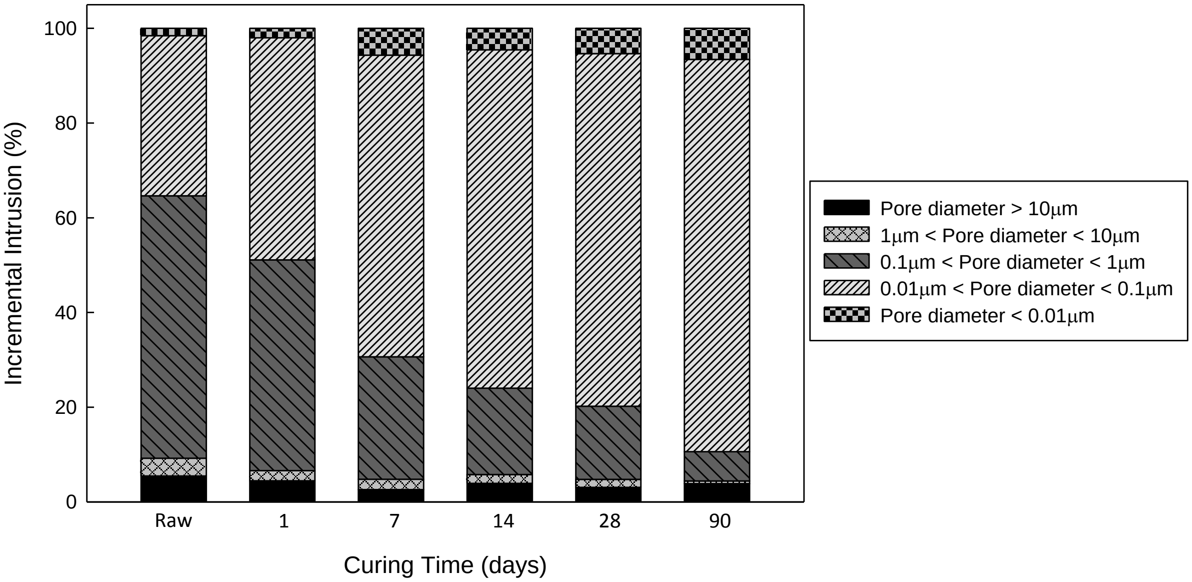

Figure 4.83: Percentage Pore Size Distribution at Different Curing Times

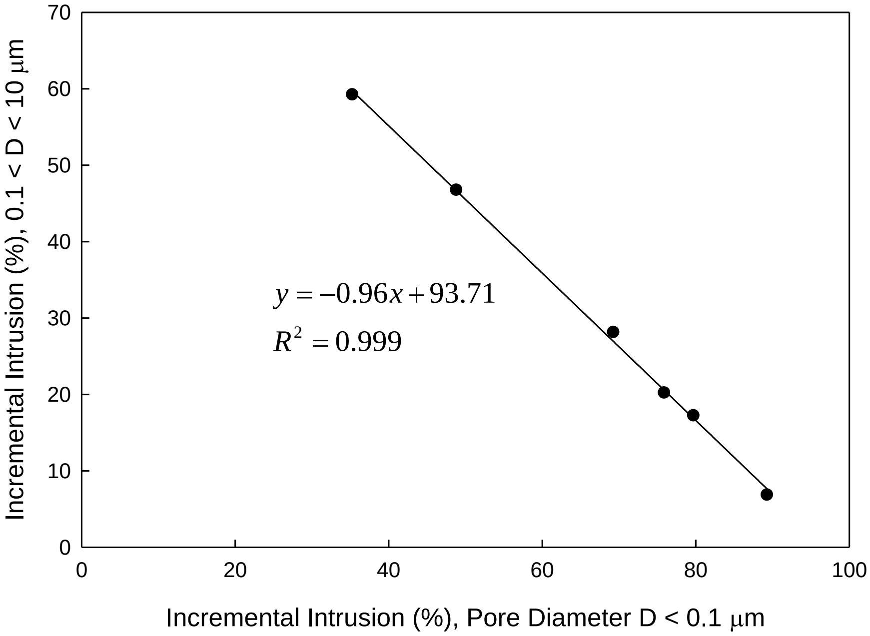

Figure 4.84: Relationship between Large Pores and Small Pores

As previously mentioned in section 4.3, the stabilization process causes the kaolinite to dissolve which contributes to the formation of cementitious products via pozzolanic reactions and then in turn results in the partitioning of the large pores into an increasing number of smaller pores. The relationship between the percentage of incremental intrusion of the pores with diameters smaller than 0.1 μm and the kaolinite to corundum ratio is presented in Figure 4.85 and shows a very good linear correlation with an R^2 value of 0.89. In particular, the relationship between the percentage of incremental intrusion of the pores with diameters smaller than 0.1 μm and the amount of CSH formed (as estimated from the mass loss between 105 and 440 ^{o}C), which is the dominant cementitious product, is illustrated in Figure 4.86 and shows an excellent linear correlation with an R^2 value of 0.98. This observation further validates the connection among the various reactions taking place during the stabilization process.

Finally, the relationship between the unconfined compressive strength and the percent incremental intrusion of the pores with diameters smaller than 0.1 µm is illustrated in Figure 4.87. The excellent linear correlation ($R^2 = 0.98$) closes the loop on the sequence of all these reactions and shows how they tie all together. The increase in strength is directly related to the increase in the amount of small pores caused by the formation of cementitious products.

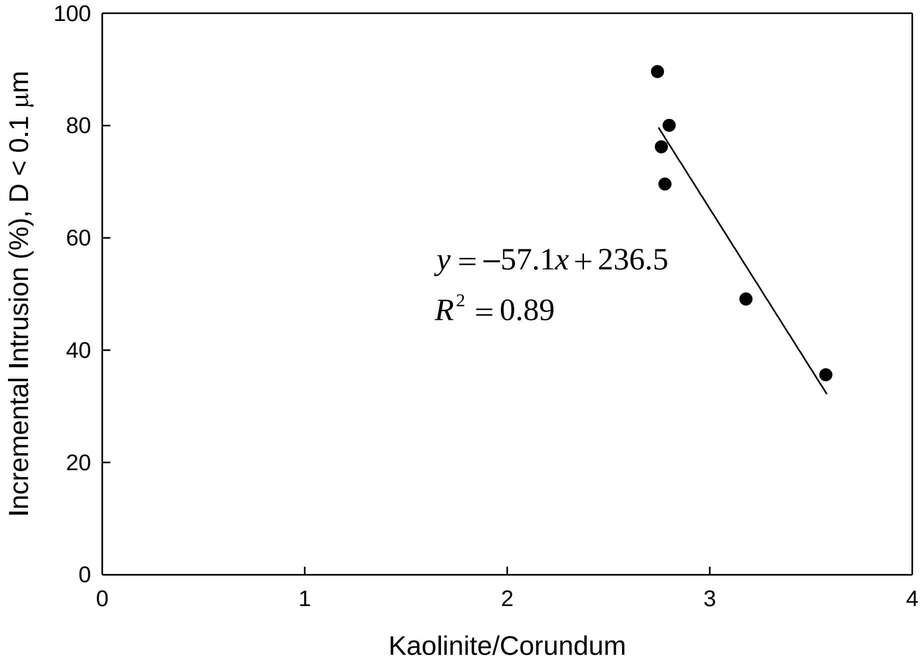

Figure 4.85: Correlation between Small Pores (D < 0.1 µm) and Kaolinite to Corundum Ratio

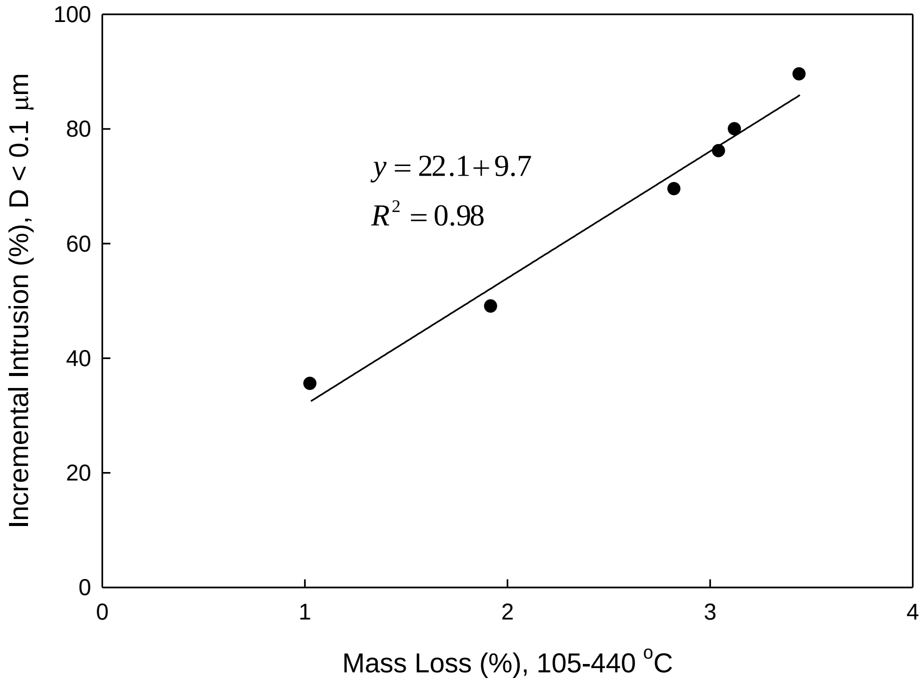

Figure 4.86: Correlation between Small Pores (D < 0.1 μm) and Amount of CSH

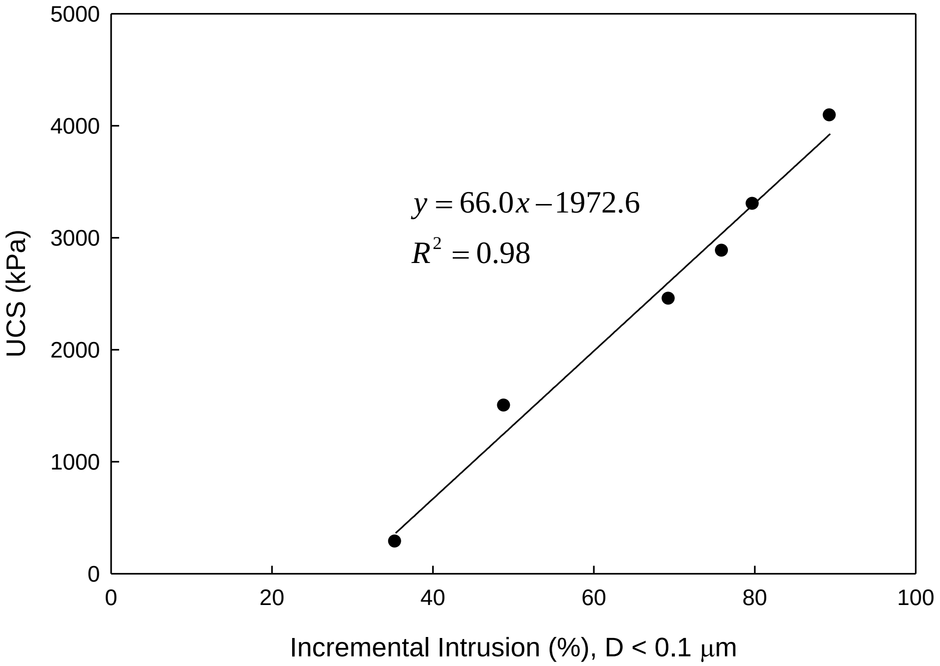

Figure 4.87: Correlation between UCS and Small Pores (D < 0.1 μm)

Chapter 5: Conclusions and Recommendations

5.1 Summary and Conclusions

The goal of this research study was to advance microstructure characterization of cement stabilized soils for better understanding of macroscopic behavior. An extensive set of laboratory tests extending across several disciplines such as engineering, geology, materials science, and geomechanics have been used in this study. They were accompanied by analytical methods and statistical models to produce insightful results that helped achieve the objectives.

The first objective of the research in support of this goal was to (i) investigate the effect of chemical stabilization on micro-scale properties and the corresponding change in macroscopic behavior, and this was achieved by performing laboratory experiments to disclose the common geotechnical and physicochemical characteristics of a manufactured soil, along with its stabilized counterpart. XRD, SEM, EDS, XRF, TG and MIP were conducted to reveal the mineralogy, structure, mineral distribution, elemental composition, and pore size distribution and the changes of these features attributed to chemical stabilization. The macroscopic behavior, in terms of unconfined compression strength, of the selected soil samples was quantified and all the microscale properties were compared to this macroscale behavior to explain the governing mechanisms controlling strength gain over curing time.

The second objective in support of the overall goal was to (ii) assess the role of the microscopic properties (e.g., mineralogical, structural) in the evolution of macroscopic behavior to better understand the fundamental behavior of clays. SEM micrographs of raw kaolinite showed a dispersed structure characterized by a high degree of preferred orientation whereas the structure of stabilized kaolinite was more flocculated. The gain in strength was attributed to the formation of hydration products, in particular CSH. The reason for this is mainly that CSH fibers were seen spreading rather continuously throughout the sample and binding the clay particles together. In contrast, all the remaining hydration products were encountered as discrete or isolated crystals. Cementitious products were easily observed filling void spaces and resulting in their partitioning into a large number of smaller pores. The kaolinite particles deformed and shrunk with increasing curing time compared to the raw soil as a result of their dissolution after the addition of stabilizer.

The thermal decomposition of kaolinite and its stabilized counterpart was examined using thermogravimetric analysis (TG) coupled with mass spectroscopy (MS) for evolved gas analysis with excellent repeatability and revealed that the mass losses in the kaolinite samples occurred at two temperatures, below 100 and at 527 ^{o}C. The first mass loss was attributed to desorption of evaporable water whereas the second was due to the loss of structural water removed by dehydroxylation. In the cement-stabilized soil, the first mass loss started below 100 ^{o}C but extended well above this temperature and was composed of several peaks indicating the decomposition of various compounds, mainly but not limited to CSH phases. The major peak at around 527 ^{o}C on the DTG curve did not shift as a result of stabilization despite the fact that calcium hydroxide which is a hydration product, decomposes at similar temperature range. The mass loss occurring beyond 580 ^{o}C was attributed to the decarbonation of calcite that formed due to soil stabilization. The temperature ranges reported in cement literature were used to calculate the corresponding mass losses for quantitative analysis. The results showed an excellent linear correlation between the increase in the amount of CSH as estimated from the mass loss between 105 and 440 ^{o}C and strength gain.

Mass spectrometry was successfully implemented to track the evolved gases and help confirm the decomposing phases. Water release was monitored by following the MS curves of the molecule ion water H_2O^+ (*m/z* 18) which was the most intense and the fragment ions OH^+ (*m/z* 17) and O^+ (*m/z* 16), and carbon dioxide was monitored by following the MS curve of CO_2^+ (*m/z* 44).

The final objective was to (iii) derive various relationships, preferably quantitatively, of these properties with the macroscopic behavior. The strength of cement-stabilized kaolinite increased in a logarithmic trend over time in accordance with previously reported studies (Circeo et al. 1962, Chrysochoou 2014). A linear relationship between the increase in the amount of calcium hydroxide, as calculated from the mass loss between 440 and 580 ^{o}C, and strength gain was found to be very good once raw kaolinite was excluded from the regression due to the fact that kaolinite and calcium hydroxide decompose at similar temperatures. Thus, caution should be used when analyzing TG results to avoid erroneously assigning mass losses to different compounds.

Quantitative X-ray diffraction (XRD) using whole-pattern fitting (Rietveld method) and the Reference Intensity Ratio (RIR) was implemented to calculate the amount of kaolinite and showed that it decreases logarithmically with curing time. A strong linear correlation was observed between the kaolinite to corundum ratio and the unconfined compressive strength. The quantitative analysis using the RIR method provided better results in comparison to the whole-pattern fitting in this case. These results could have been improved by experimentally producing the Powder Diffraction File (PDF) for the kaolinite used in this study. The whole-pattern fitting is a more robust quantification method and is expected to outperform the RIR method when the soil is more complex and/or the peaks of the internal standard overlap with other phases present in the soil.

MIP results revealed that un-sheared samples generally had a larger cumulative intrusion volume (higher porosity) than their sheared counterparts. MIP tests disclosed a weak dual-porosity structure in the raw soil which was attributed to the presence of a single mineral and the dispersed fabric caused by compaction at optimum conditions. The structure changed to a flocculated unimodal distribution after stabilization. A small decrease in porosity was observed with increasing curing time mainly due to the formation of cementitious products and the dominant pore size steadily shifted to smaller pore sizes from about 0.12 μm for the raw soil to 0.06 μm for the 90-day cured sample. The evolution of the pore size distribution was more telling and revealed that the large pores (0.1 – 10 μm) greatly diminished accompanied by a concomitant increase in the smaller pores (less than 0.1 μm) with increasing curing time. An excellent linear correlation was found between the evolution of the pore size distribution and the unconfined compressive strength.

5.2 Recommendations for Future Research

A deep understanding of the macroscopic behavior of stabilized soils based on changes made at the microscale level can be very challenging especially when dealing with natural soils and a complex stabilizer such as cement. While the objectives of this research study, in terms of advancing the microstructure characterization of cement stabilized soil, were successfully achieved, the accomplished work opened the door to many areas that could be explored. Several recommendations can be made with respect to future research plans that could help answer some of the questions raised in this study.

1. The outcomes from the thermogravimetric analysis look promising. However, these results should be extrapolated to other clay minerals, namely illite and montmorillonite, a variety of natural soils, as well as different stabilizers. Given the inherent complexity of natural soils, the occurrence of overlapping peaks from the decomposition of different components is possible. In this case, the results from the stabilized soil can be normalized or calibrated based on the raw material.
2. Similarly, quantitative XRD using both the whole-pattern fitting and the RIR method could be extended to other soils to compare the accuracy and robustness of each of these two methods.
3. A digital image analysis program such as Image-Pro Premier could be used to quantify several properties. Low magnification images could be used to approximate the porosity of each specimen and compare it to the theoretical porosity and that obtained from MIP testing. Fabric orientation of clays may also be quantified using low magnification images of the vertical plane as described in previous studies such as Martinez-Nistal (1999), but also track the change in particles orientation resulting from the addition of the stabilizer. The average particle size can be estimated from the micrographs of the horizontal plane at high magnifications. Since clay particles have been

shown to dissolve over time after the addition of stabilizer, the digital image analysis program could be used to monitor the change in the average particle size with curing time.

4. Surface analysis by X-ray Photoelectron Spectroscopy (XPS) has a high surface sensitivity with analysis depth of about 10 nm and thus is more suitable for surface analysis than EDS. XPS offers lower detectability limits and the quantitative elemental composition analysis is greatly improved compared to EDS which suffers from matrix effects. Thus, the identification of the formed crystals as a result of stabilization becomes easier and more accurate.

References

Ahmed, S., Lovell, C.W. Jr., and Diamond, S. (1974). "Pore Sizes and Strength of Compacted Clay." *Journal of Geotechnical Engineering Division,* ASCE, Vol. 100, No. GT4, pp. 407-425.

Alarcon-Ruiz, L., Platret, G., Massieu, E., and Ehrlacher, A. (2005). "The Use of Thermal Analysis in Assessing the Effect of Temperature on a Cement Paste." *Cement and Concrete Research*, 35, pp. 609-613.

Al-Rawas, A.A. (1999). "The Factors Controlling the Expansive Nature of the Soils and Rocks of Northern Oman." *Engineering Geology*, Vol. 53, pp. 327-350.

Al-Rawas, A.A. (2002). "Microfabric and Mineralogical Studies on the Stabilization of an Expansive Soil using Cement by-pass Dust and some Types of Slags." *Canadian Geotechnical Journal*, 39 (5), pp. 1150-1167.

Al-Rawas, A.A., and McGown, A. (1999). "Microstructure of Omani Expansive Soils." *Canadian Geotechnical Journal*, Vol. 36, pp. 272-290.

ASTM. (2011). 2011 Annual Book of ASTM Standards. Volume 04.08 Soil and Rock (I): D420-D5876 and Vol. 4.09 Soil and Rock (II): D5877 – latest. West Conshohocken, Pennsylvania.

Barden, L., and Sides, G.R. (1970). "Engineering Behavior and Structure of Compacted Clay." *Journal of the Soil Mechanics and Foundation Division*, Vol. 96, No. SM4, pp. 1171-1200.

Bensted, J. and Barnes, P. (2002). *Structure and Performance of Cements*, 2nd edition, Spon Press of the Taylor & Francis Group, New York, N.Y.

BS 1377 (1990). British Standard Methods of Testing for Soils for Civil Engineering Purposes. British Standards Institution, London.

Brewer, R. (1976). *Fabric and Mineral Analysis of Soils*, Robert E. Krieger Publishing, Huntinton, NY.

Brunauer, S., Emmett, P.H., and Teller, E. (1938). "Adsorption of Gases in Multimolecular Layers." *Journal of the American Chemical Society*, Vol. 60, pp. 309-319.

Cerato, A.B. and Lutenegger, A.J. (2002). "Determination of Surface Area of Fine-Grained Soils by Ethylene (EGME) Method." *Geotechnical Testing Journal*, Vol. 25, No. 3, pp. 315-321.

Cerato, A.B. and Miller, G.A. (2013). “Determination of Soil Stabilizer Content Using X-Ray Fluorescence.” *Geotechnical Testing Journal*, Vol. 36, No. 5, pp. 1-5.

Cetin, H. (2004). “Soil-Particle and Pore Orientations during Consolidation of Cohesive Soils.” *Engineering Geology*, Vol. 73, pp. 1-11.

Cetin, H., Söylemez, M. (2004). “Soil-Particle and Pore Orientations during Drained and Undrained Shear of a Cohesive Sandy Silt-Clay Soil.” *Canadian Geotechnical Journal*, Vol. 41, pp. 1127-1138.

Cetin, H., Fener, M., Söylemez, M., Gunaydin, O. (2007). “Soil Structure Changes during Compaction of a Cohesive Soil.” *Engineering Geology*, Vol. 92, pp. 38-48.

Cheng, H., Yang, J., Liu, Q., and He, J., and Frost, R.L. (2010). “Thermogravimetric Analysis-Mass Spectrometry (TG-MS) of Selected Chinese Kaolinites.” *Thermochimica Acta*, 507, pp. 106-114.

Choquette, M., Marc-André Bérubéa, and Locat, J. (1987). “Mineralogical and Microtextural Changes Associated with Lime Stabilization of Marine Clays from Eastern Canada.” *Applied Clay Science*, Vol. 2, No. 3, 215-232.

Chrysochoou, M. (2014). “Investigation of the Mineral Dissolution Rate and Strength Development in Stabilized Soils Using Quantitative X-Ray Diffraction.” *Journal of Materials in Civil Engineering*, Vol. 26, No.2, 288–295.

Circeo, L.J., Davidson, D.T., and David, H.T. (1962). “Strength-Maturity Relations of Soil-Cement Mixtures.” *Highway Research Board Bulletin*, Vol. 353, pp.84-97.

Collins, K., and McGown, A. (1983). “Micromorphological Studies in Soil Engineering.” *In: Soil Micromorphology 1. Techniques and Applications. Edited by P. Bullock and C.P. Murphy.* AB Academic Publishers, Bicester, U.K.

De La Torre, A.G., Bruque, S., and Aranda, M.A.G. (2001). “Rietveld Quantitative Amorphous Content Analysis.” *Journal of Applied Crystallography*, Vol. 34, pp. 196-202.

Delage, P., Audiguier, M., Cui, Y.J., and Howatt, M.D. (1996). “Microstructure of a Compacted Silt.” *Canadian Geotechnical Journal*, Vol. 33, pp. 150–158.

Delage, P., and Lefebvre, G. (1984). “Study of Structure of a Sensitive Champlain Clay and of its Evolution during Consolidation.” *Canadian Geotechnical Journal*, Vol. 21, pp. 21–35.

Delage, P., and Pellerin, F.M. (1984). “Influence de la Lyophilisation sur la structure d’une argile sensible du Québec.” *Clay Minerals*, Vol. 19, pp. 151-160.

Delage, P., Tessier, D., and Marcel-Audiguier, M. (1982). "Use of the Cryoscan Apparatus for Observation of Freeze-Fractured Planes of a Sensitive Quebec Clay in Scanning Electron Microscopy." Canadian Geotechnical Journal, Vol. 19, No. 1, pp. 111–114.

Diamond, S., and Kinter, E.B. (1965). "Mechanisms of Soil-Lime Stabilization." *Highway Research Record.,* 92, 83-102.

El-Jazairi, B., and Illston, J.M. (1977). "A Simultaneous Semi-Isothermal Method of Thermogravimetry and Derivative Thermogravimetry, and its Application to Cement Pastes." Cement and Concrete Research, Vol. 7, pp. 247–258.

El-Jazairi, B., and Illston, J.M. (1980). "The Hydration of Cement Paste Using The Semi-Isothermal Method of Derivative Thermogravimetry." Cement and Concrete Research, Vol. 10, pp. 361–366.

England, B.M. (1991). "The State of the Science: Scanning Electron Microscopy." *The Mineralogical Record*, Vol. 22, 123–132.

Ferber, V., Auriol, J.C., Cui, Y.J., Magnan, J.P. (2009). "On the Swelling Potential of Compacted High Plasticity Clays." *Engineering Geology*, Vol. 104, pp. 200-210.

Frost, J.D., and McNeil, S. (1998). "Imaging Technologies; Techniques and Applications in Civil Engineering." *Proceedings of the 2nd International Conference,* ASCE, Reston, VA.

Frost, J.D., and Wright, J.R. (1993). "Digital Image Processing: Techniques and Applications in Civil Engineering." *Proceedings of a Conference,* Kona, Hawaii, Feb 28-Mar 5, 1993, ASCE, 312p.

Garcia-Bengochea, I., Lovell, C.W., and Altschaefli, A.G. (1979). "Pore distribution and permeability of silty clays." *Journal of the Geotechnical Engineering Division*, ASCE, 105(GT7), 839- 856.

Gillot, J.E. (1969). "Study of the Fabric of Fine-Grained Sediments with the Scanning Electron Microscope." *Journal of Sedimentary Petrology*, Vol. 39, pp. 90–105.

Glenn, G.R. (1967). "X-Ray Studies of Lime-Bentonite Reaction Products." *Journal of the American Ceramic Society,* Vol. 50, 312-316.

Goldstein, J.I., Newburry, D.E., Echlin, P., Joy, D.C., Romig, A.D., Lyman, C.E., Fiori, C., and Lifshin, E. (1992). Scanning Electron Microscopy and X-Ray Microanalysis. Plenum Press, New York.

Griffiths, F.J., and Joshi, R.C. (1989). “Change in pore size distribution due to consolidation of clays.” *Géotechnique*, 39, 159–167.

Heide, K., and Földvari, M. (2006). “High Temperature Mass Spectrometric Gas-Release Studies of Kaolinite $Al_2[Si_2O_5(OH)_4]$ Decomposition.” *Thermochimica Acta*, 446, 106-112.

Hillier, S. (2000). “Accurate Quantitative Analysis of Clay and Other Minerals in Sandstone by XRD: Comparison of a Rietveld and a Reference Intensity Ratio (RIR) Method and the Importance of Sample Preparation.” *Clay Minerals*, Vol. 35, pp. 291-302.

Hinckley, D.N. (1963). “Variability in ‘Crystallinity’ Values among the Kaolin Deposits of the Coastal Plain of Georgia and South Carolina.” *Clays Clay Miner.*, Vol. 11, pp.229-235.

Hindar, J., Holm, J.L., Lindemann, J., and Lønvik, J. (1980). “Investigation of Some Kaolines by Simultaneous DTA/TG and Thermosonimetry.” Thermal Analysis ICTA 80, vol. II, Birkhäuser Verlag, Basel, pp. 313-318.

Horpibulsuk, S. (2012). “Strength and Microstructure of Cement Stabilized Clay.” Scanning Electron Microscopy, Dr. Viacheslav (Ed.), ISBN: 978-953-51-0092-8, InTech, Available from: http://www.intechopen.com/books/scanning-electron-microscopy/strength-and-microstructure-of-cement-stabilized-clay.

Horpibulsuk, S., Katkan, W., and Naramitkornburee, A. (2009). “Modified Ohio’s Curves: A Rapid Estimation of Compaction Curves for Coarse- and Fine-Grained Soils.” *Geotechnical Testing Journal*, ASTM, Vol. 32, No.1, pp. 115-125.

Horpibulsuk, S., Rachan, R., Chinkulkijniwat, A., Raksachon, Y., and Suddeepong, A. (2010). “Analysis of Strength Development in Cement-Stabilized Silty Clay based on Microstructural Considerations.” *Construction and Building Materials*, Vol. 24, pp.2011-2021.

Kamruzzaman, A.H.M., Chew, S.H., and Lee, F.H. (2009). “Structuration and Destructuration Behavior of Cement-Treated Singapore Marine Clay.” *Journal of Geotechnical and Geoenvironmental Engineering*, Vol. 135, No. 4, pp. 573–589.

Kang, M.S., Watabe, Y., and Tsuchida, T. (2003). “Effect of Drying Process on the Evaluation of Microstructure of Clays using Scanning Electron Microscope (SEM) and Mercury Intrusion Porosimetry (MIP).” *Proceedings of the Thirteenth International Offshore and Polar Engineering Conference*, Honolulu, Hawaii, USA , May 25-30, 2003. pp. 385-392.

Katti, D.R., and Shanmugasundaram, V. (2001). “Influence of Swelling on the Microstructure of Expansive Clays.” *Canadian Geotechnical Journal*, Vol. 38, pp. 175-182.

Khoury, N., and Khoury, C. (2005). “New Laboratory Methods for Characterization of Compaction in Fine-Grained Soils.” Internal Report (Revised in 2008). School of Civil Engineering and Environmental Science, University of Oklahoma, Norman, OK.

Khoury, N., Musharraf, Z., and Laguros, J. (2006). “Semi-Quantification of Cementing Products Using X-Ray Diffraction Technique in Stabilized Aggregate.” Journal of X-Ray Science and Technology, 14(1), 39-54.

Koliji, A., Vulliet, L., and Laloui, L. (2010). “Structural Characterization of Unsaturated Aggregated Soil.” *Canadian Geotechnical Journal*, Vol. 47, No. 3, pp. 297-311.

Kruger, R. (1990). “The Chemistry of Fly Ash and the Pozzolanic Reaction.” *Chemsa*, 16(11), 301-303.

Last,W.M. (2001). “Mineralogical Analysis of Lake Sediments.” In: Last,W.M., Smol, J.P. (eds.), *Tracking Environmental Change Using Lake Sediments*, Vol. 2: Physical and Geochemical Methods. Kluwer Academic Publishers, Dordrecht, The Netherlands.

Lea, F. M., and P. C. Hewlett (2004). *Lea's chemistry of cement and concrete*, 4th edition, New York: Elsevier Butterworth-Heinmann.

Li, X., Zhang, M. (2009). “Characterization of Dual-Structure Pore-Size Distribution of Soil.” *Canadian Geotechnical Journal*, Vol. 46, No.2, pp. 129-141.

Lin, B. (2012). “A Comprehensive Investigation on Microscale Properties and Macroscopic Behavior of Natural Expansive Soils.” Ph.D. Dissertation, University of Oklahoma, Norman, Oklahoma, USA.

Lin, B. and Cerato, A.B. (2014). “Applications of SEM and ESEM in microstructural investigation of shale-weathered expansive soils along swelling-shrinkage cycles.” *Engineering Geology*, 177, 66-74.

Lin, D.F., Lin, K.F., Hung, M.J., and Luo, H.L. (2007). “Sludge Ash/Hydrated Lime on the Geotechnical Properties of Soft Soil.” *J. Hazard. Mater.*, Vol. 145, pp.58-64.

Liu, Z.B., Shi, B., Inyang, H.I., and Cai, Y. (2005). “Magnification Effects on the Interpretation of SEM Images of Expansive Soils.” *Engineering Geology*, Vol. 78, pp. 89-94.

Martinez-Nistal, A., Veniale, F., Setti, M., and Cotecchia, F. (1999). "A Scanning Electron Microscopy Image Processing Method for Quantifying Fabric Orientation of Clay Geomaterials." *Applied Clay Science*, Vol. 14, pp. 235-243.

Midgley, H.G. (1979). "The Determination of Calcium Hydroxide in Set Portland Cements." *Cement and Concrete Research*, Vol. 9, pp. 77–82.

Mitchell, J.K., and Soga, K. (2005). Fundamentals of Soil Behavior, 3rd edn. John Wiley, Sons, Inc, New Jersey.

Mojumdar, S. (2001). "Processing-Moisture Resistance and Thermal Analysis of Macro-Defect-Free Materials." *Journal of Thermal Analysis and Calorimetry*, Vol. 64, pp. 1133-1139.

Montes-H, G., Duplay, J., Martinez, L., and Mendoza, C. (2003a). "Swelling-Shrinkage Kinetics of MX80 Bentonite." *Appl Clay Sci*, Vol. 22, pp. 279–293.

Montes-H, G., Duplay, J., Martinez, L., Geraud, Y., and Rousset-Tournier, B. (2003b). "Influence of Interlayer Cations on the Water Sorption and Swelling-Shrinkage of MX80 Bentonite." *Appl Clay Sci*, Vol. 23, pp. 309–321.

Moore, D.M., and Reynolds, R.C. Jr. (1997). X-Ray Diffraction and the Identification and Analysis of Clay Minerals, 2nd Edition. Oxford University Press, New York.

Penumadu, D., and Dean, J. (2000). "Compressibility Effect in Evaluating the Pore-Size Distribution of Kaolin Clay Using Mercury Intrusion Porosimetry." *Canadian Geotechnical Journal*, Vol. 37, No. 2, pp. 393-405.

Peterson, L.W., Moldrup, P., Jacobsen, O.H. and Rolston, D.E. (1996). "Relations between specific surface area and soil physical and chemical properties." *Soil Science*, 161(1), 9-21.

Plançon, A., Giese, R.F., and Snyder, R. (1988). "The Hinckley Index of Kaolinites." *Clay Minerals*, Vol. 23, pp. 249-260.

Rietveld, H.M. (1969). "A Profile Refinement Moethod for Nuclear and Magnetic Structures." *Journal of Applied Crystallography*, Vol. 2, pp. 65-71.

Romero, E., Gens, A., and Lloret, A. (1999). "Water permeability, Water Retention and Structure of Unsaturated Compacted Boom Clay." *Engineering Geology*, Vol. 54, pp. 117-127.

Romero, E., and Simms, P.H. (2008). "Microstructural Investigation in Unsaturated Soils: A Review with Special Attention to Contribution of Mercury Intrusion Porosimetry and Environmental Scanning Electron Microscopy." *Geotechnical and Geological Engineering*, Vol. 26, pp. 705-727.

Shi, B., and Li, S., and Tolkachev, M. (1995). “Quantitative Approach on SEM Images of Microstructure of Clay Soils.” *Scienta Sinica, Series B:Chemistry,* Life Sciences, and Earth Sciences, Vol. 38, No. 6, pp. 741-748.

Shi, S., Murakami, Y., and Wu, Z.S. (1998). “Orientation of Aggregates of Fine-Grained Soil: Quantification and Application.” *Engineering Geology*, Vol. 50, No. 1-2, pp. 59-70.

Simms, P.H., and Yanful, E.K. (2002). “Predicting Soil-Water Characteristic Curves of Compacted Plastic Soils from Measured Pore-Size Distributions.” *Géotechnique*, Vol. 52, No. 4, pp. 269-278.

Smart, P. (1967). “Particle Arrangements in Kaolin.” *Proceedings of the 15th National Conference on Clays and Clay Minerals*, Vol. 15, pp. 241-254.

Smart, P., and Leng, X. (1993). “Present Developments in Image Analysis.” *Scanning Microscopy*, Vol. 7, No. 1, pp. 5-16.

Snyder, R.L., and Bish, D.L. (1989). “Quantitative Analysis.” In: Bish, D.L., and Post, J.E. (editors), *Modern Powder Diffraction*. Reviews in Mineralogy, 20, pp. 101-144. Mineralogical Society of America, Washington, USA.

Soroka, I. (1980). “Portland Cement Paste and Concrete.” Chemical Publishing Co., Inc. New York, N.Y.

Stucki, J.W., and Bish, D.L. (1990). “Thermal analysis in clay science.” *CMS Workshop Lectures* Vol. 3, The Clay Minerals Society, Boulder, CO.

Tabet, W.E. and Cerato, A.B. (2015). “Structural Effects on the Effective Conductivity of Compacted Clays.” *IFCEE 2015*: pp. 2697-2706. San Antonio, TX, March 17-21, 2015.

Taylor H.F.W. (1990). “Cement Chemistry.” NY: Academic Press.

Tovey, N.K., and Hounslow, M.W. (1995). “Quantitative Microporosity and Orientation Analysis in Soils and Sediments.” *Journal of the Geological Society London*, Vol. 152, pp. 119-129.

Wang, J., Mo, H., Chen, J., and Gu, R. (2012). “Computer Processing Technical Analysis on Consolidation Microscopic Image of Soft Soil.” *Journal of Information & Computational Science*, 9(9), pp. 2465-2473.

Wang, K.S., Lin, K.L., Lee, T.Y., and Tzeng, B.Y. (2004b). “The Hydration Characteristics when C_2S is Present in MSWI Fly Ash Slag.” *Cement and Concrete Research*, Vol. 26, pp. 323–330.

Wang, L., Roy, A., Tittsworth, R., and Seals, R.K. (2004a). "Mineralogy of Soil Susceptible to Sulfate Attack after Stabilization." *Journal of Materials in Civil Engineering*, 16(4), pp. 375-382.

Washburn, E.W. (1921). "Note on a Method of Determining the Distribution of Pore Sizes in a Porous Material." *Proceedings of the National Academy of Sciences*, USA, Vol. 7, No. 4, pp. 115-116.

Zhou, Q., and Glasser, F.P. (2001). "Thermal Stability and Decomposition Mechanisms of Ettringite at <120^{o}C." *Cement and Concrete Research*, 31 (9), pp. 1333-1339.

Appendix A: Manufacturer Data Sheet for Kaolinite SA-1

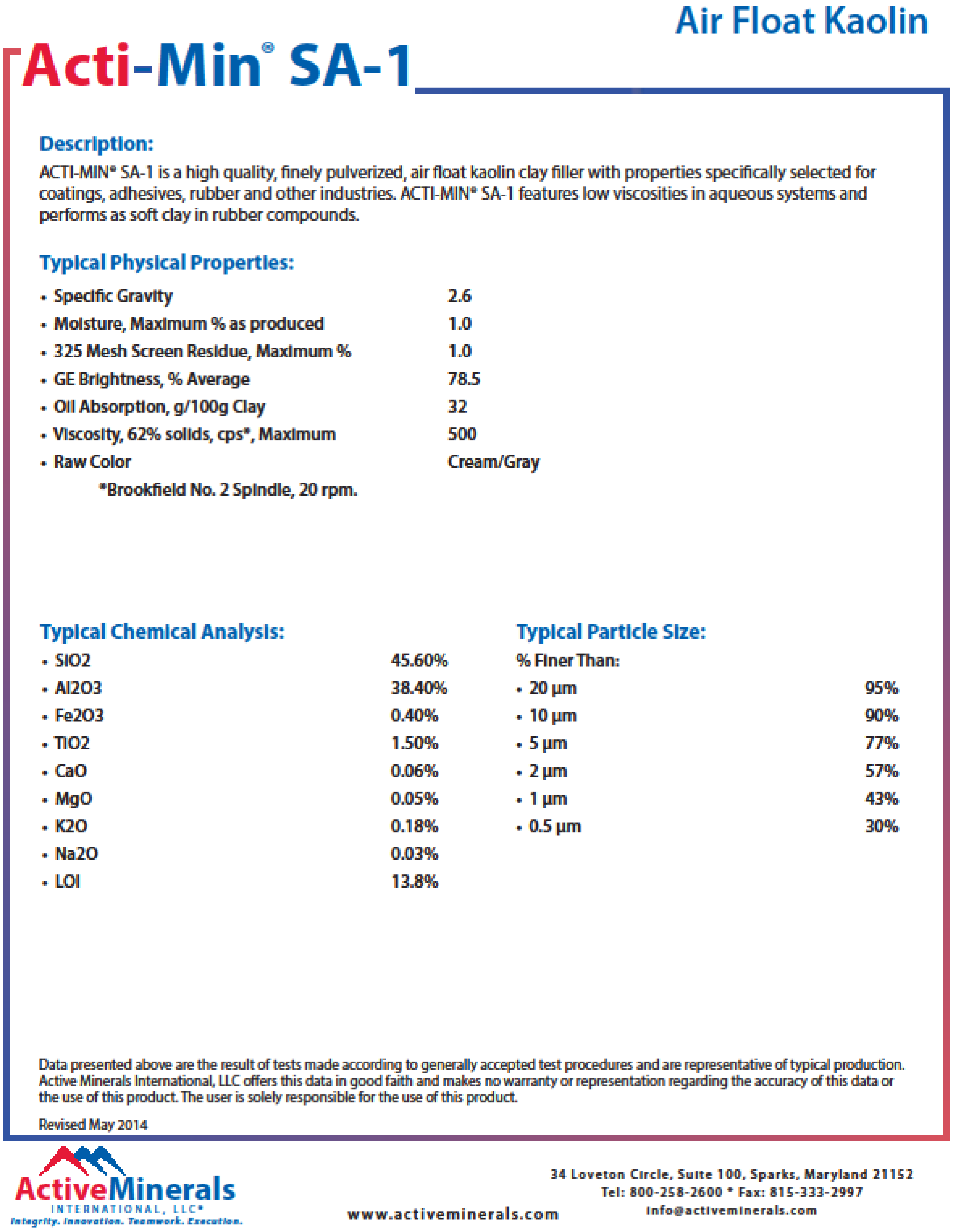

Air Float Kaolin

Acti-Min® SA-1

Description:

ACTI-MIN® SA-1 is a high quality, finely pulverized, air float kaolin clay filler with properties specifically selected for coatings, adhesives, rubber and other industries. ACTI-MIN® SA-1 features low viscosities in aqueous systems and performs as soft clay in rubber compounds.

Typical Physical Properties:

• Specific Gravity	2.6
• Moisture, Maximum % as produced	1.0
• 325 Mesh Screen Residue, Maximum %	1.0
• GE Brightness, % Average	78.5
• Oil Absorption, g/100g Clay	32
• Viscosity, 62% solids, cps*, Maximum	500
• Raw Color	Cream/Gray

*Brookfield No. 2 Spindle, 20 rpm.

Typical Chemical Analysis:

• SiO_2	45.60%
• Al_2O_3	38.40%
• Fe_2O_3	0.40%
• TiO_2	1.50%
• CaO	0.06%
• MgO	0.05%
• K_2O	0.18%
• Na_2O	0.03%
• LOI	13.8%

Typical Particle Size:

% Finer Than:

• 20 µm	95%
• 10 µm	90%
• 5 µm	77%
• 2 µm	57%
• 1 µm	43%
• 0.5 µm	30%

Data presented above are the result of tests made according to generally accepted test procedures and are representative of typical production. Active Minerals International, LLC offers this data in good faith and makes no warranty or representation regarding the accuracy of this data or the use of this product. The user is solely responsible for the use of this product.

Revised May 2014

ActiveMinerals
INTERNATIONAL, LLC®
Integrity. Innovation. Teamwork. Execution.

www.activeminerals.com

34 Loveton Circle, Suite 100, Sparks, Maryland 21152
Tel: 800-258-2600 * Fax: 815-333-2997
info@activeminerals.com

Appendix B: Manufacturer Data Sheet for Portland Cement

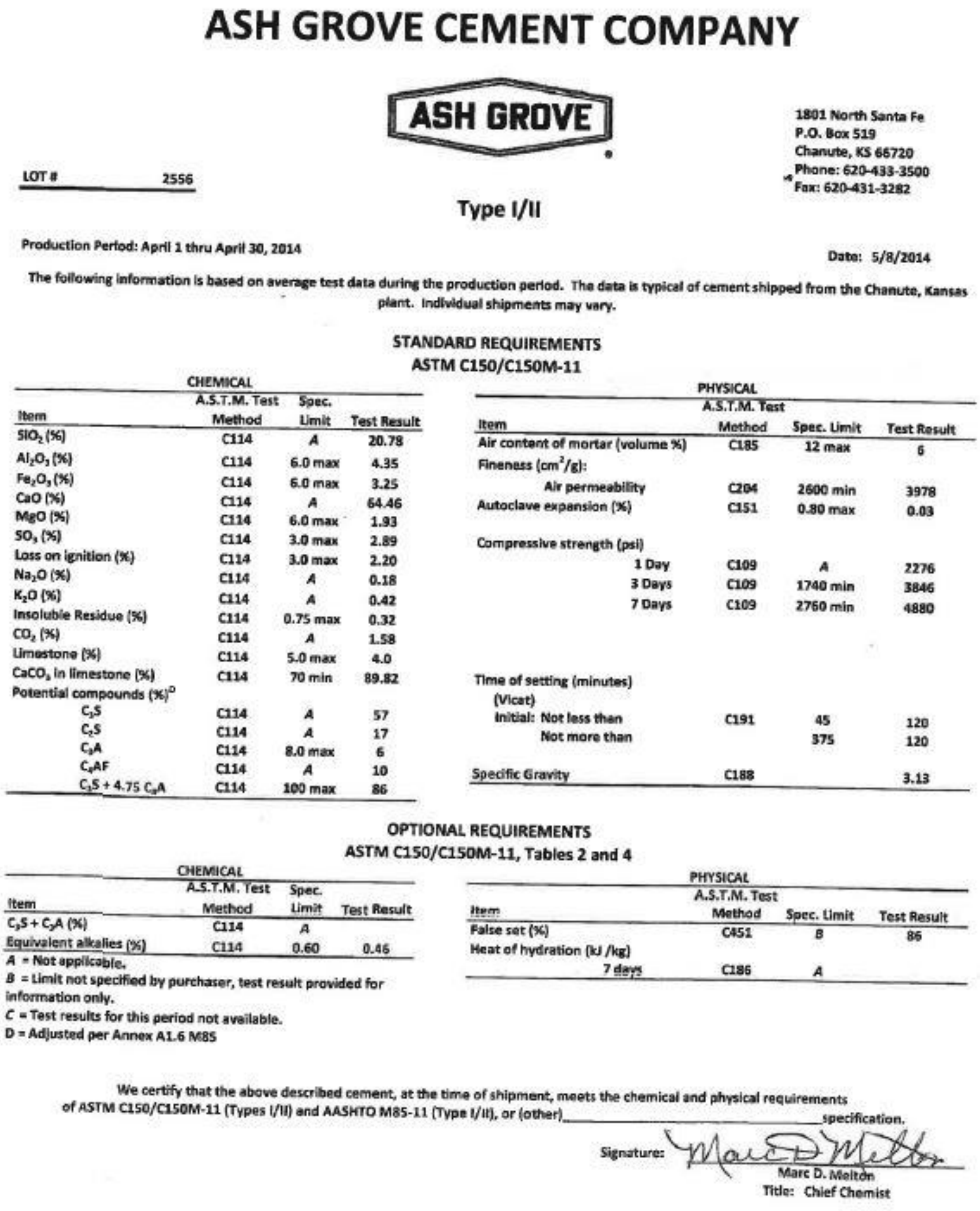

ASH GROVE CEMENT COMPANY

ASH GROVE

1801 North Santa Fe
P.O. Box 519
Chanute, KS 66720
Phone: 620-433-3500
Fax: 620-431-3282

LOT # 2556

Type I/II

Production Period: April 1 thru April 30, 2014

Date: 5/8/2014

The following information is based on average test data during the production period. The data is typical of cement shipped from the Chanute, Kansas plant. Individual shipments may vary.

STANDARD REQUIREMENTS
ASTM C150/C150M-11

CHEMICAL

Item	A.S.T.M. Test Method	Spec. Limit	Test Result
SiO_2 (%)	C114	*A*	20.78
Al_2O_3 (%)	C114	6.0 max	4.35
Fe_2O_3 (%)	C114	6.0 max	3.25
CaO (%)	C114	*A*	64.46
MgO (%)	C114	6.0 max	1.93
SO_3 (%)	C114	3.0 max	2.89
Loss on ignition (%)	C114	3.0 max	2.20
Na_2O (%)	C114	*A*	0.18
K_2O (%)	C114	*A*	0.42
Insoluble Residue (%)	C114	0.75 max	0.32
CO_2 (%)	C114	*A*	1.58
Limestone (%)	C114	5.0 max	4.0
$CaCO_3$ in limestone (%)	C114	70 min	89.82
Potential compounds (%)^D			
C_3S	C114	*A*	57
C_2S	C114	*A*	17
C_3A	C114	8.0 max	6
C_4AF	C114	*A*	10
$C_3S + 4.75\ C_3A$	C114	100 max	86

PHYSICAL

Item	A.S.T.M. Test Method	Spec. Limit	Test Result
Air content of mortar (volume %)	C185	12 max	6
Fineness (cm^2/g):			
Air permeability	C204	2600 min	3978
Autoclave expansion (%)	C151	0.80 max	0.03
Compressive strength (psi)			
1 Day	C109	*A*	2276
3 Days	C109	1740 min	3846
7 Days	C109	2760 min	4880
Time of setting (minutes) (Vicat)			
Initial: Not less than	C191	45	120
Not more than		375	120
Specific Gravity	C188		3.13

OPTIONAL REQUIREMENTS
ASTM C150/C150M-11, Tables 2 and 4

CHEMICAL

Item	A.S.T.M. Test Method	Spec. Limit	Test Result
$C_3S + C_3A$ (%)	C114	*A*	
Equivalent alkalies (%)	C114	0.60	0.46

A = Not applicable.
B = Limit not specified by purchaser, test result provided for information only.
C = Test results for this period not available.
D = Adjusted per Annex A1.6 M85

PHYSICAL

Item	A.S.T.M. Test Method	Spec. Limit	Test Result
False set (%)	C451	*B*	86
Heat of hydration (kJ /kg)			
7 days	C186	*A*	

We certify that the above described cement, at the time of shipment, meets the chemical and physical requirements of ASTM C150/C150M-11 (Types I/II) and AASHTO M85-11 (Type I/II), or (other)____________________ specification.

Signature: Marc D Melton
Marc D. Melton
Title: Chief Chemist

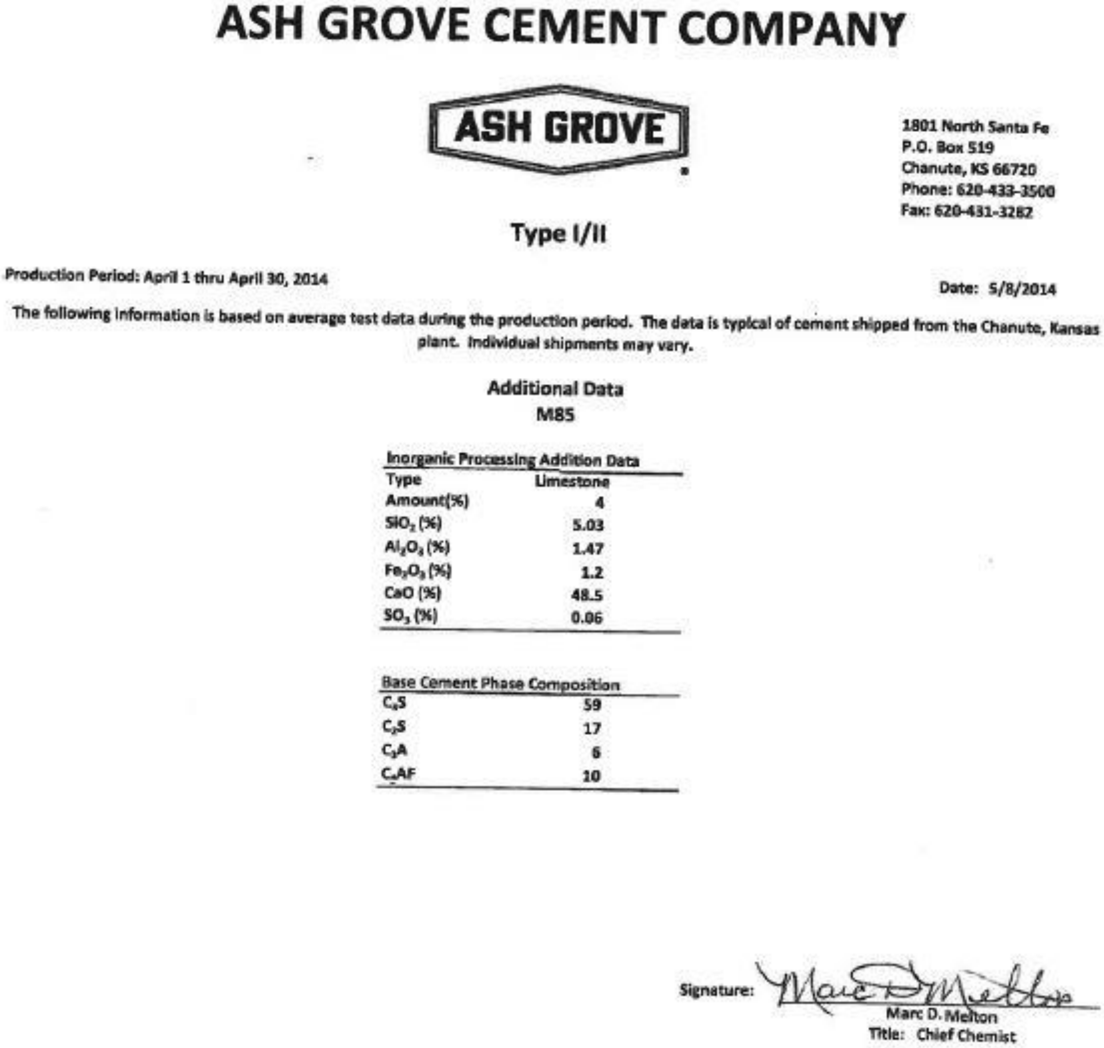

ASH GROVE CEMENT COMPANY

ASH GROVE

1801 North Santa Fe
P.O. Box 519
Chanute, KS 66720
Phone: 620-433-3500
Fax: 620-431-3282

Type I/II

Production Period: April 1 thru April 30, 2014

Date: 5/8/2014

The following information is based on average test data during the production period. The data is typical of cement shipped from the Chanute, Kansas plant. Individual shipments may vary.

Additional Data
M85

Inorganic Processing Addition Data

Type	Limestone
Amount(%)	4
SiO_2 (%)	5.03
Al_2O_3 (%)	1.47
Fe_2O_3 (%)	1.2
CaO (%)	48.5
SO_3 (%)	0.06

Base Cement Phase Composition

C_3S	59
C_2S	17
C_3A	6
C_4AF	10

Signature: Marc D Melton
Marc D. Melton
Title: Chief Chemist

Appendix C: Repeatability of Thermogravimetric Analysis Test

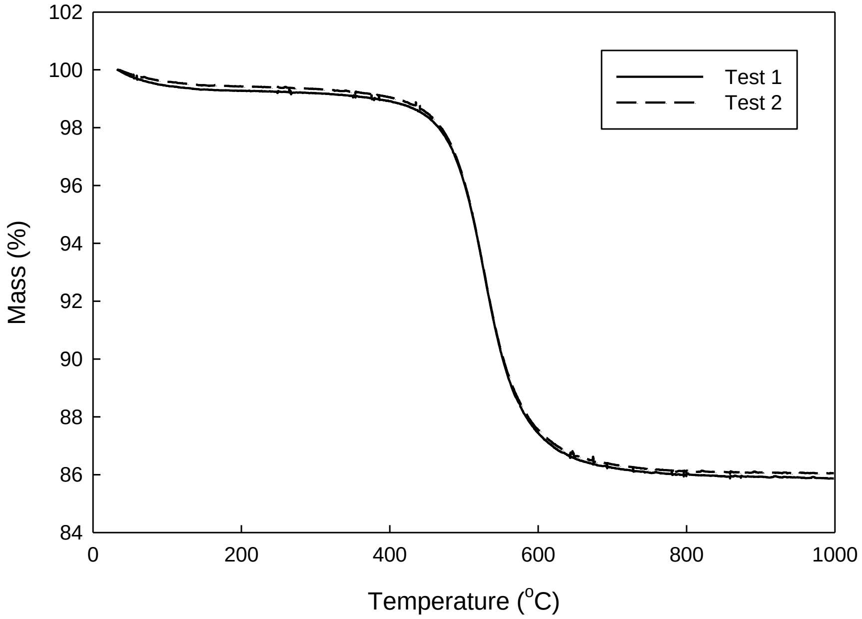

Figure C.1: TG Repeatability Tests for Raw Kaolinite

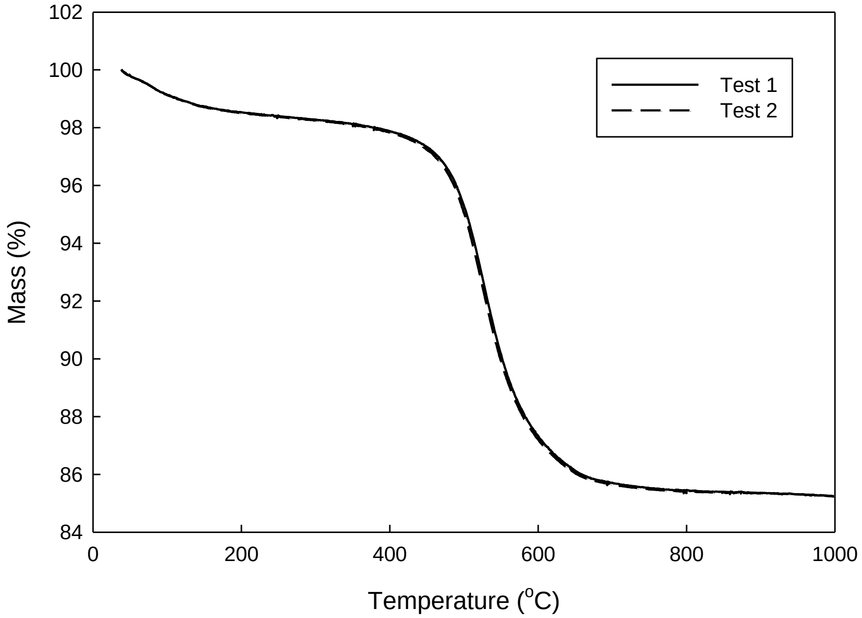

Figure C.2: TG Repeatability Tests for 1-day Cured Samples

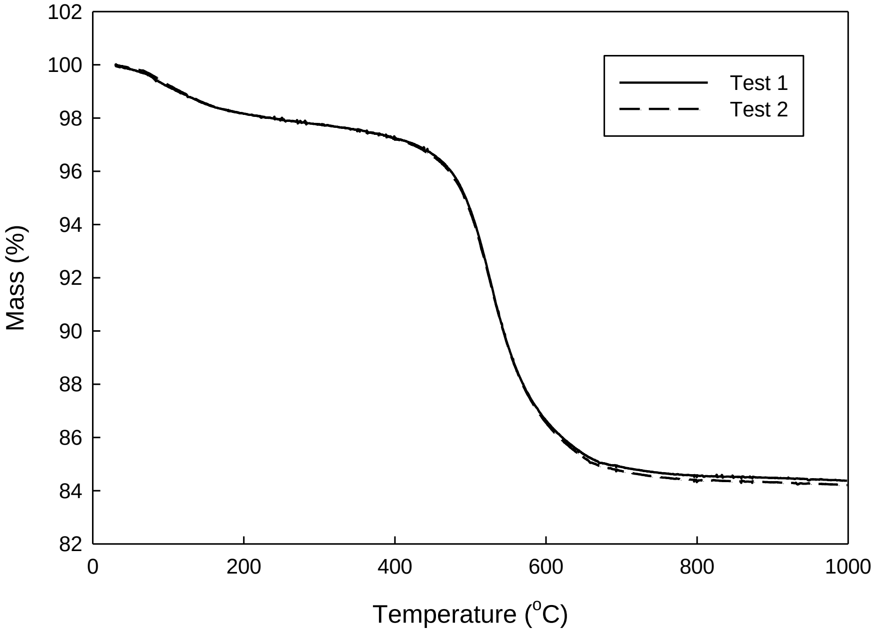

Figure C.3: TG Repeatability Tests for 7-day Cured Samples

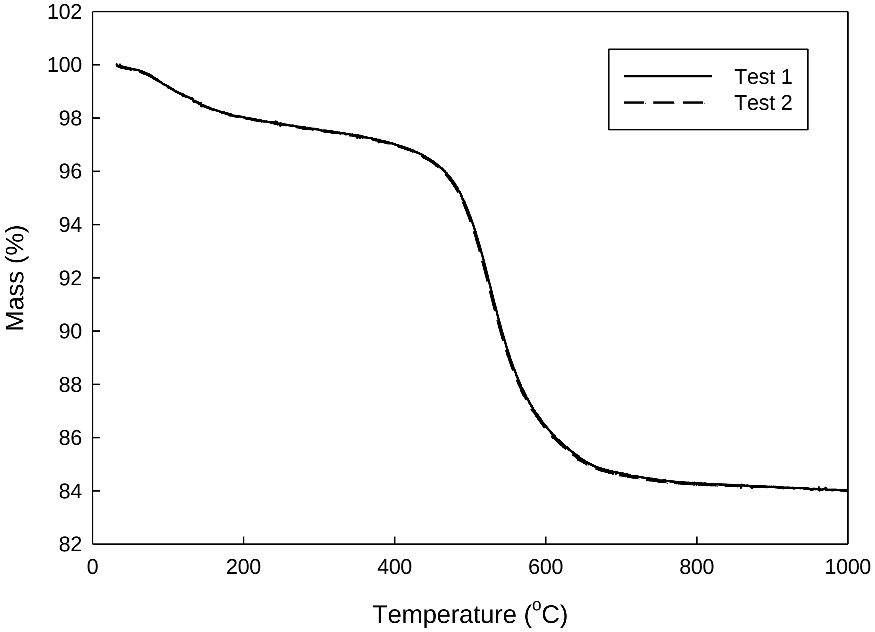

Figure C.4: TG Repeatability Tests for 14-day Cured Samples

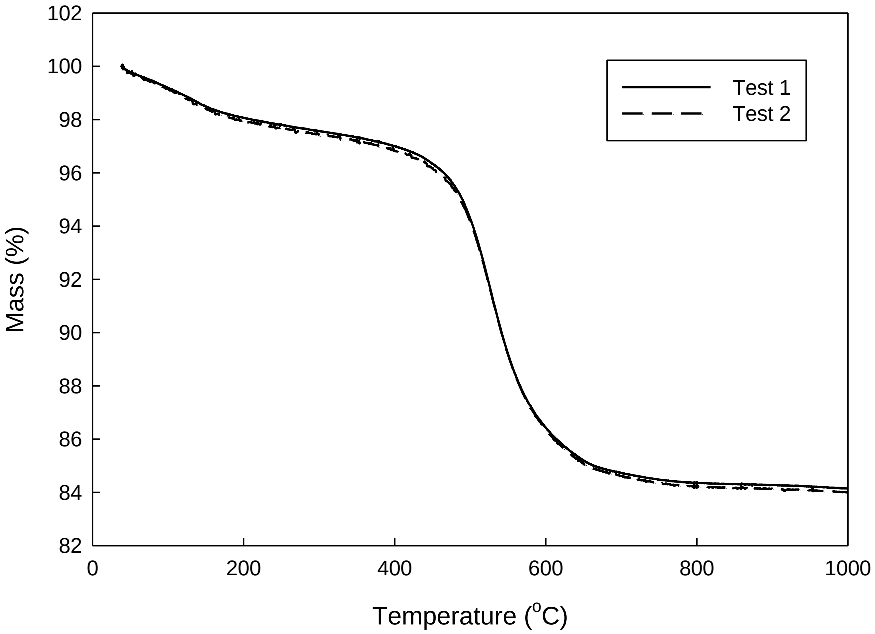

Figure C.5: TG Repeatability Tests for 14-day Cured Samples

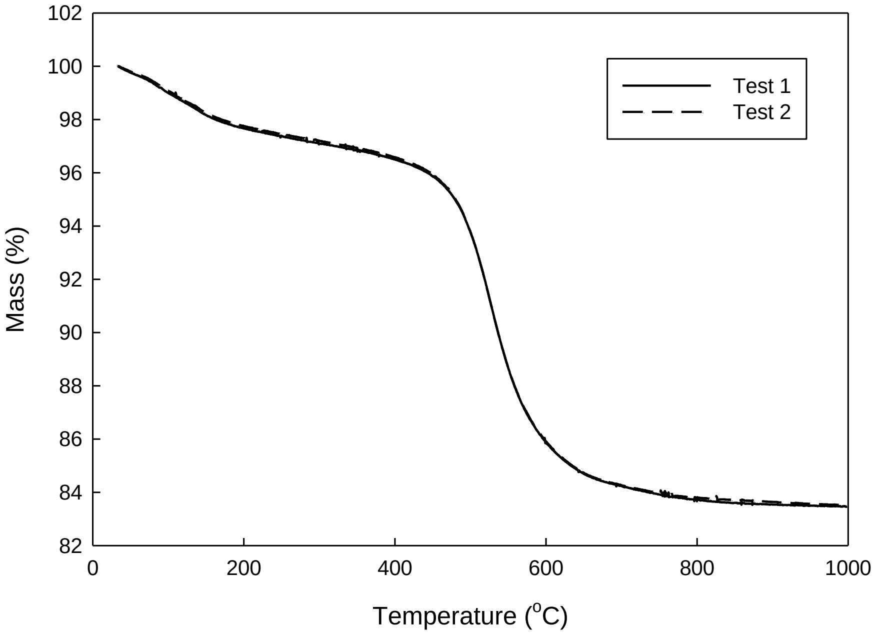

Figure C.6: TG Repeatability Tests for 14-day Cured Samples